Fast Neutron Measurements using Deuterated Liquid Scintillators

by

Mitaire I. Ojaruega

A dissertation submitted in partial fulfillment
of the requirements for the degree of
Doctor of Philosophy
(Applied Physics)
in The University of Michigan
2009

Doctoral Committee:

Professor Frederick D. Becchetti Jr., Chair
Professor Jean P. Krisch
Professor Homer A. Neal
Adjunct Professor James Kolata
Research Fellow Hanan Amro

To my family with lots of love.

ACKNOWLEDGEMENTS

Much love to my parents **Robert Ojaruega**, **Linda Sakpoba**, **Lucky Ajueyitsi** and **Betty Ajueyitsi**, for their unconditional love and support through thick and a lot of thin. I love you!

Thanks to my advisor **Professor Frederick D. Becchetti Jr**. for always being supportive. Thanks for a lot of advice and constantly reminding me to think critically. Thanks for not giving up on me. Thanks for handing me a beacon of hope in my darkest hour. My sincere gratitude for your patience, generosity, and superb mentoring. Be it known! When I grow up, I want to be like Prof. Becchetti.

Professor Brad Orr-Thanks for giving me a chance in the Applied Physics program. Thanks for your encouragements and your unwavering commitment to all the students in the AP-Program. Thank you.

Mi Negrita-(Anette Casiano-Negroni)-Te Quiero con todo mi corazon-Muchas gracias.

Professor Homer A. Neal-Thank you for serving on my thesis committee and for all the advice and encouragement over the years. My sincere gratitude.

Professor Jean Krisch- Thank you for everything you did to make my graduate school experience a much better one. Thanks for your timely and prudent advice during tough times and helping me to understand many circumstances better. Thanks for the countless hours spent in reading my many drafts, fellowship essays, and research papers. Thank you.

Professor James Kolata- Thanks for the guidance, especially during the experiment(s) at UND and for always willing to answer my many questions. Thanks for serving on my thesis committee.

Dr. Hanan Amro-Thanks for everything you've done for me. I am especially grateful for your patience during my learning-curve period and for serving on my committee. Thanks.

Jiang Hao-My partner in crime, thanks a lot buddy, for all your help with the DAQ, figures etc. I really do appreciate it and thanks for your friendship. Ganbei!

Sr. Ramon Torres-Isea-Gracias Amigo! Especially during the early days and for your patience with Sr. Ojaruega. Thanks.

R. Raymond Thanks Rich! For putting up with me and letting me drive you crazy all the time.

Amy Roberts and Anthony Villano-Thanks for all the work you both put into the experiments. I really appreciate it and can't say thank you enough..thanks.

Professor Hartman-I am very grateful for the countless hours you spent with me at NSL. Thanks for all the help with the neutron generators, simulations and advice over the past year. Thank you.

Professor Pozzi, Dr. Marek Flaska, Dr. Shaun Clarke-I can't thank you all enough for putting up with me and my many questions about Polimi. I really appreciate it. Thank you.

Professor Alec Gallimore-Thanks for your unconditional support throughout my graduate school experience. Thanks for helping to fund my endeavors over the years. I really appreciate it. Thank you.

Mr. Hugh Williams-Thanks for all the advice over the years. Thanks for helping with my writing and proof reading a lot of my materials. I am truly grateful.

TABLE OF CONTENTS

LIST OF TABLES

Table

LIST OF FIGURES

Figure

LIST OF APPENDICES

Appendix

CHAPTER I

Introduction

Nuclear physics is by no means a new phenomenom. It has been around for many decades and yet still begs to be fully understood. The atomic nucleus remains a remarkable quantum system, displaying a myriad of phenomena. Governed by the strong interaction between nucleons, nuclei exhibit correlations resulting in both single-particle and collective modes of excitations. Shortly after the discovery of the atomic nucleus, effort was dedicated to describing the nucleus based on the single-particle shell model, where the mean field produced by the ensemble of nucleons creates a potential in which individual nucleons reside in quantized states with single-particle wave functions [Krane, 1988]. Nuclear properties at energies close to the ground state were accounted for in this approach. However, in following years more complex properties of nuclei became the focus of research. Some of the new methods aim to understand how the motions of the individual nucleons couple, giving rise to collective vibrations or rotations of the nucleus as a whole. Another sign of nuclear collectivity is clustering, where subunits of nucleons tend to behave as separate units. In light nuclei, this occurs frequently and is important in nuclear astrophysics [BBFH, 1957][Rolf and Rodney, 1988].

As well known, the atomic nucleus is made up of protons and neutrons. The

proton number determines the particular element while the number of neutrons determine the isotope of that particular element. Neutrons and protons together are known as nucleons. There are approximately 6000 nuclides of which only about one third have been successfully produced and studied experimentally. Of all the artificially produced elements, roughly 300 of them are stable and essentially make up all the matter around us today. So where did these elements have their origin? Part of this question is presently being investigated in detail for the first time due to the development of short-lived radioactive nuclear beams (RNBs) [Kolata, 1989][Becchetti, 1990].

The majority of nuclear reaction studies have been on the stable isotopes as they are readily available. However, as noted, there are several thousand unstable isotopes whose nuclear properties have not been measured. Extrapolations of reaction rates for radioactive nuclei from rates observed with stable nuclei, has been shown to be unreliable [Becchetti, 1989]. There may be errors because of the very positive Q-values of reactions involving radioactive nuclei with low binding energy. Hence reaction rates involving radioactive nuclei calculated by nuclear models sometimes have uncertainties of a few orders of magnitude [Arnold, 1988].

The question of how the strong nuclear force holds together nuclei when $N >> Z$ or $Z >> N$ is crucial to understanding the very existence and composition of our universe. From the very beginning, e.g. a few minutes after the Big Bang, the interactions of nucleons to form light nuclei, and their accumulation in later processes in synthesizing heavier nuclei, has been important in defining our living environment (figs. 1.1 and 1.2). Our understanding of nuclear structure and synthesis of the elements is still largely empirical and based on the information available to us about the properties of stable and near-stable nuclei [BBFH, 1957].

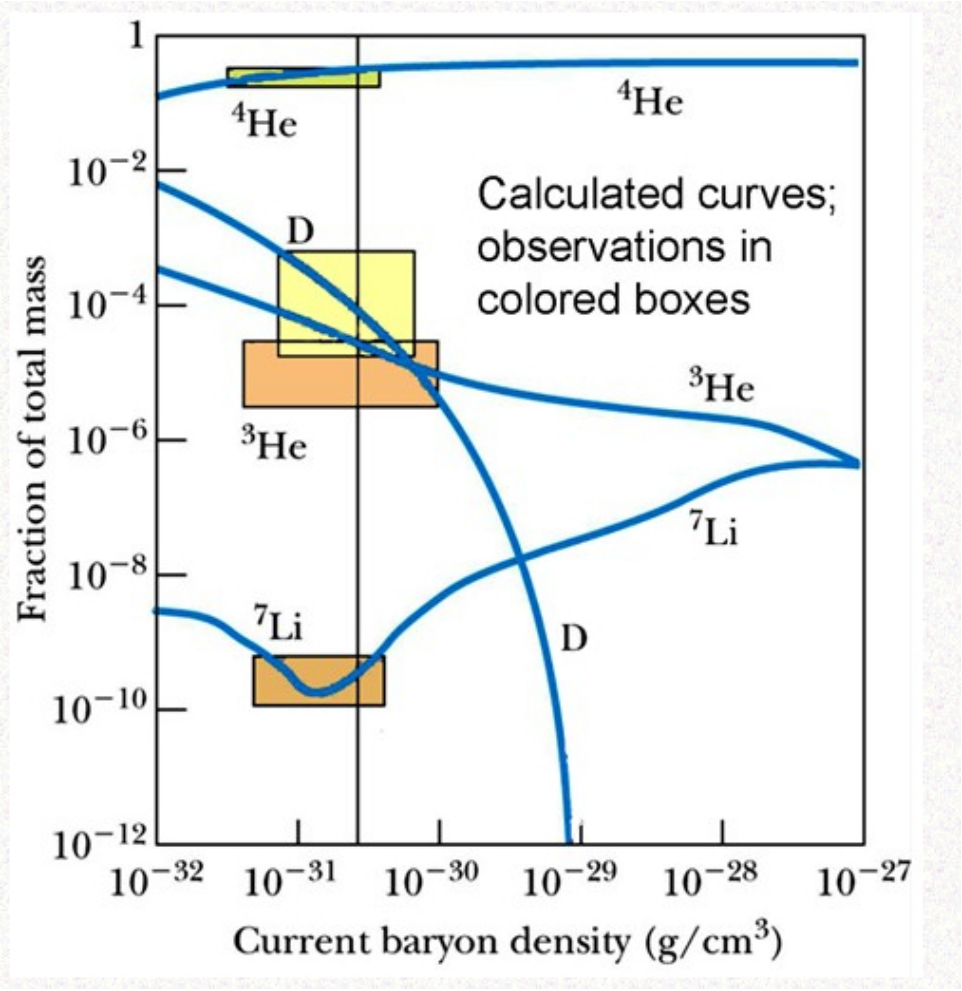

Figure 1.1: The predicted abundance of elements heavier than hydrogen, as a function of current baryon density in the universe compared with observations [Wittke, 2008].

1.1 Nuclear Astrophysics

Nuclear physics plays an enormous role in addressing key questions about the origin of matter in the universe. Life on earth is possible because of the structure of the atomic nuclei and the interactions between them. Knowing that the iron in our blood had their origin in nuclear reactions inside a star is a dramatic reminder of the link between our lives and the cosmic scale of nuclear astrophysics.

In many cases, the nuclear astrophysics of interest is in understanding rapid neutron-capture process (r-process). This process is a sequence of rapid neutron

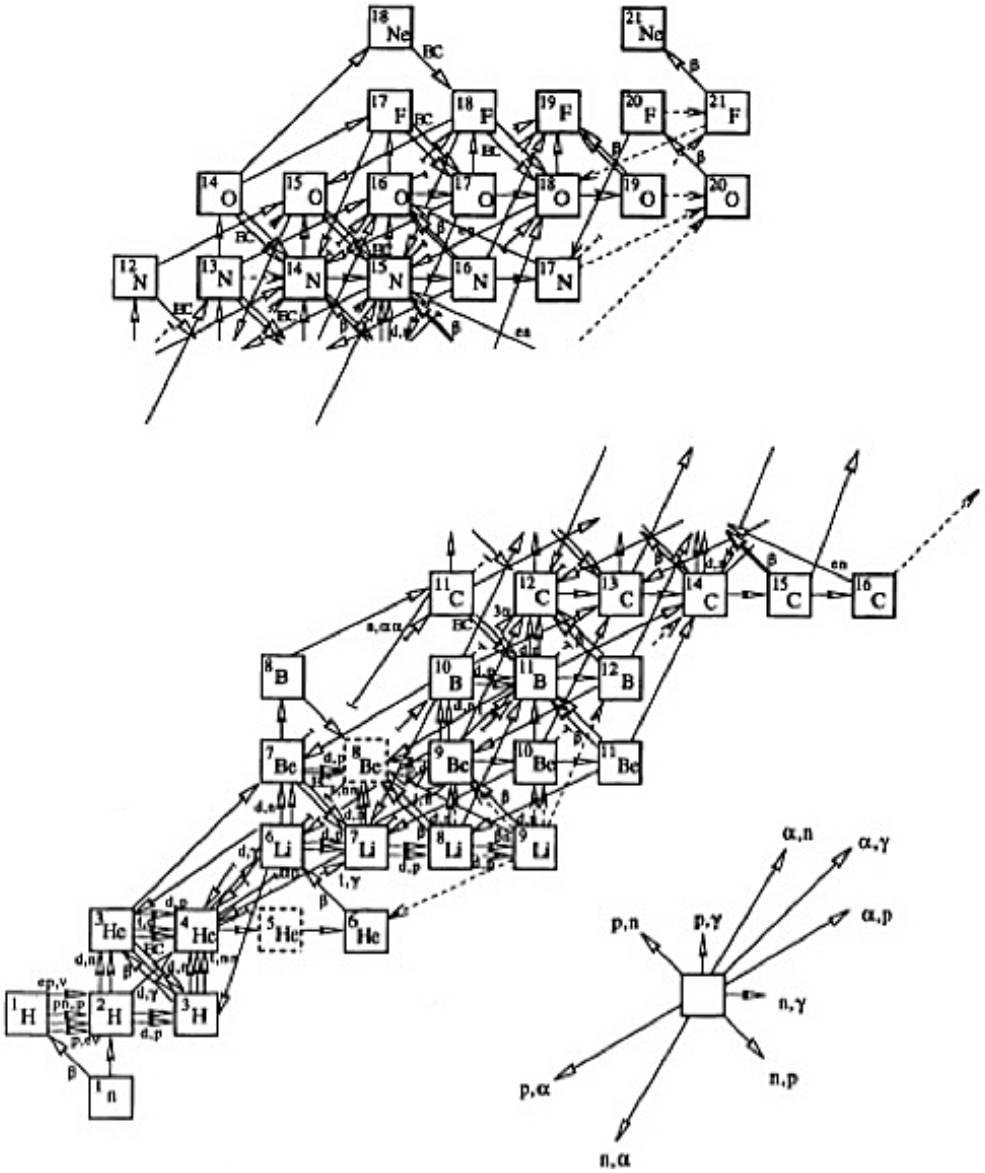

Figure 1.2: Nuclear astrophysics reaction chain [Olive, 2009].

captures on neutron-rich unstable nuclei interspersed with beta decays. This is believed to be responsible for the formation of elements beyond iron in the periodic table [BBFH, 1957]. While stars process hydrogen and helium fuel into medium-mass elements over millions of years, supernovae process some of this in just a few seconds and then disperse almost all into space to seed future generations of stars and planets. The knowledge of certain nuclear reaction cross sections (fig 1.2) is key to explaining cosmic processes like the Big Bang and stellar evolution [Schramm, 1996][Baur and Rebel, 1996]. Usually one needs to know these cross sections at very low collision energies corresponding to the relevant astrophysical temperatures (keVs). However, measuring at such energies with their small cross sections is often very difficult. But with new detectors and nuclear processes now available, answering some of the questions has been possible.

1.1.1 Big Bang Nucleosynthesis

Our knowledge about the origin of our universe is perhaps among the great achievements of the 20th century. This knowledge comes from many years of theory and experiments. Particle accelerators have been used to probe the energy range of the early universe.

Big Bang Nucleosynthesis (BBN) was proposed by Gamow, Alpher and Herman. [Gamow, Alpher, Herman, 1948] as a method to answer the questions about the creation of elements. However, because there were no stable nuclei with atomic weight 5 or 8, it made the aforementioned model unfit as a mechanism for producing elements much heavier than hydrogen and helium. Also, the initial conditions for the model by Gamow and colleagues assumed pure neutrons as the initial condition. Today it is believed that the light elements were created in two ways. Elements such

as hydrogen, helium and lithium were made in the first few minutes of the Big Bang, while most elements heavier than helium are believed to have been later produced in the cores of stars. Observations combined with theories allowed astronomers to make these conclusions.

The strength of BBN comes from the fact that most of the basic physics associated with it can be carried out in a laboratory. The relevant temperatures, 0.1 to about 1 MeV, are well explored in nuclear laboratory settings. Nuclear interactions under these condition are well understood and continue to be explored

The predictions of BBN have been used to test the big-bang model. The agreement between the observed and predicted abundance of light elements such as deuterium and lithium further helped to confirm the model and allowed the accurate determination of the present baryon density in the universe (fig. 1.1), between 1.7 x 10^{-31} and 4.1 x 10^{-31} grams per cubic centimeter [Copi, Schramm, and Turner, 1995][Wittke, 2008]. Although many questions have been answered with BBN, there still exist uncertainty in current values of the light element abundances and ratios (fig. 1.1). In particular, the deuterium, ^{3}He, ^{4}He and ^{7}Li abundances depend on the single parameter of the initial density of ordinary matter made out of protons and neutrons: baryonic matter [Olive, 2000]. As noted below, there is disagreement with the exact value or percentages and hence the amount of "normal" matter in the universe.

1.1.2 Missing Mass Problem

One of the major problems in astrophysics today is the missing mass problem, which as noted above concerns the amount of baryons in our universe. The ratio of the mass density, ρ, of the universe to the critical mass density, ρ_c, is determined by

the baryon mass density.

$$\rho_c = (3H_0^2/8\pi G) \backsimeq 5 * 10^{-30} g/cm \tag{1.1}$$

where H_0 = v/d = 50kms^{-1}Mpc^{-1} is Hubble's constant, and G is Newton's constant of gravity [Rolfs and Rodney, 1988]. It is agreed that the universe is open if ρ/ρc$\leq$ 1 and closed if $\rho/\rho_c \geq$1.

The standard big bang model [Schramm, 1977] assumes that the density of the universe is uniform during the nucleosynthesis that took place around 10^9 K and a few minutes after the big bang took place. This model can only account for the synthesis of four isotopes (^{2}H, ^{3}He, ^{4}He, and ^{7}Li) compared to the observed abundances. Figure 1.1 shows the mass fraction of light elements produced in the standard big bang model as a function of the present baryon density, ρ_B. The present baryon density is deduced from the experimentally-determined abundance of certain isotopes. For example the present ρ_B value from D/H and ^{7}Li/H was determined to be roughly 5*10^{-31}gcm^{-3} [Rolfs and Rodney, 1988][Spite, 1982]. This baryon density value implies the total density of normal matter in our universe as $\rho/\rho_c = \leq$ 0.10 and the universe is open. This suggests the universe will forever continue to expand yet other measurements show the universe is closed or nearly so and that majority of the baryons needed for a closed universe is missing. In particular Zwicky showed in 1937 that the mass needed to gravitationally contain star clusters could not be accounted for by the observed masses of the stars when he analyzed he Doppler velocities of whole galaxies within the Coma cluster, hence the original dark matter problem [Zwicky, 1937]. The Wide Field Planetary Camera of the Hubble Space Telescope, has been used to shows a cluster of Galaxies, known as Abell 2218. Together with these galaxies, this cluster contains a great deal of dark matter (a mixture of hot

hydrogen gas and non-baryonic dark matter). These kind of dark matter can be indirectly detected by a method known as gravitational lensing which was predicted by Einstein's general theory of relativity [Turner, 2000].

Today, baryons are found in dark stars, bright stars, cold gas, etc. The light elements made in BBN defined a region for the baryon density, [Turner, 2000] where the predicted and measured abundances of all four light elements were consistent, $0.007 < \Omega_B h^2 < 0.022$ [Copi,1995].

The range of Ω_B was close to 10 with Hubble constant uncertainty, the BBN determination of the baryon density was still reasonable until new results [Mohr, 1999] now show that the dark, non-baryonic matter accounts for 30 $\pm$ 7% of the critical mass and energy density, with baryons (most of which are dark) making up only 4.5 +-1% of the critical density, and "dark energy" the remainder [Turner, 2000].

During BBN, the three light elements that were made in small amounts were D, ^{3}He, and ^{7}Li. Among the three, deuterium was deemed the "baryometer" because its existence directly depends on the baryon density. It is important to note that, even though BBN predictions are pretty good, there is evidence to suggest that the current values for ^{6}Li and ^{7}Li are inconsistent. This partially has to do with accuracies in reaction rates and relevant astrophysics cross sections measured [Olive, 2000]. Some of the relevant astrophysics reactions (fig. 1.2) include: d(d,γ)^{3}He, n(p,γ), ^{7}Li(d,n)^{4}He and t(d,n)^{4}He. We plan to measure some of these or analog reactions utilizing our special deuterated liquid scintillators.

1.1.3 Radiative Capture Reactions

Nuclear reactions in which the incident projectile is absorbed by the target nucleus and γ radiation is then emitted are known as radiative-capture reactions A(x,γ). As a group, reactions of this kind are of enormous importance in astrophysics (fig 1.2) including BBN and particularly stellar nucleosynthesis [Rolfs and Barnes, 1990]. Many nuclear features such as the collective band structure and origin of enhanced multipole decays, and the spectroscopic properties of nuclear states can be deduced with radiative-capture reactions. Such spectroscopic factors in turn will give information about nuclear level densities and level fluctuations. However, there are some difficulties with radiative capture. The cross sections are generally very small hence making it a difficult task to measure them experimentally.

As a result of A(x,γ)B having small cross sections, a high beam intensity and pure and stable targets are needed to study such reactions. For the aforementioned reason, we often now study these very difficult reactions using "analog reactions". For example the (d,n) reaction is an analog to (p,γ) radiative-capture reaction. It is important to note that, recoiling nuclei B produced in a radiative capture or (d,n) will most likely be in the same direction as the beam. Having a neutron as the outgoing particle in (d,n) requires an effective neutron detector and we have designed, constructed and tested one for the purpose of accomplishing that task.

1.2 Goals of Thesis

For this thesis, the goal was to design, build and test a neutron detector that could be used to study (d,n) and other radioactive beam reactions such as (^{3}He,n) and (^{6}He, ^{5}He). The goal was to eventually use these detectors to investigate such reactions on ^{8}Li, ^{7}Be, ^{6}He or other exotic nuclei. These unstable nuclei are produced

as secondary beams at the Nuclear Structure Laboratory (NSL) at the University of Notre Dame using the UM-UND *TwinSol* RNB apparatus [Becchetti, 2001]. A detector capable of detecting neutrons between 5-20 MeV was required. This posed some problem for the traditional CH_2 (plastic) neutron detectors that require a long flight path to deduce the neutron energy via time-of-flight (ToF). These traditional scintillators have several drawbacks such as: low energy resolution, unable to discriminate between neutrons and gammas without ToF, not optimal for use with secondary RNBs, and unable to discriminate cosmic ray muons. Liquid hydrogen-based scintillators are likewise limited as they do not yield neutron energy without ToF. For this reason a new liquid scintillator based on C_6D_6 was studied. It was suggested in 1981 by P.M. Lister et. al., that C_6D_6 could be used for neutron spectroscopy and in particular (d,n) reactions because of several unique features [Lister, 1981]. C_6D_6 has the capability of good n/γ pulse shape discrimination and neutron energies can be obtained without the use of the time-of-flight technique.

This thesis is divided into the following sections: Chapter 1: Gives a general introduction of what was intended; Chapter 2: Describes the building and setup of the liquid scintillators; Chapter 3: Describes the calibration of the detectors with gamma sources and DD and DT neutron generators; Chapter 4: Describes the (d,n) nuclear reactions studied with the detector as a feasibility test; Chapter 5: Details the results from the various reactions including the cross sections deduced ; Chapter 6 gives the conclusions and possible future work; Appendices give details of the Monte Carlo simulations performed together with Marek Flaska and Shaun Clarke at UM using MCNP-Polimi, give details of the CAMAC-based data acquisition system used for measurements done at UM, and has data for the PMT and bases used.

CHAPTER II

Scintillation Detection Principles

The scintillation detector is one of the most versatile radiation and particle detection devices used in nuclear and particle physics. It uses the fact that certain materials, when struck by a neutron, photon or charged particle, emit a small flash of light. When coupled to an amplifying device, such as the photomultiplier tube (PMT), this scintillation can then be converted into electrical pulses that can then be analyzed and counted electronically to give information about the incident radiation.

The first use of scintillation counters for particle detection dates back to the 1903 spinthariscope, invented by Crookes [Crookes, 1903]. This device consisted of ZnS screen that produced weak scintillations when struck by α-particles. When viewed under a microscope, one can see the scintillation events. The process was fairly difficult, hence it never really garnered attention even though the famous Marsden and Geiger α scattering experiment used it [Leo, 1987].

It was not until 1944 that Baker and Curran [Baker and Curran, 1944] brought back the scintillator by employing the newly-developed photomultiplier tube. The weak scintillation could now be counted with efficiency and reliability that in some cases surpassed that of the typical gas counters in wide-spread use. The new improvements and development was so rapid that, by the 1950s, scintillation detectors were

the most reliable and widely used devices for particle detection, including neutron detection.

Although no single scintillation material meets all the requirements for a particular detector, a good scintillator should have the capability to convert kinetic energy of particles into detectable light with high scintillation efficiency. The light yield should be proportional to the deposited energy over as wide a range as possible. The material should be of good optical quality, i.e. it's index of refraction should be close to that of glass ($\sim$1.5) to allow good coupling of the scintillation light to a photomultiplier tube. It should have a short decay time and a fast rise time to allow fast radiation counting and time-of-flight measurements [Knoll, 2000]. The scintillator should permit one to distinguish between incident particles and x-rays or gamma rays.

2.1 Scintillators

Organic scintillators contain aromatic hydrocarbon molecules that have vibrational excited states which can be initiated by ionizing radiation. Their most unique feature is a very rapid decay time on the order of a few nanoseconds.

Scintillation light in these compounds comes from transitions of free electrons in the molecules. The electrons are independent of any atom in the molecule and occupy what is known as the π-electron structure. The π-electron structure of a typical molecule is shown in figure 2.1. Energy can be absorbed by exciting the electron configuration into any one of a number of states [Leo, 1987]. From figure 2.1 one can see that a series of triplet (spin 1) electronic levels are shown as T_1,T_2, while the singlet states (spin 0) are labeled as S_0, S_1. The energy spacing between electron levels is on the order of a few eV whereas that between the vibrational levels is of the order of a few tenths of eV.

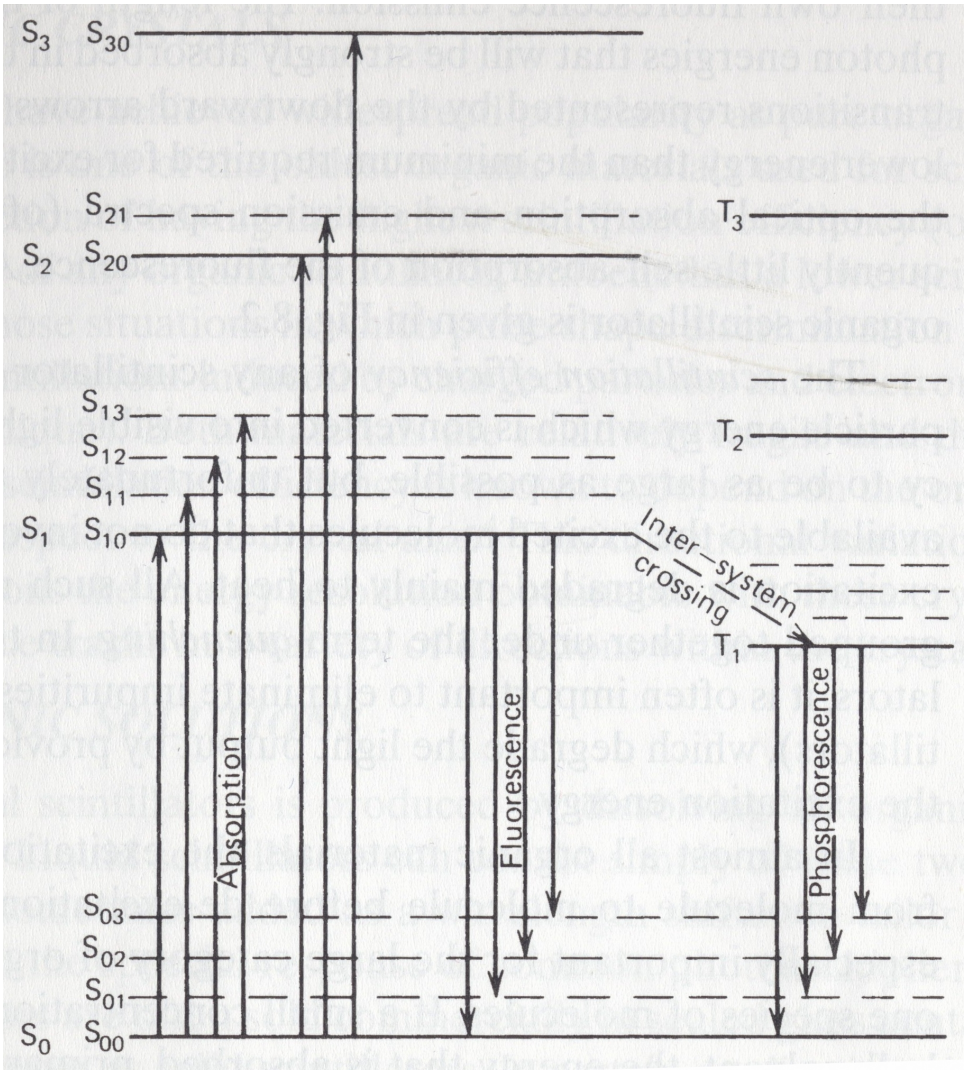

Figure 2.1: Energy levels of an organic molecule with π-electron structure [Knoll, 2000].

The principle scintillation light is emitted in transitions between S_{10} and one of the vibrational ground states. The downward arrow in the π-electron figure indicates the transition between these states. If τ represents the fluorescence decay time for the S_{10} level, then the prompt fluorescence intensity at time t following the excitation will be represented by the equation [Birks, 1964]:

$$I = I_0 e^{-t/\tau} \tag{2.1}$$

In most organic scitillators, τ is a few nanoseconds, and the prompt scintillation component is relatively fast.

2.1.1 Organic Crystals

Only two materials, anthracene ($C_{14}H_{10}$) and trans stillbene ($C_{14}H_{12}$) have achieved widespread popularity as pure organic scintillator crystals. Anthracene is believed to have the greatest light output per unit energy while stillbene has much lower efficiency. Stillbene is favored for situations where pulse shape discrimination (PSD) is required. Both materials are relatively brittle and difficult to handle in large sizes [Klein and Brooks, 2006].

2.1.2 Organic Liquids

Organic liquids are liquid solutions of one or more organic scintillators in an organic solvent. While the scintillation process is the same as for the other scintillators, the energy absorption mechanism is different. In liquids, the ionization energy is mainly absorbed by the solution and then transported to the scintillation solute. This transfer usually occurs quickly and efficiently, though the precise mechanism still is not well known. The response of liquid scintillator is usually very fast with

decay time on the order of 3 to 4 nsec and the rise time is a few nsec. They have a particular advantage in that they easily can be mixed with other materials to increase the neutron detection efficiency. Liquid scintillators also generally are very sensitive to impurities within the solvent [Marion and Fowler, 1960] .

2.1.3 Plastics

Plastic scintillators are the most widely used of all the organic scintillator detectors. Like the organic liquids, plastic scintillators also are solutions of organic scintillators but in solid plastic. Signals are extremely fast with a decay constant of about 2-3 nsec and rise times of 1-3 nsec, and they can have a high light output. Due to the fast decay time, the rise time becomes very critical. Bengtson and Mostzynkski [Bengtson and Moszynski, 1970] give the best mathematical description for the rise time of plastic scintillators.

$$N(t) = N_0 f(\sigma, t) e^{-t/\tau} \tag{2.2}$$

where f(σ,t) is a Gaussian with a standard deviation σ. Different plastic will have different standard deviations σ and hence rise times.

2.1.4 Inorganic Scintillators

The inorganic scintillators are mostly crystals of alkaline materials grown in a high temperature furnace containing a small impurity activator. NaI(TI) is by far the most commonly used material for such scintillators, followed by CsI (Tl). These scintillators have an advantage of having a high stopping power because of their high density and atomic number. This makes them particularly well suited for γ-ray detectors [Knoll, 2000][Gilmore and Hemingway, 1995]. They also can be easily cut to

smaller sizes to provide good position sensitivity. They are widely used in medical and health physics to detect gamma rays and x-rays. However, these scintillators absorb water and must be encapsulated. Other materials that have gained attention from nuclear and high-energy physicists are the BGO and BaF_2. BGO is particularly unique because of its high Z atoms and greater efficiency for conversion of photoelectrons from gamma rays. Unlike NaI(Tl) and CsI (Tl), BGO and BaF_2 do not absorb water and can be used without water-tight encapsulation. The spectral output for a C_6H_6 or C_6D_6 scintillator is very similar to that of NaI and CsI shown in figure 2.2.

2.1.5 Gaseous Scintillators

Gaseous scintillators consist of nitrogen or noble gases like argon and helium. For these scintillators, the atoms are individually excited and then return to their ground states. The scintillation process is a result of a single charged particle interacting with an added scintillate. This de-excitation is usually very rapid (on the order of $\sim$ 1 nsec), hence the detector usually has a fast response.

2.2 Scintillator Light Output Response

The light output of a scintillator L is determined by the scintillator's efficiency for converting ionization energy into photons detectable by a PMT [Eichholz and Poston, 1982]. A tiny part of the kinetic energy of a charged particle, x-ray, or γ-ray is lost in the scintillator and converted to fluorescent light. The remainder is usually dissipated either in the form of heat or molecular vibrations that do not make light or from the particle or photons escaping after an initial scattering event. In practice, the light output is different for different types of particles at the same energy.

For organic scintillators, like anthracene or stilbene, the response to electrons is linear for electrons above 125 keV [Brannon and Olde, 1962]. The response to

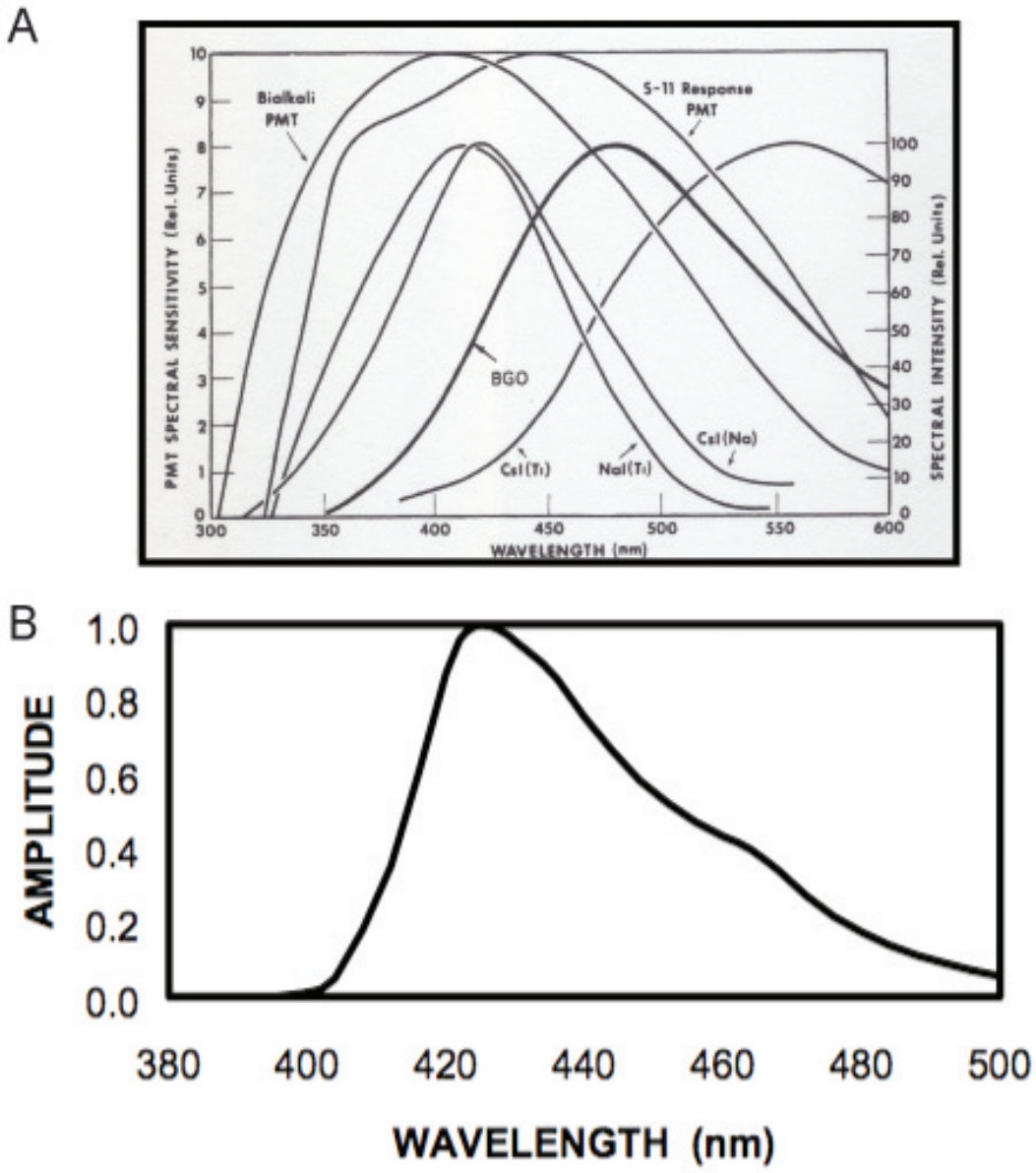

Figure 2.2: (A)PMT response and light emission spectra for different inorganic crystals [Knoll, 2000] (B) C_6D_6 emission spectrum [Eljen Technology web page].

heavier charged particles such as protons is significantly less for the same energies and nonlinear (figs. 2.3 to 2.5). The response of scintillators is a complex function of not only the particle's energy, but also the type of particle and its unique ionization. Figure 2.3 shows a typical organic plastic scintillator response to both protons and electrons [Smith, 1968].

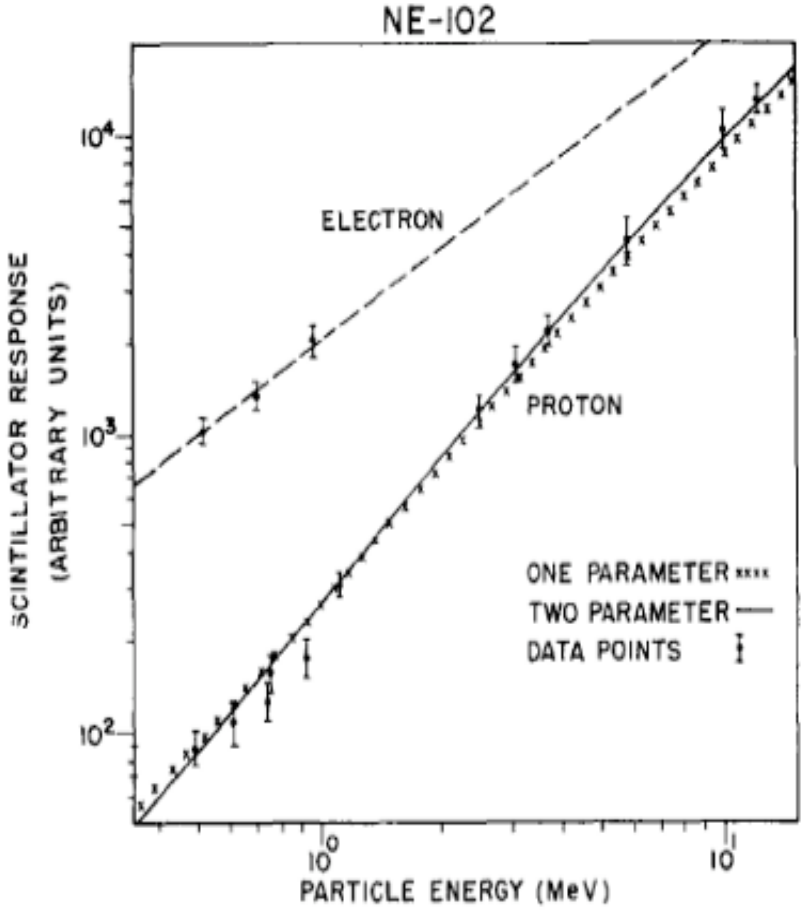

Figure 2.3: Response of NE-102 plastic scintillator to electrons and protons [Smith, 1968].

J. B. Birks was the first to put forward a good semi-empirical model to explain the behavior of these scintillators [Birks, 1964]. He assumed the intrinsic response of organic scintillators to be linear and further explained the deviations as due to quenching interactions of the molecules created in the path of the incident parti-

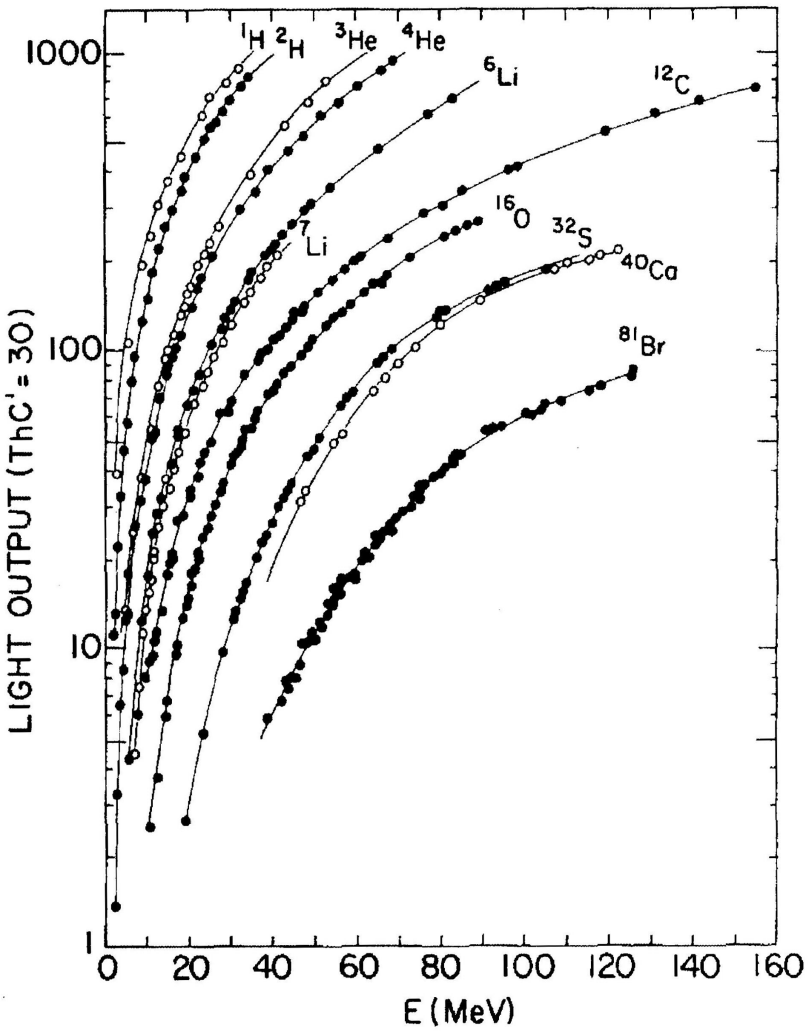

Figure 2.4: NE102 plastic scintillator response to heavy ions [Becchetti, 1976].

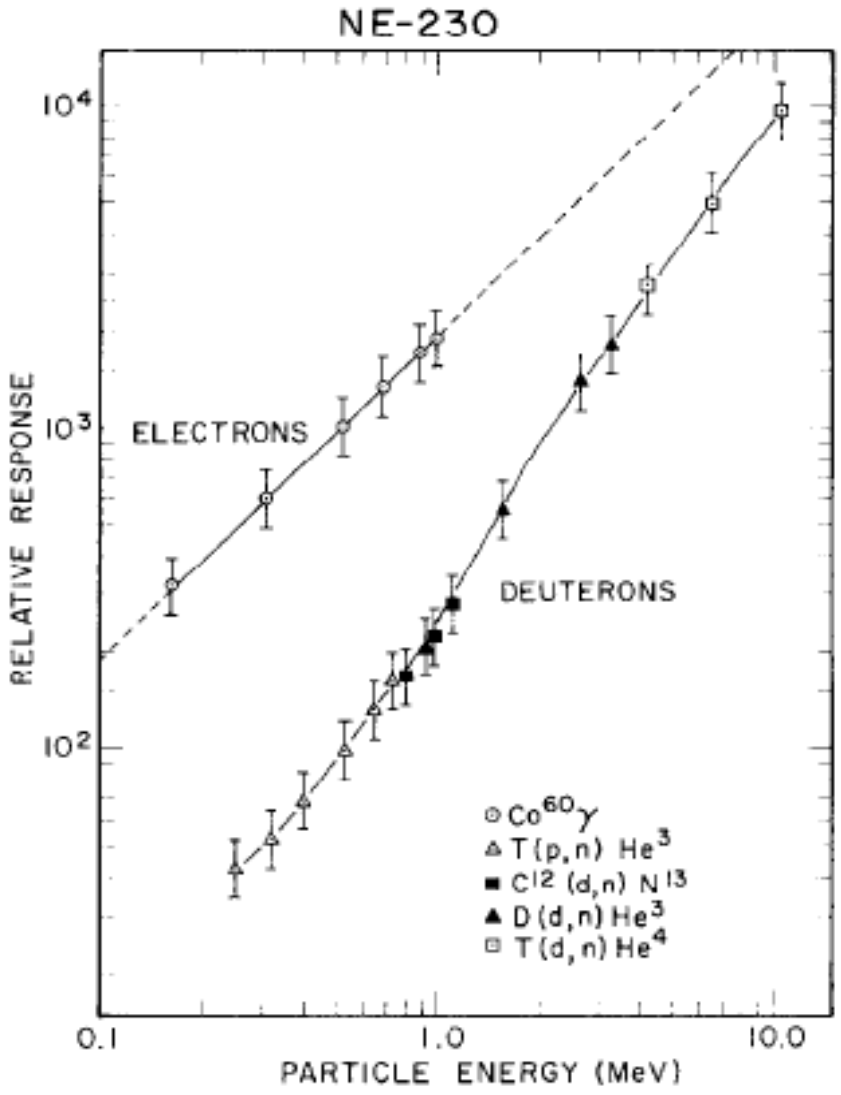

Figure 2.5: Response of a C_6D_6-equivalent (NE-230) liquid scintillator to electrons and deuterons [Smith, 1968].

cle. This interaction decreases the apparent energy, which would otherwise create scintillation light.

More quenching interactions will take place when higher local ionization produces a higher density of the excited molecules. For this model, the light output per unit length, dL/dx, is related to the specific ionization dE/dx of a particle by

$$\frac{dL}{dx} = \frac{A\frac{dE}{dx}}{1 + kB\frac{dE}{dx}} \tag{2.3}$$

where A is the absolute intrinsic efficiency; kB is the quenching parameter that relates the density of ionization to $\frac{dE}{dx}$. The kB parameter is obtained by fitting Birks' formula to experimental data.

When excited by fast electrons or high-energy charged particles, $\frac{dE}{dx}$ is small and Birks' formula then predicts

$$\frac{dL}{dx} = A\frac{dE}{dx} \tag{2.4}$$

This is the region where the light output is linearly related to the initial energy of the incident electron or particle:

$$L \equiv \int_0^E \frac{dL}{dx} dE = AE \tag{2.5}$$

While Birks' formulae have been reasonably successful, deviations have made it important to turn to higher orders to allow a better fit to data. Several scientists have proposed different equations for L and $\frac{dL}{dx}$. These equations, in general, introduce additional fitting parameters to that of Birks. Becchetti used the Murray-Meyer model to interprete the scintillator response data for heavy ions [Becchetti, 1976]. Craun and Smith have done extensive analysis of organic scintillator response using

the data of Smith, Polk and Miller. [Smith and Craun, 1970][Smith, Polk, and Miller, 1968] Their analysis used an extended version of Birks' equation

$$\frac{dL}{dx} = \frac{A\frac{dE}{dx}}{1 + kB\frac{dE}{dx} + C(\frac{dE}{dx})^2} \tag{2.6}$$

where C is again an empirically-fitted parameter.

The response of the popular plastic NE102 plastic scintillator to several heavy ions as measured by Becchetti et.al is shown (figure 2.4).

We can see from figure 2.4, that the light elements appears to experience a much faster decrease in the light output with decreasing energy. The response of a C_6D_6 liquid scintillator equivalent (NE-230) to both electrons and deuterons is shown in figure 2.5 [Smith, 1968]. From figure 2.5, one sees that light yield for electrons is much more than that for deuterons.

2.3 Deuterated Liquid Scintillator

As will be shown below, the proton-recoil scintillators used to detect fast neutrons that are widely used in nuclear structure experiments suffer from difficult lineshape unfolding, particularly for neutron energies above a few MeV. It has been suggested that a fast neutron scintillator with a better capability to unfold lineshapes would be beneficial and ease data analysis. Proton-recoil detectors exhibit step-function lineshapes because the cross section in the center-of-mass frame for n-p elastic scattering at MeV energies is symmetric around 90 degrees. The recoil proton energy for such detectors is related to the scattering cross-section in the center-of-mass frame:

$$L(E) = \frac{K}{E}\frac{d\sigma}{d\Omega_{cm}} \tag{2.7}$$

Where K is a constant determined by the mass of the incident and target particles and E is the energy of the incident neutron.

2.3.1 n+p vs. n+d Cross Section

Typically in a hydrogen-based neutron scintillator, the simplest interaction is that of n+p elastic scattering. This reaction is isotropic in the center-of-mass frame for energies up to 10 MeV and beyond (fig. 2.8). Monoenergetic neutrons at and below this energy incident on a standard hydrogen-based scintillator will produce a nearly flat pulse height distribution (i.e. a step function) [Leo, 1987], going from zero to the maximum energy of the incident neutron. This is particularly difficult to analyze when neutrons from nuclear reactions interact with the scintillator as it will give rise to several step functions corresponding to different neutron energies superimposed on each other (figure 2.6). It is difficult to unfold such spectra. Thus it was suggested to use a deutereted scintillator. Unlike n+p elastic scattering, the n+d scattering between 2 and 20 MeV is not symmetric around 90 degrees in the center-of-mass. It has a sharp backward peak resulting in a forward recoil deuteron peak, thus making it possible for the scintillator light output L to have much of the incident neutron energy. A plot of adopted n+d elastic cross sections for three different energies (E = 12 - 21 MeV) is shown in figure 2.7. It is obvious from figure 2.7 and even data at higher energies, figure 2.9, that the cross-sections have a dip at about 120^o. Thus there is a pronounced peak in the C_6D_6 detector response to neutrons above 1 MeV. The forward recoiling deuteron peak in the deuterated scintillator gives it two major advantages over the proton-recoil scintillator: (1) it allows one to work with the spectra directly without complicated unfolding; (2) one can identify, directly from the raw data, the lower-lying states that are being populated in the residual nucleus

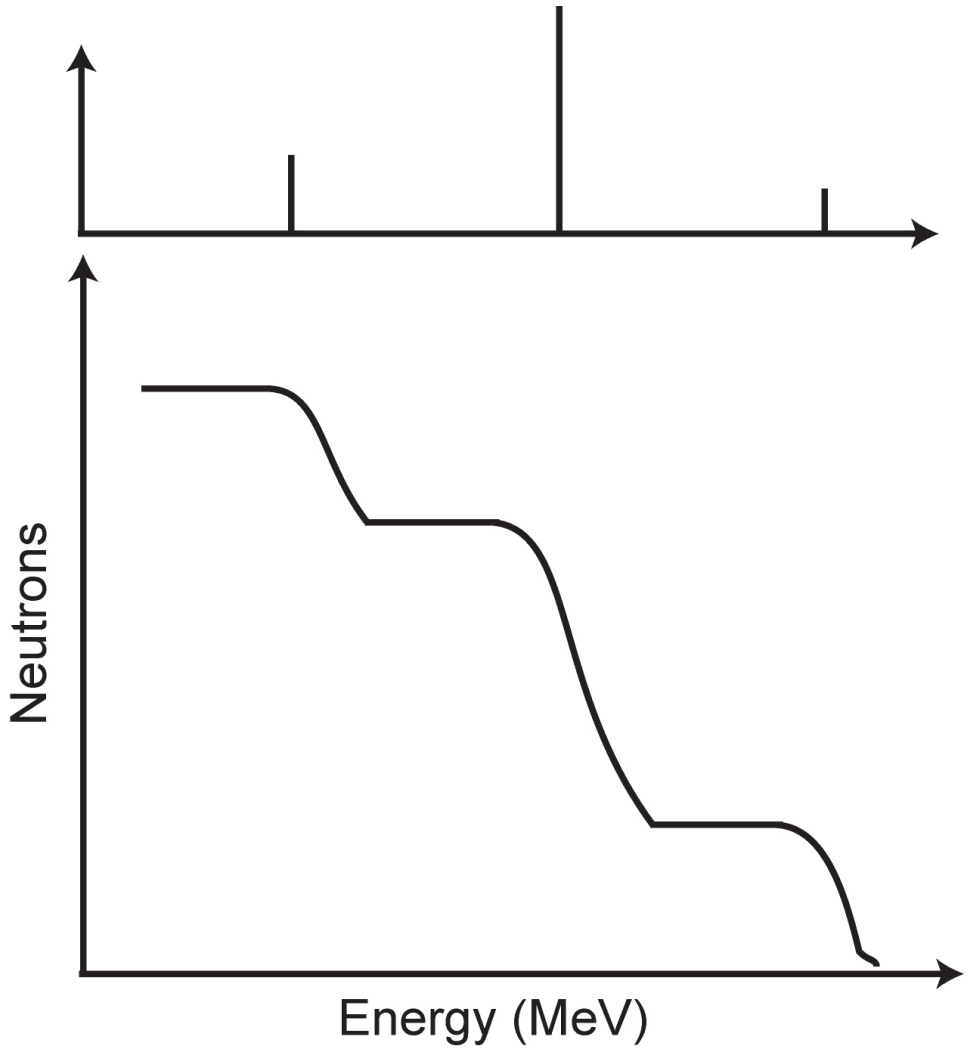

Figure 2.6: Expected C_6H_6 detector response including typical detector resolution (bottom) to three different (top) neutron energies [Lister, 1981].

and determine cross sections.

The light output of a deuterated scintillator can be calibrated in neutron energy by bombarding the scintillator with monoenergetic neutron beams. In cases where this occur, the recoil deuterons are produced due to elastic neutron-deuteron scattering. By studying the entire recoil spectra obtained at different incident neutron energies, the scintillator response curve to neutrons of various energies can be determined.

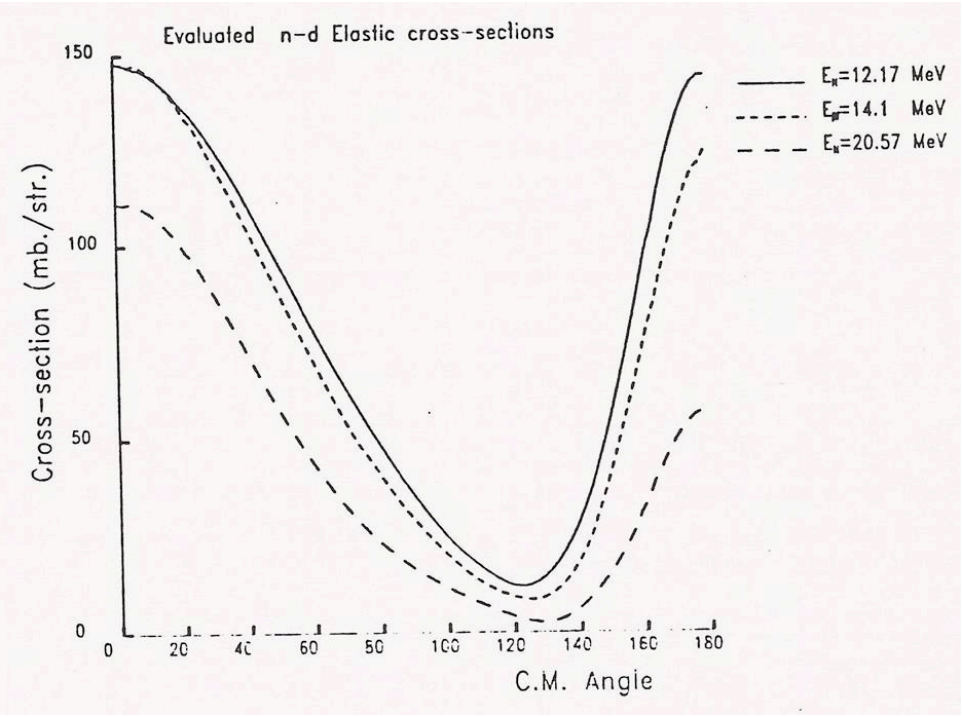

Figure 2.7: Adopted n-d elastic scattering cross sections [Lister, 1981].

For the experiments planned for this research, some criteria had to be met for the chosen scintillator:

1. The neutron energies must be deduced without time of flight.

2. Spectra must be easy to work with.

3. Must separate nuclear reaction energy states from the neutron spectra.

4. Must discriminate between neutrons, gamma rays and cosmic-ray muons.

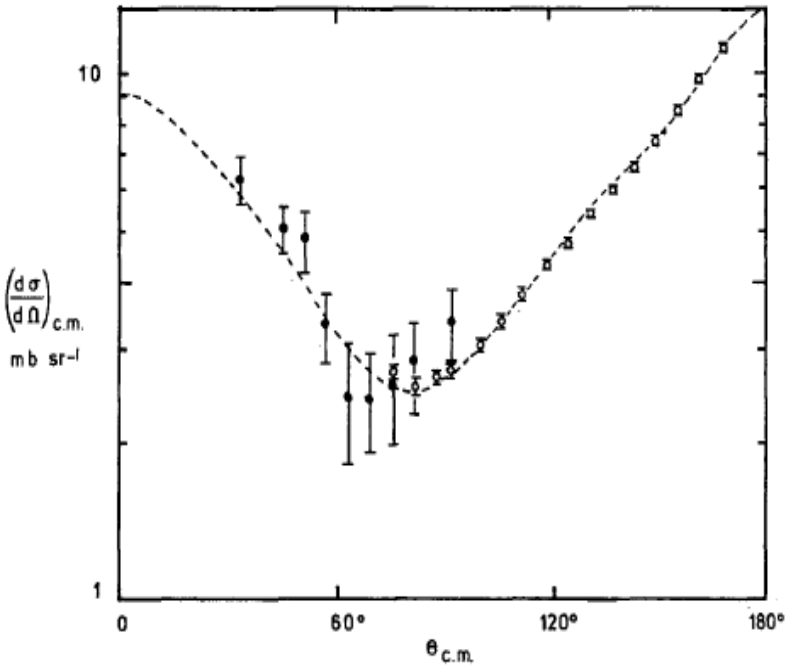

Figure 2.8: n-p elastic scattering cross section, E near 130 MeV [Howard, 1974].

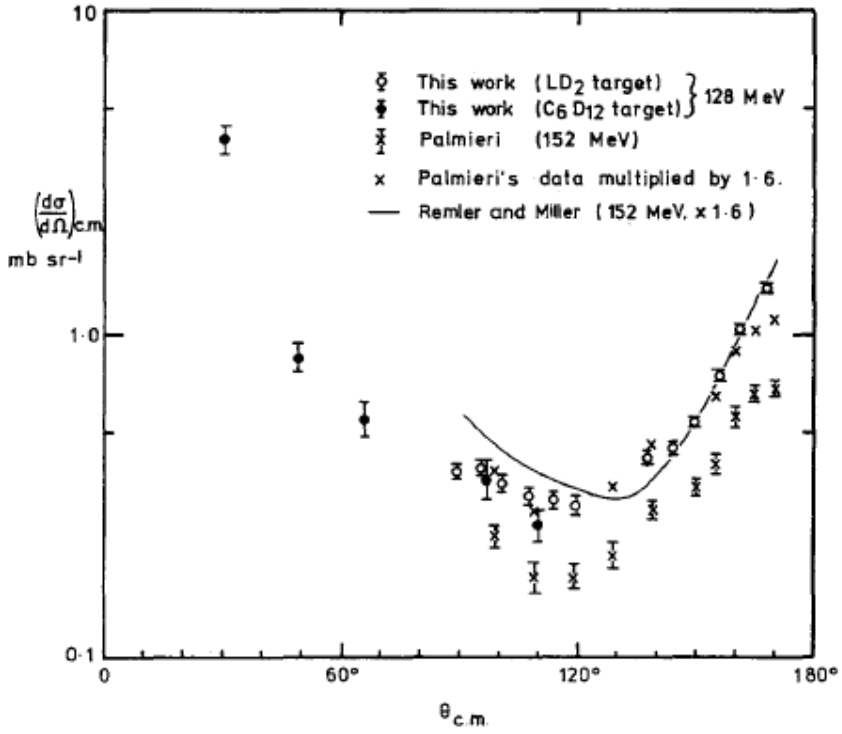

Figure 2.9: High-energy n-d elastic scattering cross sections [Howard, 1974].

Deuterium-based scintillators are by no means easier to work with than proton-recoil scintillators. In fact, they can be somewhat more complex than a proton-recoil detector. This is because the n-d interaction can result in a three-body breakup reaction of the form D(n,2n)p. At low energies, most of the experimental features a deuterated scintillator exhibits can provide energy information about the recoiling charged particles [Tornow, 1985]. This produces pulses of various apparent neutron energies in the scintillator, hence pulse-shape discrimination must be use to distinguish between Compton electron pulses from γ rays and deuteron recoil pulses, and also between proton and deuteron pulses. Because very little information is available on its response to charged particles, a detailed knowledge of the response of the scintillator to recoil deuterons as well as protons, which are produced in the breakup process, is required. For the experiments covered in this work, four C_6D_6 detectors were used with a C_6H_6 detector used for comparison. A Monte Carlo code (MCNP-Polimi) was written to simulate the detector's response to neutrons and gamma-rays at different energies.

2.4 Mounting Encapsulated C_6D_6 and C_6H_6 Detectors

The main components of the scintillator detectors are the encapsulated detector, the optical coupling, the photomultiplier tube (PMT), and the PMT base. The encapsulated C_6D_6 and C_6H_6 detectors were purchased from Eljen Technologies in Sweet Water, TX. The complete specifications for both the C_6D_6 and C_6H_6 detectors are listed in tables 2.1 and 2.2.

Upon their arrival at the University of Michigan (March, 2008), I assembled the detectors with PMTs and tube bases to make them functional. A few things had to be done before mounting the scintillators to a PMT. The scintillator came with a small

C_6H_6 Hydrogen Scintillator Properties	
Light Output (% Anthracene)	78 %
No. of Blue Photons per 1 MeV of Electron Energy	12,000
Wavelength of Maximum Emission	425 nm
Specific Gravity (g/cc)	0.874
Atomic Ratio, H:C	1.212
No. of H Atoms per cm^3	4.82 x 10^{22}
No. of C Atoms per cm^3	3.98 x 10^{22}
No. of Electrons per cm^3	2.27 x 10^{23}
Flash Point (T.O.C.)oo	26^oC (79^oF)
Refractive Index, n_D	1.505
Decay Time (short component)	3.2 ns
Mean Decay Times of First 3 Components	3.16, 32.3 and 270 ns
No. of Photoelectrons per Kev energy loss using an RCA-8575 PMT	1.7
Alpha/Beta Ratio, "fast"	0.073
Alpha/Beta Ratio, slow"	0.098

Table 2.1: C_6H_6 Detector Properties.

C_6D_6 Deuterated Scintillator Properties	
Light Output (% Anthracene)	60 %
No. of Photons per 1 MeV of Electron Energy	9200
Wavelength of Maximum Emission	425 nm
Specific Gravity (g/cc)	0.954
Atomic Ratio, D:H	141
No. of D Atoms per cm^3	4.06 x 10^{22}
No. of H Atoms per cm^3	2.87 x 10^{20}
No. of C Atoms per cm^3	4.10 x 10^{22}
No. of Electrons per cm^3	2.87 x 10^{23}
Flash Point (T.O.C.)oo	-11^oC (12^oF)
Refractive Index, n_D	1.498
Decay Time (short component)	3.5 ns
Boiling Range	79^oC
Bulk Light Attenuation Length	$>$ 3 meters

Table 2.2: C_6D_6 Detector Properties.

mu-metal magnetic-field shield for the tube that had to be screwed very carefully to the scintillator cells while making sure the scintillator cell window remained intact. Also as described below, the tube base had to be slightly modified to fit the detector assembly.

2.4.1 Photomultiplier Tubes

The PMT we used with the scintillators was the RCA 8575 PMT. The PMT is a 2-inch (50mm) diameter, 12-stage end-window photomultiplier with a bialkali

(K-Cs-Sb) photo-cathode, a pyrex faceplate, and an in-line electrostatically focused copper-berryllium dynode structure (see Appendix E). This tube was chosen because of its high quantum efficiency, high current amplification, low dark current and good timing characteristics. In addition, several of these tubes were available along with fast-timing PMT bases (Ortec 265) from past nuclear research projects.

First, several PMTs were tested with high voltage to make sure they worked properly. As noted the PMTs were attached to an Ortect 265 PMT fast timing base. These had to be slightly modified to accommodate the mechanical dimensions of the scintillator cells. The Ortec base (see Appendix E) provides a simple mechanical assembly and resistive voltage divider network, with the appropriate capacitor decoupling, for the operation of the RCA-8575. Also, this base helps to maintain good pulse fidelity and timing over a wide range of signal currents.

Extreme care was taken not to break the scintillator cells. The scintillator was encapsulated in the Eljen type VM cells which consist of a 50 mm x 50 mm cylindrical aluminum body with a 6 mm thick optical window and sealed under inert gas [Eljen web page]. This was important because of the toxic nature of benzene. A small thermal expansion volume was included which resulted in a fill-factor of about 90%. Before mounting, the scintillator surface and the PMT were cleaned with alcohol. A bit of optical grease supplied by Eljen (EJ-552 Dow Silicon) was then put onto the center of the PMT. Optical epoxy which is more secure was not used so the PMTs could later be replaced if needed.

The PMT was then pressed onto the scintillator so that the grease spread radially to make a smooth, thin optical coupling of the entire surface of the scintillator to the PMT which could compromise the optical coupling. The RCA 8575 PMT was mounted horizontally on the scintillator. Care was taken to make sure no air space

was left between the cell and the PMT. The optical grease used had an index of refraction close to that of the scintillator window (roughly 1.5). The scintillator coupled with the PMT was then attached to the PMT base for the initial test of a complete detector. To further ensure there was no accidental light leak from the scintillator, PMT and base, the complete detector assembly was wrapped with 3M black electrical tape.

Figure 2.10 shows the individual stages just described. Each of the detectors had a custom mu-metal shield (figure 2.10) to cancel the fringe field from the earth and from *TwinSol* (B $\approx$ 100 gauss).

Figure 2.10: Mounting the scintillator.

2.4.2 PMT Time Response and Resolution

There are two factors that usually affect the time resolution of the photomultipliers: the fluctuations due to statistical noise relative to the signal (S/N), and the variations in the transit time of the electrons through the photomultiplier, including the natural fluctuations in photomultiplier current due to statistical nature of the photoelectric effect and the secondary emission processes. Noise (S/N) is one of the limitations of time resolution with any photomultiplier. The transit time variation

may occur because of the differences in path length traveled by the electrons in the PMT and in the energy with which they are emitted by the photocathode [Leo, 1987]. It is important to note that this difference is enhanced by the asymmetry of the dynodes. It is obvious that the electrons that are emitted at one section could have a longer distance to travel than those emitted at another section. There also is variations due to the direction of the emitted electron and their energy after acceleration between the dynodes. These factors determine the selection of particular photomultiplier tubes based on experimental testing of each PMT. This is very important, for every scintillator to transmit photons effectively, the PMT must be optimal and working properly. I therefore tested several RCA-8575 PMTs and selected the best ones for mounting on the scintillator cells.

CHAPTER III

Neutron Detection

The neutron is a subatomic particle with no electric charge and with a mass close to that of a proton, its iso-spin partner. In fact, its mass only is about 2 percent larger than that of the proton and hence a free neutron will decay to a proton with emission of an electron. When bound in stable nuclei, neutrons are stable, but unstable when free in nature. It undergoes beta decay with a half life of just under 15 minutes (886 seconds). As noted, the number of neutrons in an element determines the isotope of that particular element.

Common with x-rays and gamma rays, is the lack of charge of the neutron. This makes the neutron extremely difficult to detect. It cannot interact by means of the Coulomb force, which dominates the energy loss for charged particles. Instead neutrons must be detected by means of a nuclear interaction that give rise to secondary charged particles. The required information must then be deduced from the properties of the secondary charged particle [Knoll 2000]. This is the technique used by J. Chadwick [Chadwick, 1932] to detect the neutron via the detection of a recoil proton. The late date of this discovery reflects the difficulty (still) in detecting neutrons.

There are many nuclear reactions involving neutrons as the scattered particle and many detectors are available for neutron detection. However, because the reaction

probability is highly dependent upon the neutron energy, different techniques must be employed for different neutron-energy regions. It is important to note that for nuclear-structure studies involving neutron energies above 1 MeV, a recoil-proton spectrometer of some type is almost universally used [Birks, 1964].

Organic scintillators are particularly useful for neutron detection because of their high hydrogen content and the large sizes available, especially for plastic scintillators. Two methods are usually employed with these scintillators for spectroscopic applications: the time-of-flight (ToF) method and the recoil-proton method. For the time-of-flight application, the detector only is used for timing information triggered by detection of the recoil proton. The energy information is deduced from the target-to-detector flight time (ToF). This technique has the disadvantage of requiring a long flight path (often tens of meters) in order to obtain good neutron energy resolution, with a corresponding loss in solid angle unless a "wall" of scintillators is used [Kolata, 2006]. This makes the ToF method only useful when there is expansive experimental area and high accelerator beam current. Even then, the range of scattering angles can be limited.

The presence of signals due to gamma rays is a major problem in all neutron detection systems. Because the ToF method involves velocity measurements, it is usually possible to discriminate between neutrons and gammas since the latter will appear in a well defined group with v=c and thus easily can be identified. This is the most important advantage of the ToF system over others. However, cosmic ray muons which are random in time and hence ToF, and give large scintillation signals, can be a major source of background, especially for low-cross section measurements. The latter often is the case for RNB experiments which use low-intensity ($< 10^7$/s) secondary beams [Lee, 2002].

As noted, organic scintillators are known for their excellent timing characteristics, especially in rise time and hence ToF resolution. This has made their application with ToF almost universal. Other sophisticated timing methods also have been developed to take advantage of this unique feature [El-Salem, 1970] [Nutt, Gedcke and Williams, 1970].

The proton-recoil method requires a pulse-shape discrimination technique to identify neutrons in the presence of γ-rays or cosmic-ray muons where ToF cannot be used. In situations where space is limited, the proton-recoil scintillation counter may be useable without ToF. In this case, as discussed earlier, the neutrons impinge on a light target nucleus within the scintillator, and pulses due to the recoil of the nucleus are then recorded. The obvious observation is that the scintillation pulses will not necessarily be related to the energy of the incident neutrons, but will reveal a distribution dependent upon the kinematics of the neutrons and the target nucleus interaction. Then it becomes imperative to know the interaction kinematics before hand so one can extract the neutron spectra from the observed pulse-height distribution.

One of the simplest interactions is that of n-p elastic scattering, which as previously noted is isotropic in the center of mass for neutron energies up to 10 MeV. Monoenergetic neutrons at and below this energy, give rise to a flat scintillation pulse height distribution extending from zero energy up to the energy of the incident neutrons [Knoll, 2000]. Hence, neutrons coming from nuclear reactions, with several energy groups, will give rise to step functions superimposed on one another as shown in figure 2.6 [Lister, 1981] [Burrus and Verbinski, 1969]. Computer codes were developed to address such spectra and some recent developments have made it possible to further unfold more complex line shapes [Straker, Burgart, Love and

Freestone, 1971].

Because n-p elastic scattering results in simple step functions, the computer code used for analysis initially has to work with a portion of the spectrum, rather than the entire spectrum, to identify the edge that corresponds to the neutron groups [Brooks, 1979] [Brooks, 1980]. For the aforementioned reasons, and for the nuclear (d,n) experiments planned, some requirements must be met for the detector in addition to those noted earlier. These are:

1. It must be able to detect neutrons between 2 and 20 MeV.

2. It must be relatively inexpensive.

3. It must have good n/γ pulse shape discrimination.

4. It must be reasonably efficient.

3.1 Calibration of Scintillators

3.1.1 Gamma Calibration

The detector response for the detectors used here to several gamma ray sources of known energies was measured. Since there is no distinct photo peak in organic low-Z scintillators, [Knoll, 2000][Schram, 1963], in order to calibrate the measured light output with the actual energy of the recoiling electron, the channel numbers of the Compton edges of several gamma sources were recorded. As noted below, detecting the Compton edges over a wide energy range one can find the linearity (or nonlinearity) of the detector response.

Unlike neutrons, that are detected as a result of recoiling nuclei, gamma rays are detected by measuring the recoil atomic electrons that are struck. The collision energy of the gamma rays causes the electron to recoil and produce light in the

scintillator. The electron light pulse created in the scintillator is proportional to the electron recoil energy in the scintillaor, and hence related to the energy of the incident photon. The energy of the scattered gamma for Compton scattering can be expressed as [Knoll, 2000].

$$E_\gamma = E_0/((1 + (E_0/m_e c^2)(1 - cos(\theta_\gamma))) \tag{3.1}$$

Where E_0 is the energy of the incident gamma ray, θ_γ is the angle through which the electron e^- scatters, and $m_e c^2$ is the rest mass of the struck electron. It is important to note that the energy of the scattered gamma ray is at a minimum when $\theta_\gamma = 180^o$. The electron recoil energy $E_e = E_0$-Eγ has a maximum value at this point, called the Compton edge of the energy spectra. The light output functions of liquid scintillators have been extensively studied and are usually related to the light output function of electrons, which is nearly linear for electron energies greater than 40 keV [Dietze, 1979]. The calibration of the liquid scintillators was done using the gamma sources ^{22}Na, ^{60}Co and ^{137}Cs. Because of the influence of the resolution on the position of the Compton edge, it is vital to know how to select the position used. For this work, the Compton edge was selected by taking the half point between the peak corresponding to the gamma energy and the base due to resolution. Its been shown to be the location where most of the Compton energy within the edge is located. The incident gamma ray energies used for the calibration and the resulting electron recoil Compton energies of the calibration sources are given in table 3.1, while the pulse-height spectra for ^{60}Co and ^{137}Cs γ-source are shown in figures 3.3 and 3.4.

The schematic for the initial test setup is shown in figure 3.1 . The goal was to make sure that each detectors was giving the right signal and responding appropriately. The data were then sent to a CAMAC-based computer acquisition system which provided pulse-height spectra (see section 3.2). This provided energy cali-

Data for gamma sources			
Isotope	Gamma Energy (MeV)	Intensity %	Compton Edge (MeVee)
^{137}Cs	0.662	85.1	0.477
^{22}Na	1.275	99.94	1.154
^{60}Co	1.173	99.97	0.963
	1.333	99.99	1.118

Table 3.1: Data on gamma sources used for scintillator calibration.

bration of the scintillators in terms of the equivalent Compton electron energy (in energy units denoted MeVee).

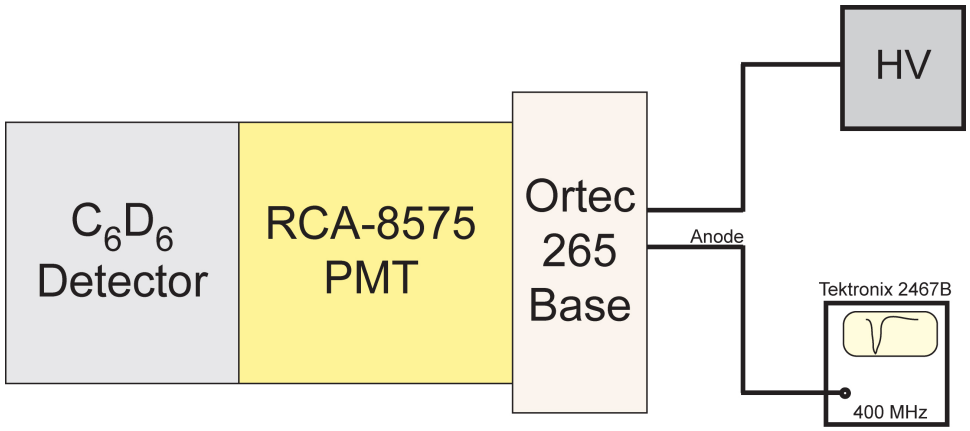

Figure 3.1: Schematic for testing the scintillators.

After this initial test with the last detector was completed, care was taken to make sure the detectors were stored properly and the coupling between the PMT and the scintillator remained intact. The scintillallor were stored horizontally at room temperature. At higher or more humid temperatures, the coupling between the scintillator and PMT can deteriorate or even break. For this reason, the detectors were tested and calibrated with gamma sources each time they were to be used to check that the optical coupling was initially intact. This coupling later proved to be problematic. During some later experiments we discovered that three of the five scintillators decoupled and greatly reduced the wealth of information we were expecting.

3.1.2 Testing the C_6D_6 and C_6H_6 Detectors with Neutrons

The response of direct or recoil deuterons and protons in the scintillator is different from that of the electrons generated by γ-rays. Deuterons and protons emit less light than electrons of the same energy (a pulse-height defect, figures 2.3 - 2.5) and also exhibit a nonlinear response [Smith, 1968]. Monoenergetic neutrons can be produced for calibrations using a low-energy deuteron accelerator, due to the fact that the D(d,n) and ^{3}H(d,n) reactions are quite exothermic (Q=3.26 MeV and 17.58 MeV). The most crucial properties of the sources for monoenergetic neutron production are neutron intensity and neutron energy spread. Factors such as the energy spread of the deuteron projectile, the degradation of the incident beam in the target material, and the angular spread of the emitted neutrons can affect the quality of the neutron beam.

3.1.3 Scintillator Calibration with Neutrons

To test the C_6H_6 and C_6D_6 scintillator response to monoenergetic neutrons, two experiments were done using the DD and DT neutron generators at the University of Michigan Neutron Science Laboratory [Hartman, 2008]. First, the light output of the scintillator was again calibrated with Compton edges from known γ sources such as ^{60}Co and ^{137}Cs. The production of monoenergetic neutrons by bombarding suitable targets with a deuterium beam was particularly attractive because the neutron energy produced is quite large. Traditionally, the D(d,n)^{3}He and ^{3}H(d,n)^{4}He reactions have been widely used as sources of monoenergetic neutrons. It was a logical first step to test our deuterated and hydrogen liquid scintillators. In the D+D and D+T reaction (yielding nearly monoenergetic ∼2.5 MeV and ∼14.1 MeV neutrons, respectively), the large positive Q-values and the low atomic numbers make it possible to produce high yields of fast neutrons even at low incident deuteron beam energies ($\leq$ few hundred keV).

The two nuclear reactions used to produce monoenergetic neutrons are:

$$D + D = {}^3He + n + 3.26MeV$$

and

$$D + T = {}^4He + n + 17.586MeV$$

The DD neutron generator used to test the scintillators was designed by Thermo Scientific with a maximum neutron yield of 10^8 neutrons per second. It is a small device which contains a compact linear accelerator and produces neutrons by fusing isotopes of hydrogen together [Thermo-Scientific]. The fusion reactions take place by accelerating deuterium into a metal hydride target which also contains deuterium. Fusion of deuterium atoms (D + D) results in the formation of a ^{3}He ion and a

neutron with a kinetic energy of approximately 2.5 MeV with a spread in energy $<$ 200 keV. It is important to note that the neutrons are isotropic.

Also, the horizontal axis in figures 3.7 and 3.8 is light output converted to the equivalent output (in MeVee) for electrons using the γ-ray calibrations.

For the case of the DT generator, the fusion of deuterium and a tritium nucleus (D + T) results in the formation of a ^{4}He ion and a neutron with a kinetic energy of approximately 14.1 MeV with roughly a 2 MeV energy spread in the beam. Again the neutrons are emitted nearly isotropically [Ludewigt, 2007]. The DT generator used for this test is a moderately large, fixed installation and consists of four main parts: the accelerator head, a control chassis, two cooling units, and the accelerating high-voltage power supply. The maximum neutron yield is $2x10^{10}$ neutrons per second. This unit is housed in a thick-wall shielded cave in the NSL because of the high radiation it produces. More information about the DD and DT generators is listed in Appendix B.

3.2 KMAX Data Acquisition

For the experiments done at UM, a KMAX CAMAC-based data acquisition systems was utilized [Sparrow, 2006]. A fellow graduate student (Hao Jiang) and I wrote this data acquisition program code in JAVA. The code was specifically written for the experiments with the neutron generators. A full description of the code and the entire code written can be found in Appendix D. Briefly, the data acquisition is a CAMAC-based system that reads the CAMAC crate using a standard crate controller via USB. The signals from the PMT are obtained from the ORTEC-265 base and sent to a LeCroy 428F analog fan out. The signal is then sent from the fan out into the constant-fraction-discriminator (CFD) where the gates are generated and

sent to the LeCroy 2249A-(charge-to-pulse-height-converter)QDC before KMAX receives the data. The electronics schematic describing this data acquisition process is shown in figure 3.5.

From the observed spectra (figures 3.6-3.8), one can deduce that for lower energy neutrons (E_n <2 MeV), one can clearly see significant differences between the C_6H_6 and C_6D_6 scintillators. In fact, this is even more pronounce for higher energy neutrons. The deuterated scintillator has a pronounced bump corresponding to the energy of the incident neutron. It is clear that all we have for the C_6H_6 however, is as expected a rather rounded-off step function (figures 3.7 and 3.9). As noted it makes it difficult to deduce the neutron energy for the latter unless one uses the ToF method.

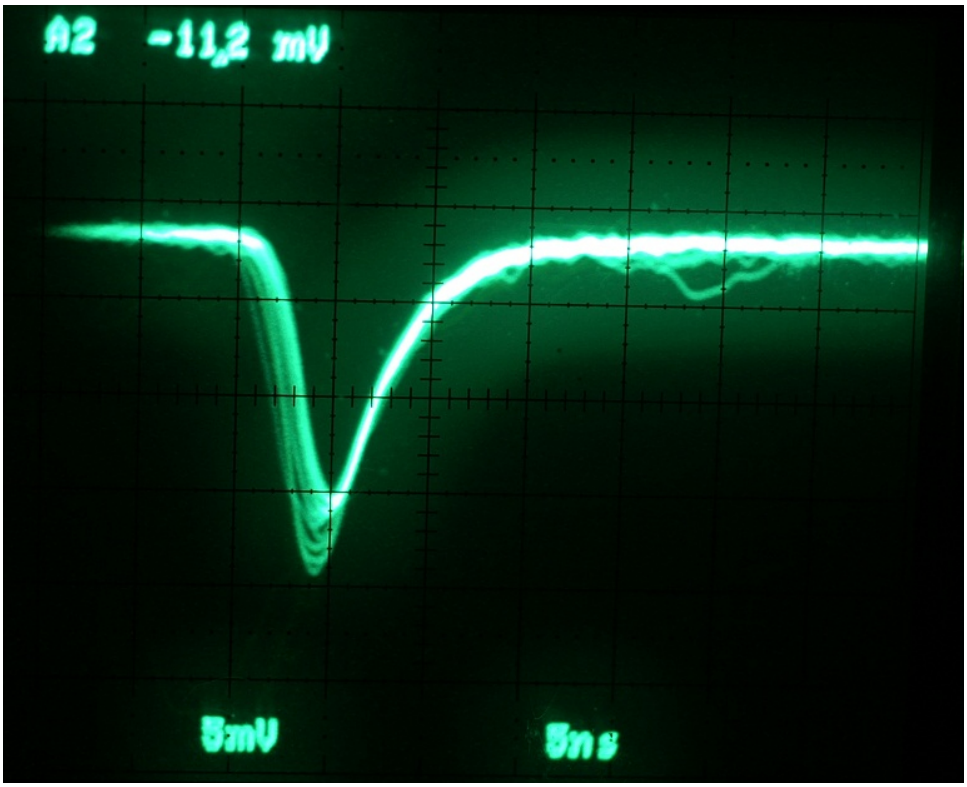

Figure 3.2: Typical PMT signal from the scintillator for γ-rays.

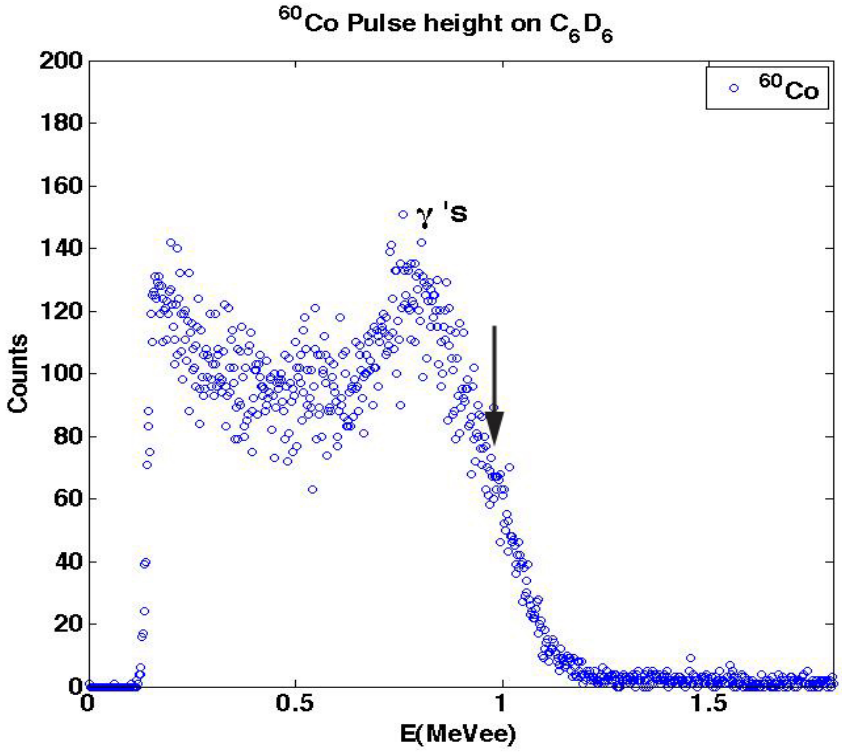

Figure 3.3: C_6D_6 response to ^{60}Co γ-rays. The arrow indicates the Compton edge calibration point (see text).

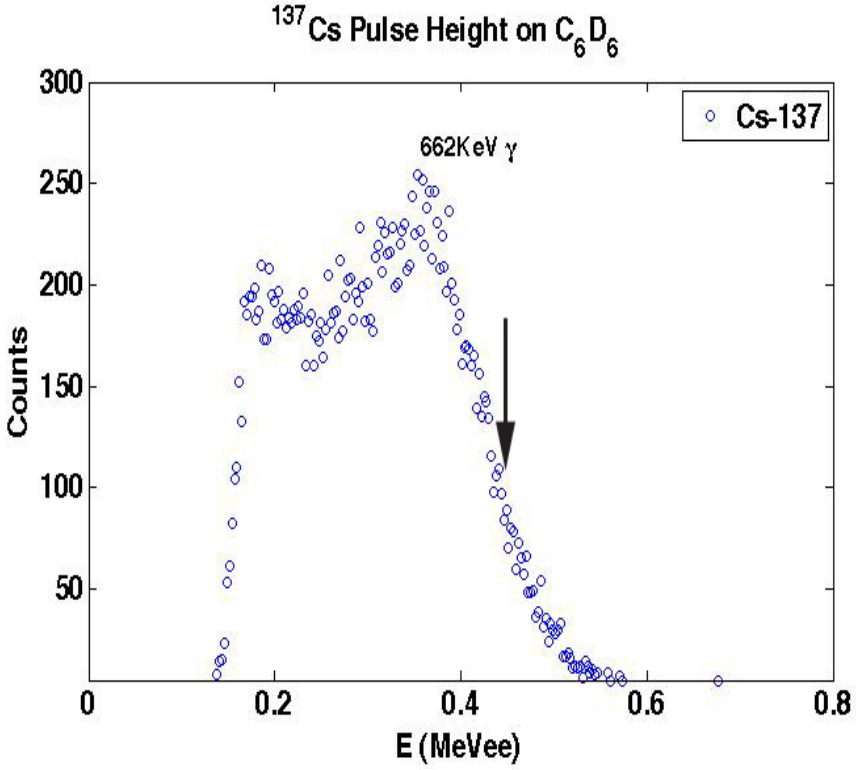

Figure 3.4: C_6D_6 response to ^{137}Cs γ rays (662 KeV). The arrow indicates the position used for the Compton edge, (see text).

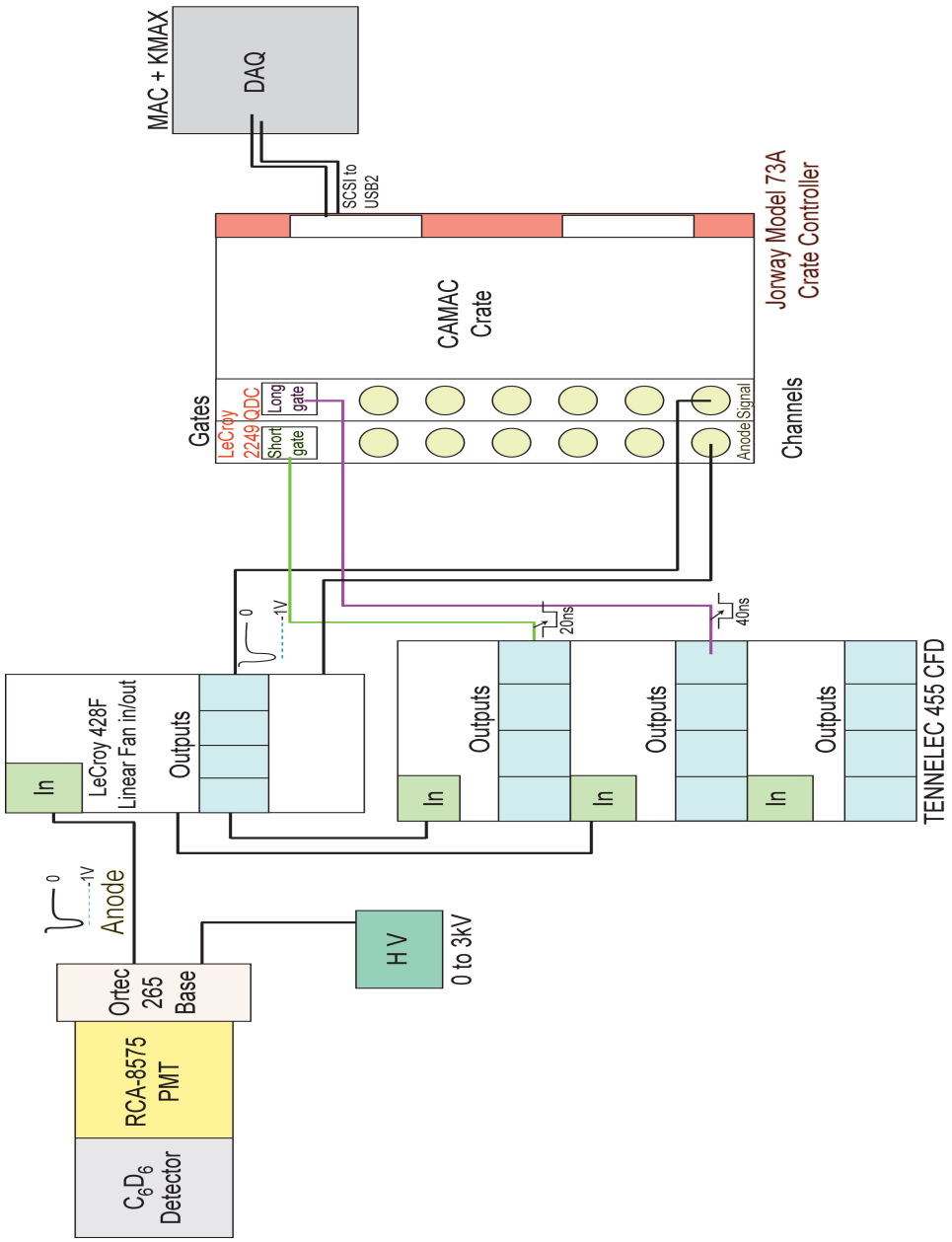

Figure 3.5: Electronics used for D+D and D+T studies at UM.

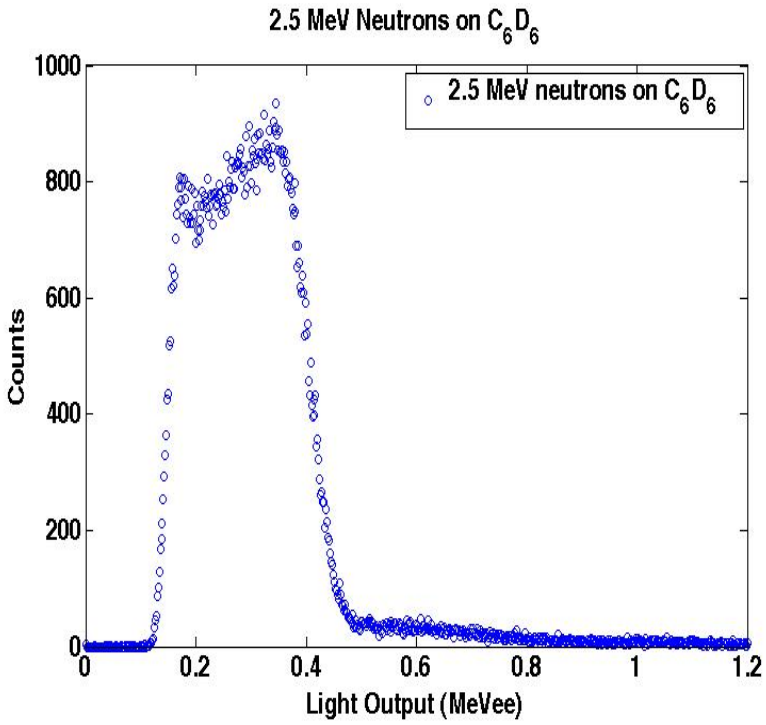

Figure 3.6: Observed C_6D_6 response to 2.5 MeV neutrons.

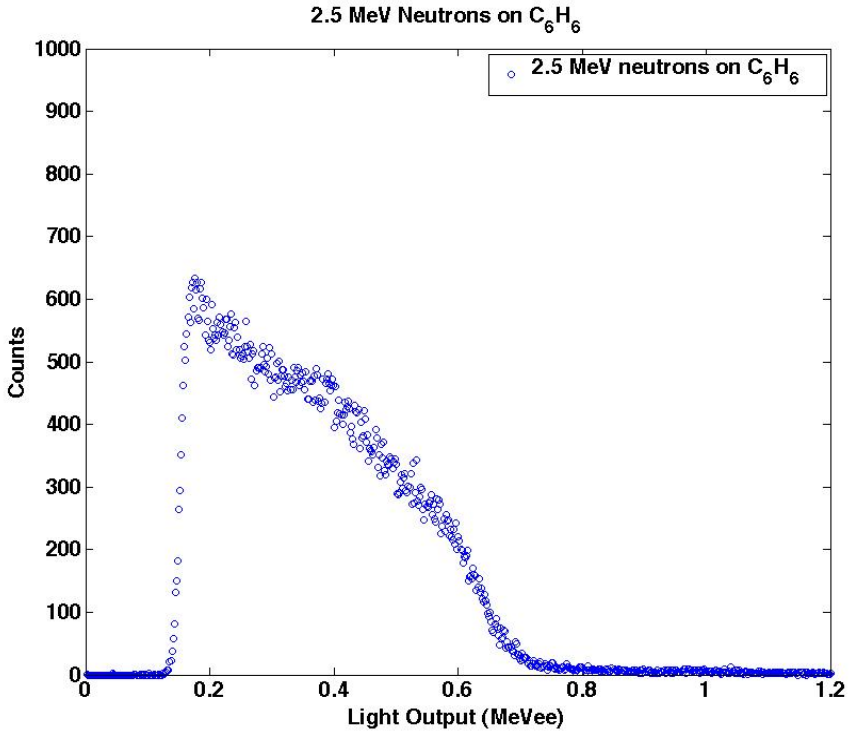

Figure 3.7: Observed C_6H_6 response to 2.5 MeV neutrons.

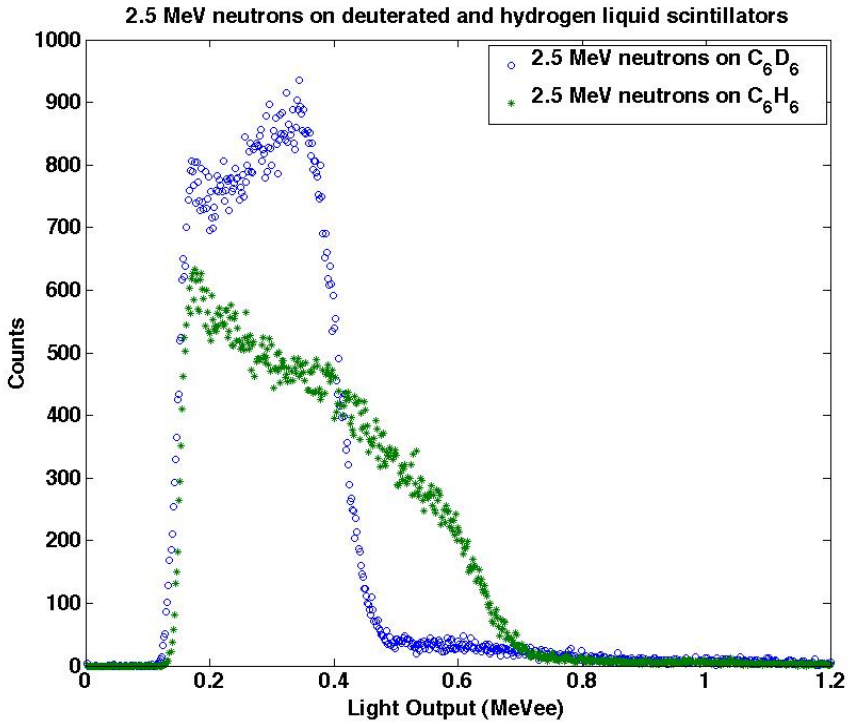

Figure 3.8: Observed C_6D_6 and C_6H_6 superimposed scintillator response to 2.5 MeV neutrons.

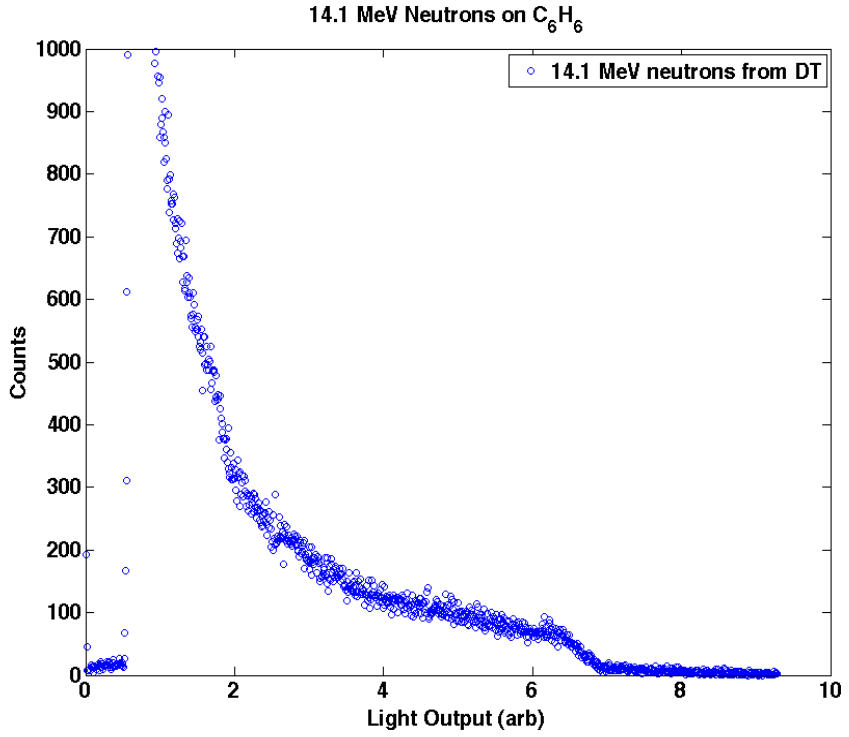

Figure 3.9: Observed C_6H_6 scintillator response to 14.1 MeV neutrons.

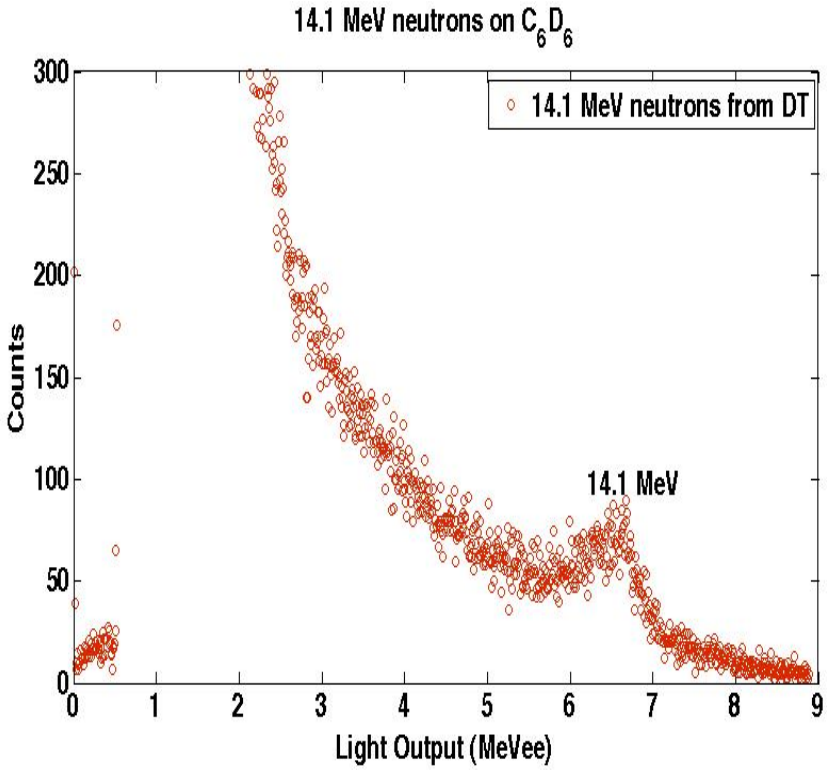

Figure 3.10: Observed C_6D_6 response to 14.1 MeV neutrons.

CHAPTER IV

The (d,n) Experiments at UND

4.1 D+D Experiment at E_d = 9 MeV

The purpose of this experiment was to measure the differential cross section for the known D + D nuclear reaction at 9 MeV and use it to verify the energy response and detection efficiency of the C_6D_6 scintillator for high-energy neutrons. For the D+D reaction where other reactions and nuclear species may be produced, a solid-state silicon detector telescope was used to observe the ^{3}He recoil particles from the D(d,n)^{3}He reaction in coincidence with neutrons if needed for future analysis.

Four identical (C_6D_6) deuterated liquid scintillators and a hydrogen (C_6H_6) liquid scintillator were used to observed the neutrons from the D+D reaction at E_d = 9 MeV (lab). The UND accelerator layout, the C_6D_6 detector array used for this experiment, the electronics, and the schematics for the array and the auxiliary ΔE vs. E telescope are shown in figures 4.1 to 4.3.

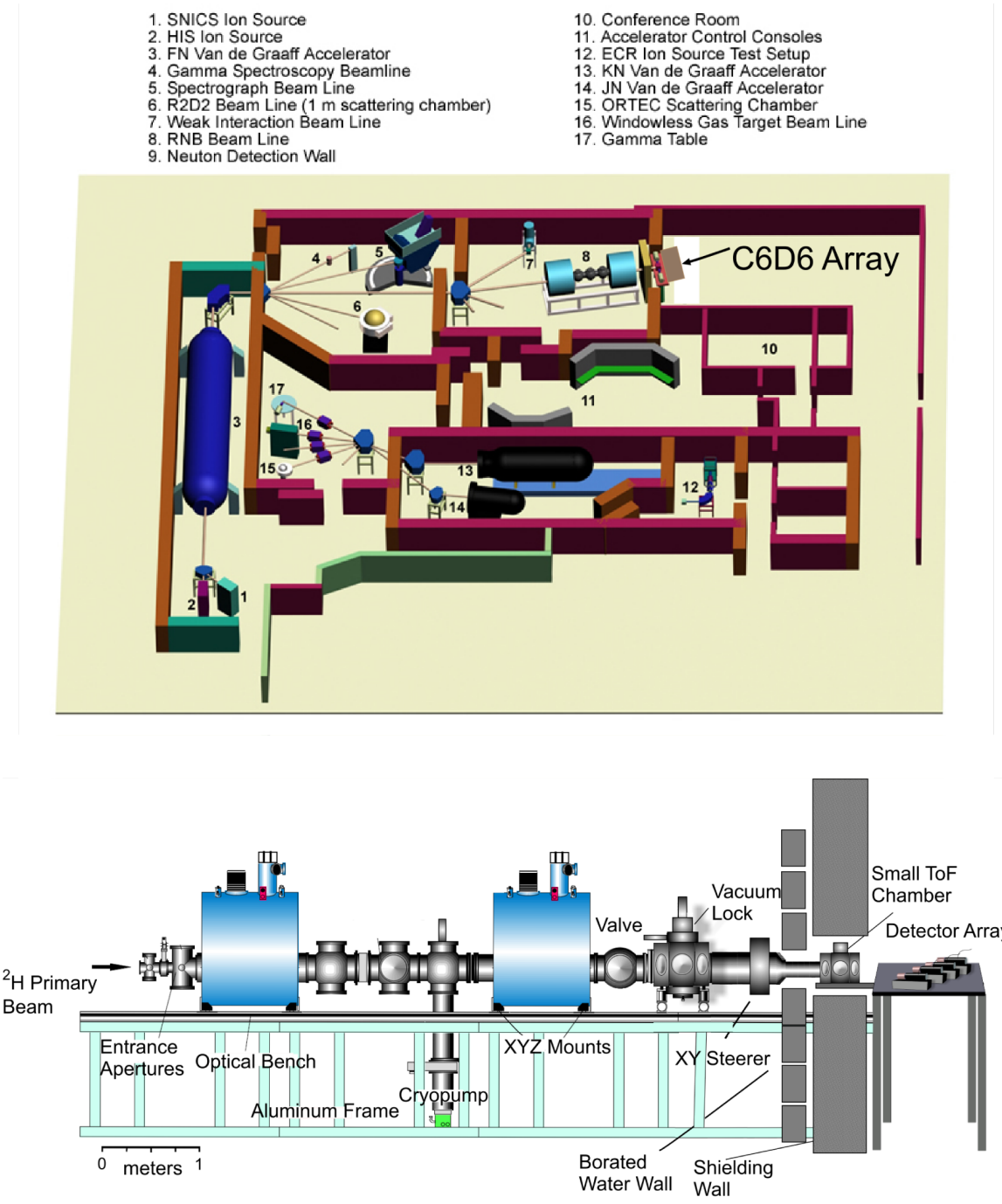

Figure 4.1: UND-*TwinSol* experimental layout.

array.png

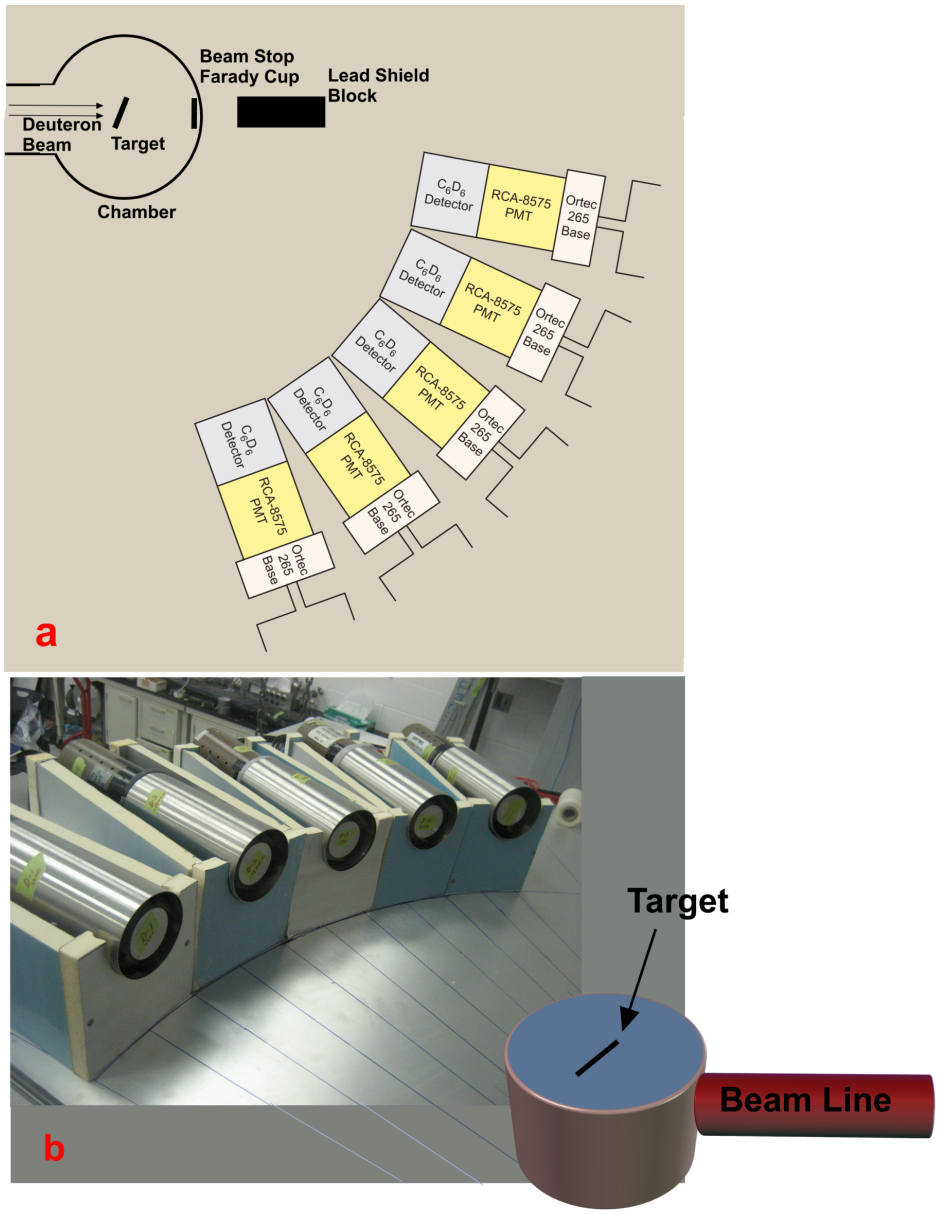

Figure 4.2: (A) Drawing of detector array used for the UND experiments. (B) Picture of the detector array.

The primary deuteron beam used for this experiment was accelerated by the 10 MV FN tandem Van de Graaff accelerator at the Nuclear Structure Laboratory at the University of Notre Dame [Nucl. Structure Lab Webpage]. The *TwinSol* radioactive nuclear beam facility [Becchetti, 2001] was used to focus the beam into a small thin-wall aluminum secondary target chamber located in a shielded room 7.5 m downstream from *TwinSol* [Becchetti, 2003][Lee, 2001]. Two large superconducting solenoids act as thick lenses to collect and focus the beam of interest onto a spot that is typically 5 mm full width at half maximum (FWHM). In this experiment *TwinSol* was used as a transport element and not used to generate a secondary beam.

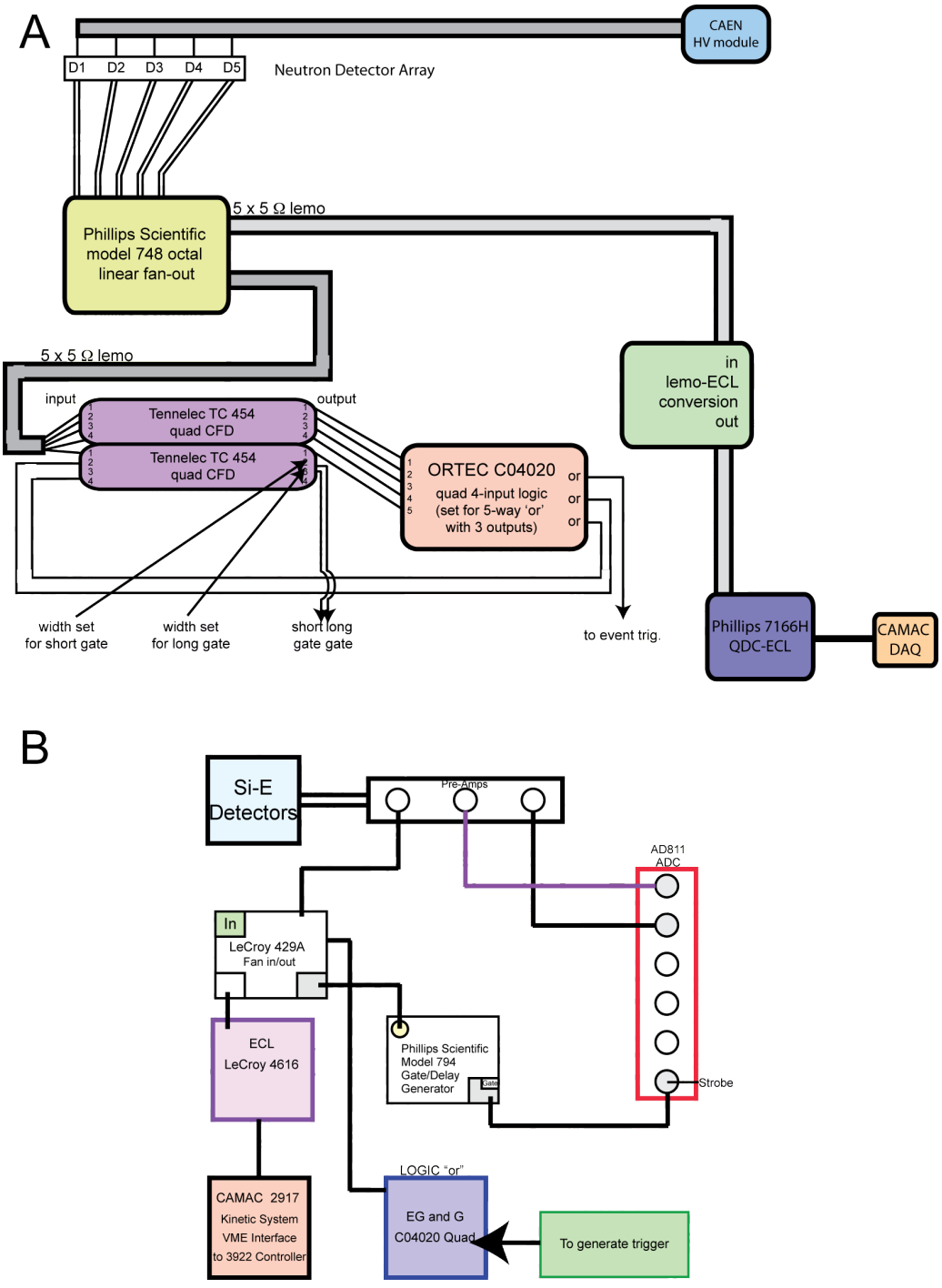

Figure 4.3: The electronic schematics for the UND experiments. (A) C_6D_6 electronics. (B) ΔE vs. E telescope electronics.

The 9 MeV deuteron beam was incident on a 257 μg/cm^2 CD_2 target. The target was in the small chamber together with the solid-state ΔE-E detector telescope which was not used for the data analysis presented here. The array of liquid scintillators were mounted on a platform covering a range of laboratory angles from 10 to 80 degrees in the lab (see figure 4.2). The current on the chamber faraday cup used to stop the beam typically was 0.1 to 1 nA. From kinematics we know that the neutron energy decreases rapidly with angle, and that this reaction has a large forward cross section. Thus deducing the cross section information for the forward angles was fairly straight forward since the spectra were very easy to work with, but for the larger angles, there were some problems. In fact the neutron energy from D(d,n) is reduced by almost 50 percent and overlaps neutrons from ^{12}C(d,n) from carbon in the CD_2 target. Data for a natural carbon target were therefore measured to identify background from carbon.

Cranberg [Cranberg, 1956], Thornton [Thornton, 1969] and Kolata [Kolata, 2008], have measured the cross section for this reaction within the same energy range. Thornton and Cramberg measured a wider deuterium beam energy range compared with the one used for this thesis and that of Kolata. It appears the cross sections do not vary much as the bombarding energy increases. The D(d,n) spectra shown in figure 4.4A, displays the ^{13}N g.s. and ^{3}He g.s. The lab cross section was determined using equation 4.1:

$$d\sigma/d\Omega = (N_{event}/\epsilon)/(Q * d\Omega * N_{tgt}) \tag{4.1}$$

where $N_{tgt} = (N_A * R\rho x)/A_{tgt}$

$d\Omega$ = solid angle = area of detector x F $\div$ r^2

F = detector liquid fill fraction (= 90%)

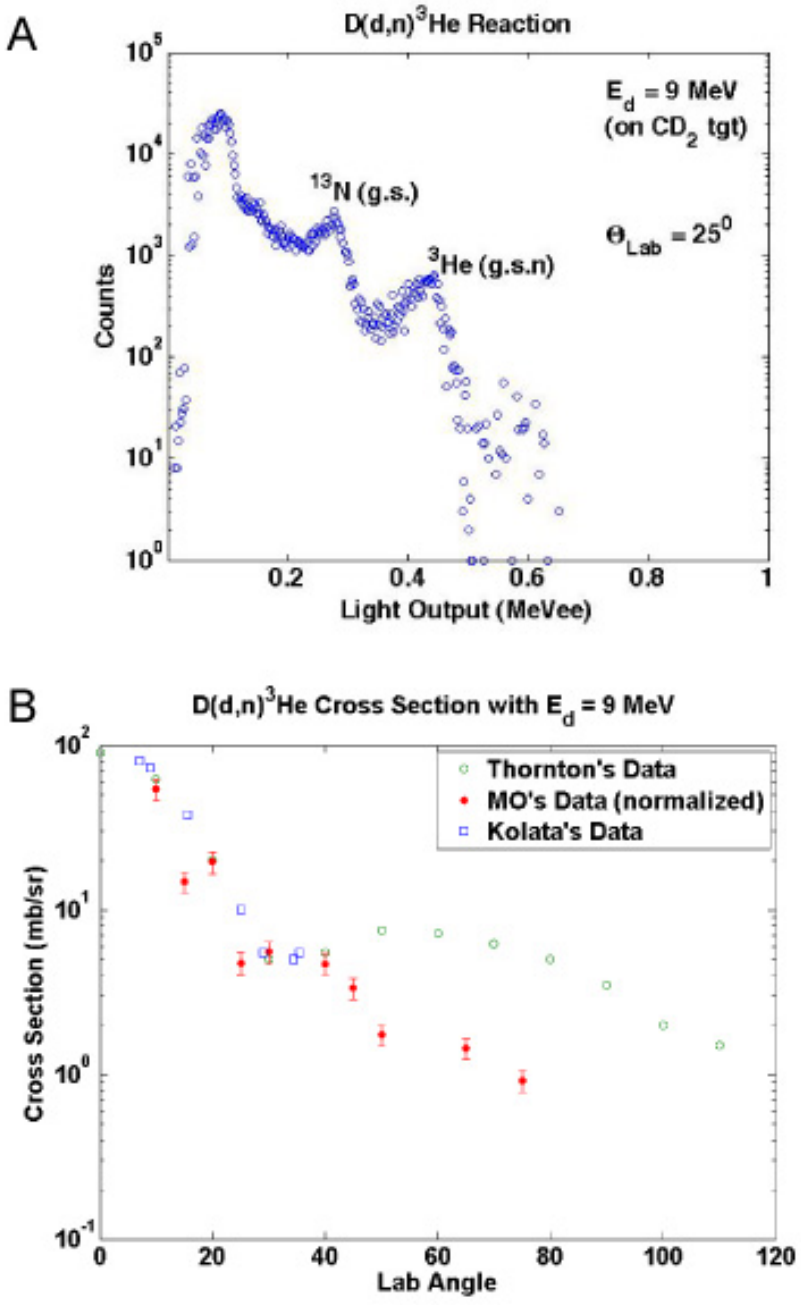

Figure 4.4: (A) D(d,n) reaction spectrum. (B) D+D cross sections $E_d = 9$ MeV from MO's experiment, Thornton's data [Thornton, 1969], and Kolata's data [Kolata, 2008].

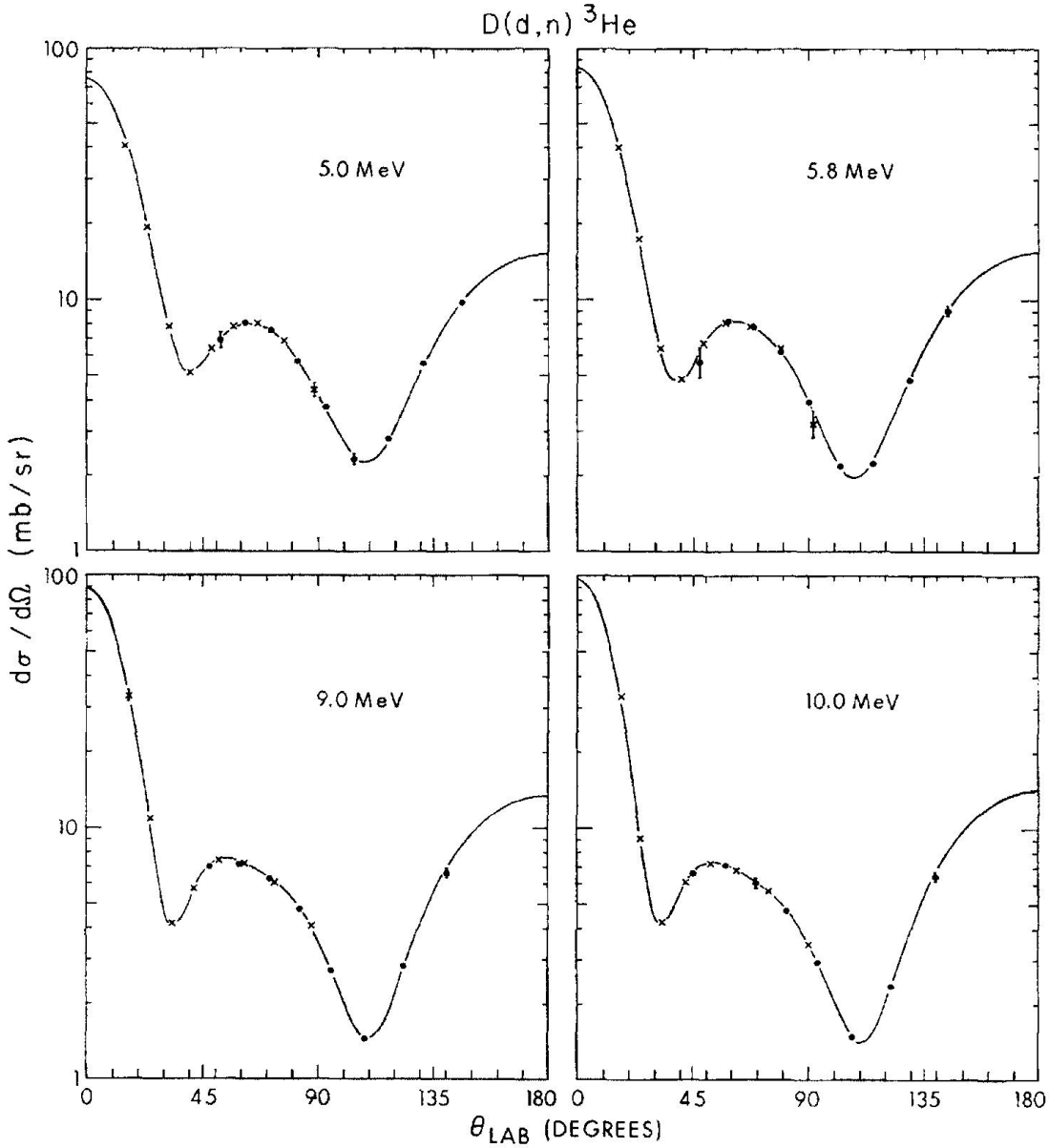

Figure 4.5: Known laboratory D(d,n)^{3}He differential cross sections, E = 5 - 10 MeV [Thornton, 1969].

N_{event} = number of scattered events recorded

ϵ = detector efficiency

N_A = Avogadro's number

ρx = target thickness $\div$ cos(Θ)

cos(Θ) = target angle

Q = Beam charge collected (Coulombs)

The ratio R = A/A_{tgt} in N_{tgt} corresponds to different values based on the target composition. For the CD_2 target, R = 4/16 for deuterons in CD_2 and 12/16 for carbon in CD_2.

In principle the detection efficiency, ϵ can be calculated from a simulation (Appendix C). However, in this case we have a known cross section we can use for a normalization ϵ, and then use that value for the measurements on other targets. In figure 4.4B we show the cross section measured and normalized at forward angles plotted against that measured by Kolata [Kolata, 2008]. As the angle increases, differences in the cross sections compared to the known cross sections are apparent. This is perhaps due to the optical coupling problem we experienced during the latter stages of the run. (Shown in figure 4.5 are the additional D+D cross sections vs. E_d according to Thornton [Thornton, 1969])

It is important to make sure that the detector is well coupled to the PMT. For the initial PMT coupling to the scintillators, we used the Eljen Technologies silicon grease. Although we had five detectors as shown in figure 4.2, and the scintillators initially functioned satisfactorily, it became evident later during the UND experiments that the scintillator and some of the PMTs probably had lost their coupling. This prevented us from obtaining some reliable data for a variety of angles. This limited the amount of good data we could achieve. A better optical silicon grease

such as the St. Gobain BC-630 is needed to ensure good optical coupling.

The efficiency deduced from the normalization of the measured D+D data to that of Thornton and Kolata yields an efficiency higher than expected from the simulation (sect. 5.2 and appendix C). This will require further study.

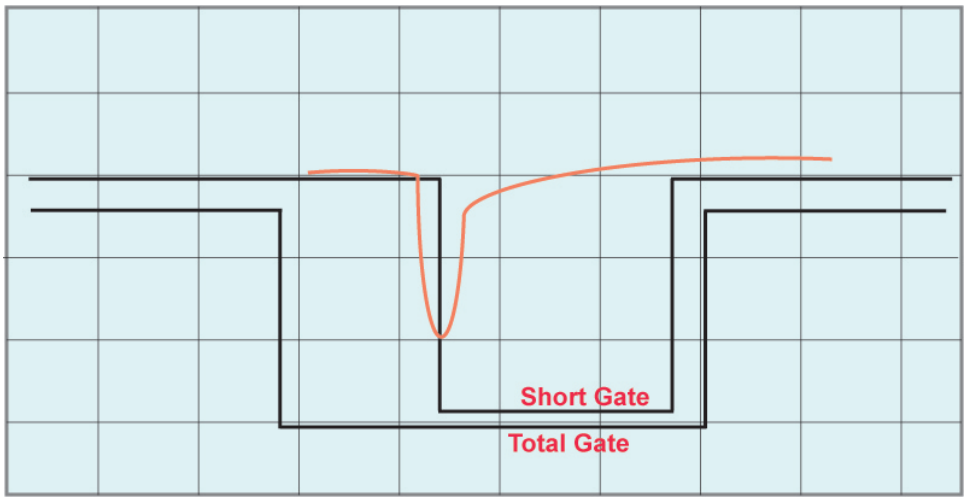

Figure 4.6: QDC timing for pulse shape discrimination (time = 10 ns/div).

4.1.1 Pulse Shape Discrimination (PSD)

This experiment was intended to test the detectors' response, verify the detector efficiency and test the n/γ pulse shape discrimination (PSD) capability. The information about the nuclear process only can be deduced from the neutron spectrum projected from the 2D PSD spectra. Since γ-rays emit light faster than a recoil proton or deuteron one can integrate the light emitted over different time scales (short time gate and long time gate) to generate a PSD spectrum. Care was taken to make sure the constant fraction discriminator gates used to set the pulse integration time windows were set properly (figure 4.2). One had to adjust these gates until a reliable gate was obtained for the PSD. For this experiment, the short time gate set at the trailing edge of the PMT pulse was 20 ns while the long gate covering the entire PMT pulse was set at 40 ns (figure 4.6).

Figure 4.6 shows the signal timing scheme used for the pulse shape discrimination. The QDC integrates the charge of a signal only when a timing gate is present. As noted, one gate is set so that the QDC integrates the total charge of the pulse, while the other is set to integrate just a portion of the tail. Because the pulses for γ rays and neutrons have different decay time (equation 4.2), the ratio of the integrated tail charge to the total charge provides one of the best means for PSD.

A major obstacle with recoil detectors is the presence of signals as a result of random gamma ray events that are generated by the incident beam. In general, the range of gamma ray pulse heights will usually overlap that of the neutron events, and therefore a means of uniquely identifying and separating neutron events is required [Marrone, 2002][Brooks, 1979][McBeth, 1971]. Organic liquid scintillators such as C_6D_6 exhibit different responses to different types of incident particles. More importantly, as noted the time structure of the light-pulse signal emitted are dependent upon the ionization of the particle in the scintillating medium [Smith, 1968].

The recoiling particle from neutron scattering produce signals with slow decay times as compared with signals of recoiling energetic electrons from γ-rays. The pulses produced by Compton electrons from gamma events are found to contain most of their total emitted light in the leading edge, with relatively little light in the tail pulse. On the other hand, proton or deuterons recoils due to neutrons or heavier particles are found to have a larger fraction of the total light in the tail, and less in the leading edge. For this reason, integration of the falling edge of the resulting signal gives a good way to discriminate neutrons from gamma rays. This is mathematically described by an exponential equation:

$$A(t) = A_1 e^{-t/T_1} + A_2 e^{-t/T_2} \tag{4.2}$$

where ($T_1 > T_2$)

The ratio between A_1/A_2 is highly dependent on the particle type.

There are many ways to achieve PSD. However, for this experiment, pulse shape discrimination was achieved by integrating the charge of the signal tail and comparing it with the total charge. Figure 4.7 shows a typical PSD spectrum. The spectrum only contains information about the particle separation in the 2D spectrum. In order to deduce the neutron energy information, the neutron band is then gated in the 2D spectrum and projected onto a 1D spectrum for further analysis.

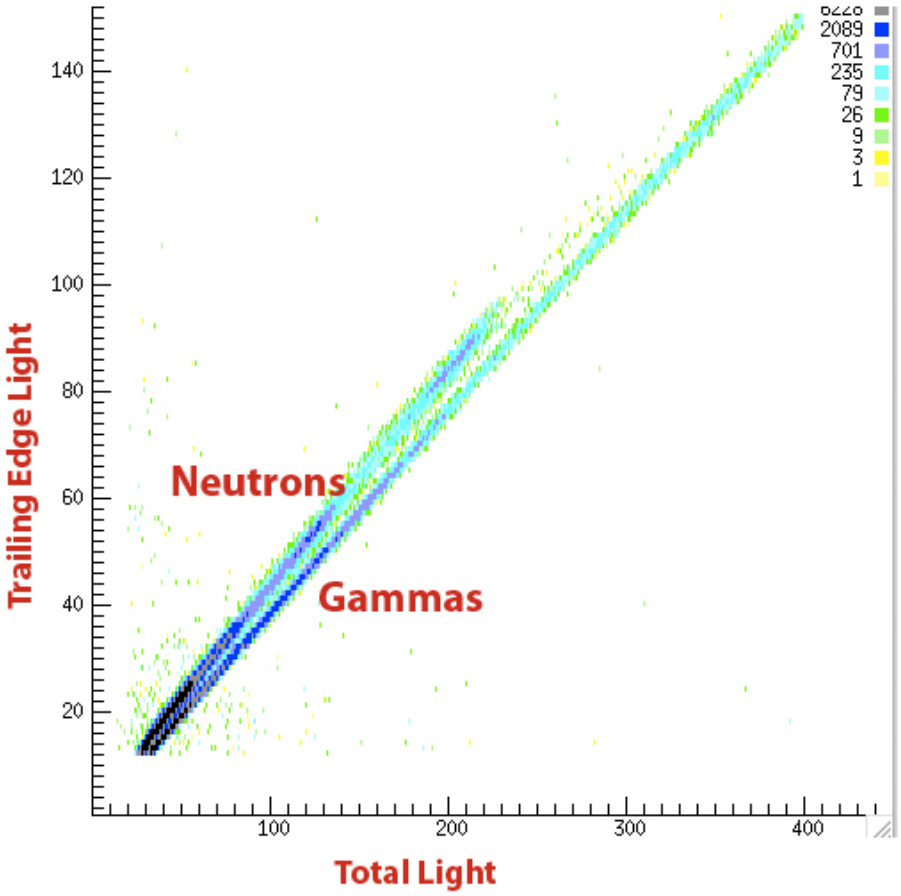

Figure 4.7: 2D spectrum of the C_6D_6 pulse shape discrimination (PSD).

From figure 4.3, we can see that the PMT output was fanned out using the LeCroy

428F linear fan-in/out. Two of the negative signals from the 428F were then sent into the Tennelec 455 CFD to trigger timing gates. A third output from the 428F was sent to a delay box to allow the adjustment of the signal going into the QDC gate. The output of the delay box was then sent back into a second 428F where two negative signals were now are inputed to the LeCroy 2249A QDC. The gate output starts the QDC and sets the gates for integration of the light signal (PMT anode charge pulse).

4.1.2 Data Acquisition

Experimental data at UND were collected and analyzed with a Linux-based PC computer. In Part A. of the experiment, the liquid scintillator anode signals were input into a fan out where two negative signals were input into a QDC within the CAMAC crate shown in figure 4.3. The QDC integrated the total and partial charges of the negative signals using the 40 and 20 ns time gates noted. The CAMAC modules then processed the signals received and sent these to the computer. Data collection, analysis, and storage were achieved with the help of the Oak Ridge Data Analysis Program (ORDAP) [Milner, 1980]. From the computer terminal, the CAMAC crate could be initialized and data collection could be started and stopped. One-dimensional and two-dimensional histograms from the QDC inputs were created with a sub program within the ORNL package called DAMM. The two-dimensional histograms contained the integration of both the short and long time gate information from the QDCs and generated the PSD spectrum (figure 4.6). The neutron band in the aforementioned spectra is gated and projected to reveal the neutron energy information contained in the spectra. A copy of the ORDAP data acquisition code written for this experiment is given in Appendix D.

4.2 ^{12}C(d,n)^{13}N Experiment

The schematic for this experiment is the same as the one used for the D(d,n)^{3}He experiment. The main difference is the target, which then provides data to remove neutrons emitted from the ^{12}C in the CD_2 target. We used a 941 μg/cm^2 thick ^{12}C target. In recent years the ^{12}C(d,n)^{13}N reaction itself has been of considerable interest for several reasons. The effects of interference between a direct proton-transfer reaction and compound-nucleus formation with neutron emission is of interest. The ^{12}C(d,n)^{13}N reaction also is a source of enormous amounts of neutrons at E_d = 9 MeV and is useful for other applications as carbon targets are inexpensive and can take high beam currents. Here we use this reaction as another standard neutron calibration for the detectors. Because the target used for the D+D experiment has a carbon component, as noted, it also was important to do this experiment to remove ^{12}C(d,n) neutrons to deduce information from the neutron spectra for D(d,n) on CD_2.

Before any neutron data was collected, the detectors were once again calibrated in MeVee using a ^{60}Co button γ source (table 3.1). The Compton edge again was used as the energy calibration point for the detectors (e.g. E_γ = 1.17 MeV = 1 MeVee Compton edge). The gains on the PMT were gain matched before data was collected by adjusting the PMT gain with the HV supply. After this neutrons were allowed to impinge on the scintillator and reaction spectra were obtained with the beam intensity adjusted to avoid appreciable pulse pile up in the detectors.

This reaction made it possible to explore another unique feature of the scintillator. With this reaction, there are several excited states of ^{13}N that could be observed. Using a typical hydrogen-based scintillator would require multiple extraction of in-

formation employing the ToF method. With the deuterium-based scintillator we are able to observe the various energy states and work with them directly from the spectra. Figure 4.8 shows a spectra taken at a specified angle showing the various nuclear energy states. In the spectra we observe the ground and the 2.31 MeV first excited state, together with the two very states close in energy at 3.51 MeV and 3.56 MeV excitation in ^{13}N.

4.3 ^{13}C(d,n)^{14}N Experiment

This experiment was done to eventually deduce some nuclear astrophysics parameters such as spectroscopic factors. The setup for this experiment was the same as the aforementioned D(d,n) and ^{12}C(d,n) experiments. The difference is the enriched (to more than 90% ^{13}C) target that was used. The target for this experiment was manufactured by the Arizona Carbon Foil Co., Inc. with a stated thickness of 400 μg/cm^2

Bobbitt [Bobbitt, 1973] carried out a similar experiment but only to observe the excited-state energy levels. Cross section data and deduced spectroscopic factor for the same experiment at $E_d = 5.5$ MeV also have been reported [Cookson, 1968][Fuchs, 1966]. As part of this thesis, the cross section for the 13C(d,n) reaction was measured at various laboratory angles. To our knowledge this was the first time such cross section data above 6 MeV is reported. At energies above 6 MeV it is expected that the data become easier to analyze. One would minimize the compound states that contribute to the cross sections for energies less than 6 MeV. Again, to obtain the neutron spectra showing the individual states, the neutron band of a 2D PSD spectrum containing only neutron events was gated and projected unto a 1D deuteron recoil spectrum to reveal the neutron energy information. From figure 4.9, distinct

peaks of forward recoiling deuterons corresponding to the ground state and the first few excited states of ^{14}N are clearly seen. We see this well because of the large separation of states in the residual nucleus.

Figure 4.10 shows the ^{14}N (g.s.) cross section measured in this experiment using the detector efficiencies obtained from the D+D measurements.

A major advantage with C_6D_6 liquid scintillator is the fact that energy information and peak values could be obtained directly without ToF. So in obtaining the cross section, the scintillator deuterium recoil peak in the spectra is gated and projected. The peak sum is then obtained from the 1D spectra and used in the cross section calculation with the peak efficiency deduced from the D+D measurements.

In figure 4.11 we display the various excited states that were obtained with a long flight path (tens of meters). The one obtained with the C_6D_6 liquid scintillator array was obtained with less than 1 meter from the target yet will permit measurement of angular distributions for several states in ^{14}N.

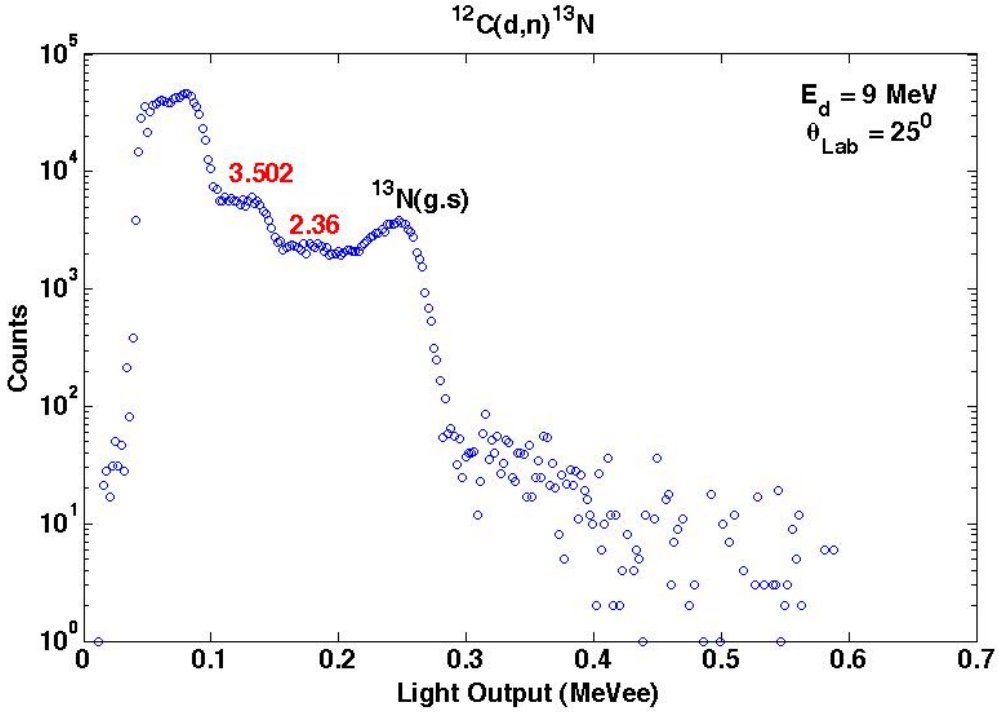

Figure 4.8: D+^{12}C reaction spectra showing various ^{13}N excited states. The x-axis is light output converted to electron-equivalent energy in MeVee.

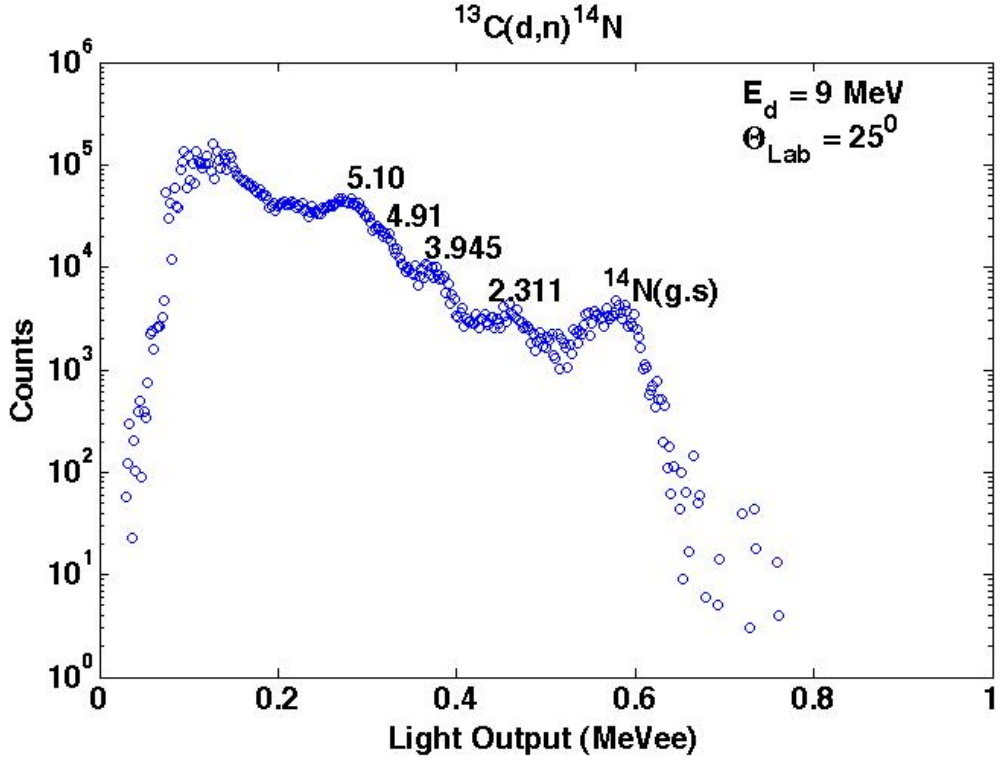

Figure 4.9: D+^{13}C reaction spectra showing the various ^{14}N excited states. The x-axis is light output converted to electron-equivalent energy in MeVee.

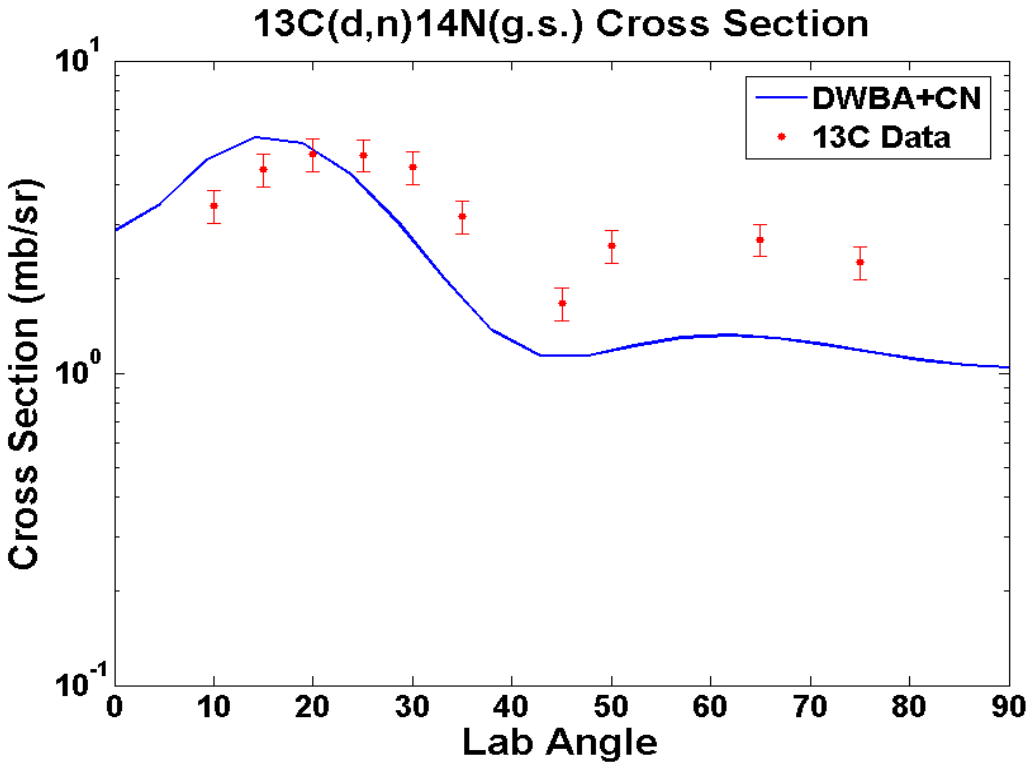

Figure 4.10: ^{13}C(d,n)^{14}N(g.s.) cross section $E_d = 9$ MeV. The curve is a DWBA calculation [Krane, 1988] including a compound nucleus (CN) contribution based on the calculation shown in [Bobbitt, 1973].

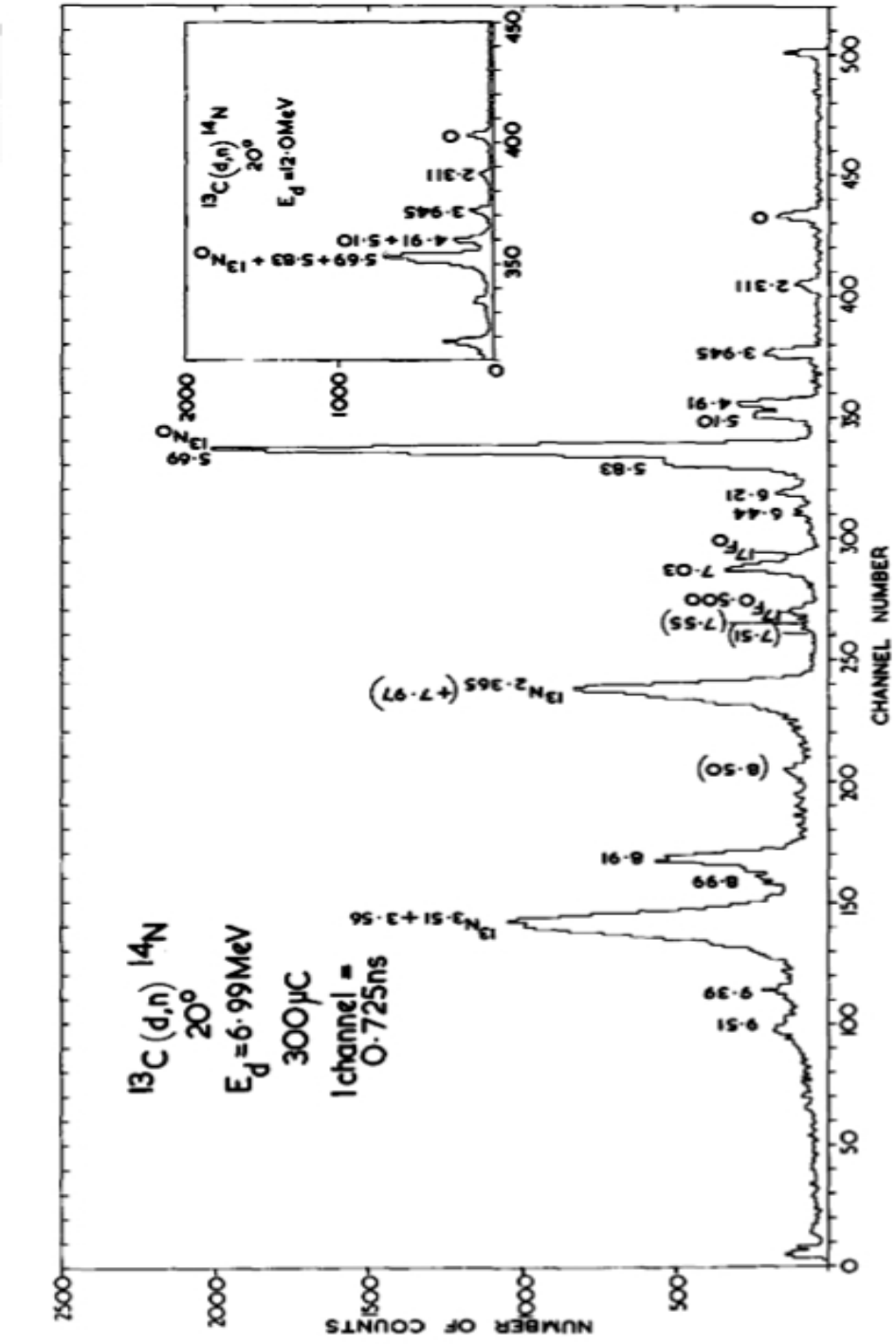

Figure 4.11: Time-of-flight spectrum at 20^o for the ^{13}C(d,n)^{14}N reaction [Cookson, 1968].

CHAPTER V

Monte Carlo Simulations

5.1 Introduction

As part of this thesis, a Monte Carlo simulation was performed to produce the detection efficiency of both the C_6D_6 and the C_6H_6 detectors. The detector efficiency simulation was performed with the MCNP-Polimi code and the Polimi MatLab Post Processor code [Pozzi, 2004] modified for deuterated scintillators. The modification involved including a n + d cross section library thereby adding the n+d differential cross $d\sigma/d\Omega\Theta$ and total cross section σ(E) data (for both the elastic and inelastic scattering collisions), light output data for deuterons, adding the n +d scattering to the reaction selection routine, and modifying subroutines that calculate the light output for each n + d scattering events that significantly contribute to the final light output, L.

As the need for better ways of detecting neutrons and other nuclear particles increases, so does the need for new tools to carry simulations. In recent years, the use of special liquid scintillators such as C_6D_6, such as used in this thesis, have become more widespread. However, there is limited published materials on these new detectors, hence this thesis project. This is not the case for C_6H_6 (e.g. NE213) liquid scintillators and the popular NE102 plastic scintillators, where there exist extensive

information. Because MCNP-Polimi was initially written for both plastic and liquid scintillators, it already contains the conversion factors and fitting parameters for typical normal hydrogen liquid scintillators. A primary task was now to modify the code to include deuterium-related parameters including the light output conversion factors.

I will again briefly review the process behind how neutron scintillator works and the simulation needed. When a neutron hits the detector, it collides with the atomic nuclei that make up the detector (scintillating materials). The atomic nuclei for C_6D_6 are deuterium (deuterons), hydrogen (protons), and carbon. When a neutron collides with a nucleus, the neutron transfers energy to the nucleus. The energy that is transfered obeys conservation of energy and momentum. The recoiling nucleus will then collide with electrons of other atoms and molecules before it comes to rest. The recoiling nucleus will loose small amounts of energy during each of many collisions. About 10% of the collisions will excite the scintillator materials and when they de-excite, they will emit photons (figure 2.1). The emitted photons have nearly the same total amount of energy as that transfered to the atom during the initial collisions. These photons make up the light output from the scintillator which the PMT detects and amplifies.

A PMT anode pulse-height distribution based on the light output is generated. In this spectrum the light pulse amplitude calibrated in electron energy units (MeVee) is plotted on the x-axis and the number of events detected (neutrons) on the y-axis. The integration of this curve relative to the number of incident particles gives the total detection efficiency. Thus in our case, the total detection efficiency is the ratio between the detected neutrons and the number of neutrons incident on the scintillator. However, it will depend on the lower-level PMT anode signal threshold

used.

Having a realistic simulation code to generate the detector efficiency is an excellent time-saving technique that allows the reliable use of scintillator detectors for cross section measurements. It can be tested using known experimental cross sections such as D(d,n). My modification of the MCNP-Polimi is shown in its entirety in Appendix C and contains the modifications to the code needed to simulate neutron detection in C_6D_6 in the neutron energy range of 2-20 MeV.

5.2 Efficiency Simulation for Neutrons with the MCNP Post Processor

To simulate a scintillator detector pulse, requires that the energy deposited by neutrons and photons or charged particles in the detector be converted into light output using measured detector light output response functions (e. g. figures 2.3-2.5). Since photons in organic scintillators are detected primarily by Compton scattering, the pulse height to energy deposited response function is nearly linear:

$$L \doteq E_\gamma \tag{5.1}$$

where E_γ is the energy deposited by the photon (MeV) and L is the measured light output (in MeVee). Neutrons on the other hand are detected for the most part by elastic scattering on nuclei, and the response is nonlinear. Pozzi et.al. have measured the neutron and photon pulse-height to energy response functions for organic liquid scintillator (BC 501 equivalent to C_6H_6) and plastic (BC 420) scintillators [Pozzi, 2004]. The measured response functions can be fit with quadratic functions as follows:

$$L_H = 0.0364 * E_n^2 + 0.125 E_n \tag{5.2}$$

for the plastic scintillator, and

$$L_H = 0.0350 * E_n^2 + 0.1410 E_n \tag{5.3}$$

for the organic liquid scintillator, where E_n is the energy deposited by the neutron on hydrogen (MeV) and L_H is the resulting light output (MeVee).

The above equations can be used to obtain the light output data for C_6H_6 scintillators while the equation below can be used for C_6D_6. It is worth noting that the light output from the C_6D_6 scintillator is a bit less than traditional (C_6H_6) scintillators. The fitting parameters for C_6D_6 were obtain from published data [Naqvi, 1994][Smith, 1968]. The light output equation for C_6D_6 is then as follows:

$$L_D = 0.02963 * E_n^2 + 0.1350 E_n \tag{5.4}$$

where E_n is the energy deposited by the neutron on deuterium (MeV) and L_D is the measured light output in electron-equivalent energy units (MeVee). It is important to note that neutron interactions with carbon atoms also produce some amount of light, which we can approximate as

$$L_D = 0.02 * E_n \tag{5.5}$$

where E_n is the energy deposited by the neutron on carbon (MeV) and L_D is the light output (MeVee).

In figure 5.1 I display the total efficiency for detecting neutrons of a certain energy as a function of the PMT anode thresholds (in MeVee) set in the electronics (e.g. at the CFD shown in figures 3.5 and 4.3).The bump in the lower energy end, close to 9 MeV is due to the resonant states in the 12C(d,n) reaction. This is obvious in

the figure because the scintillator contains 12C as part of the scintillating material. In figure 5.2A I display the calculated C_6D_6 total detection efficiency. Figure 5.2B shows the calculated total neutron peak efficiency needed to extract cross sections. It is analyzed in the simulation in the manner used to analyze actual spectra (which includes a background subtraction as needed). However, as noted in section 4, the detector neutron peak efficiency deduced from the D+D measurements differs from the simulated values (which appear to be low). This will require further study.

In figure 5.3, I display a simulation of 14.1 MeV neutrons on C_6D_6 compared with the measurements. The latter, however, include scintillator resolution and pulse-pile up degradation not included in the simulations. (More detailed measurements are planned).

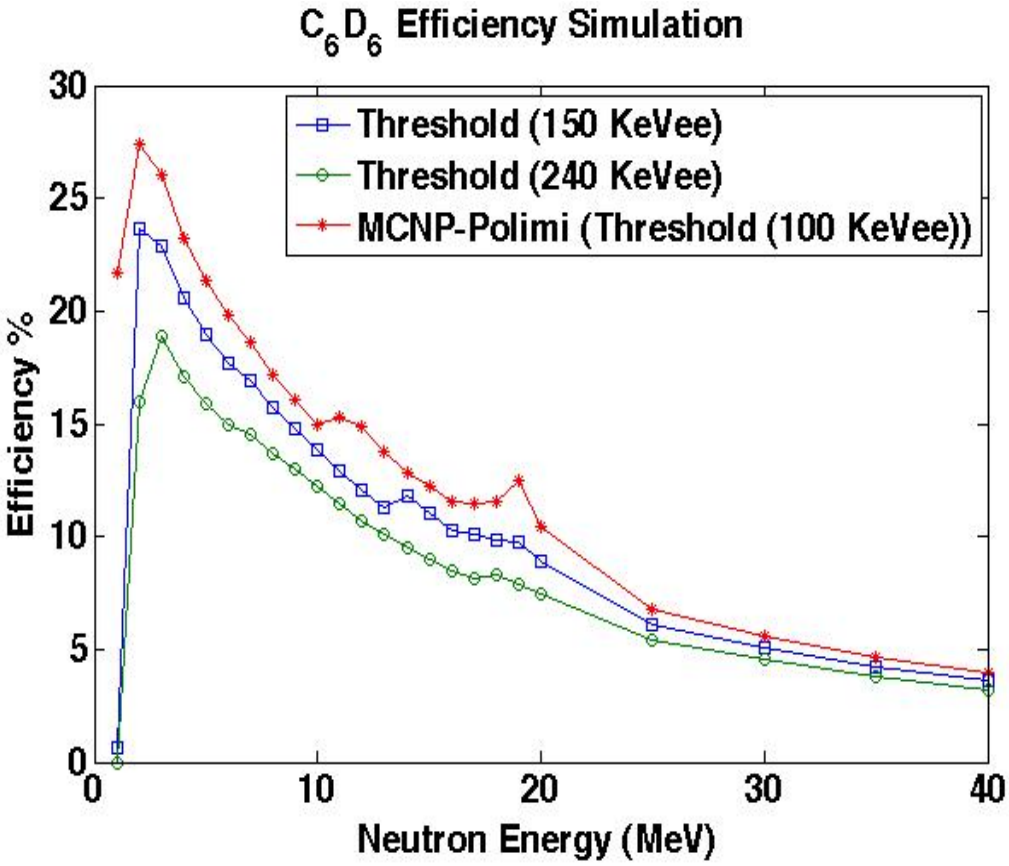

Figure 5.1: C_6D_6 total efficiency simulation.

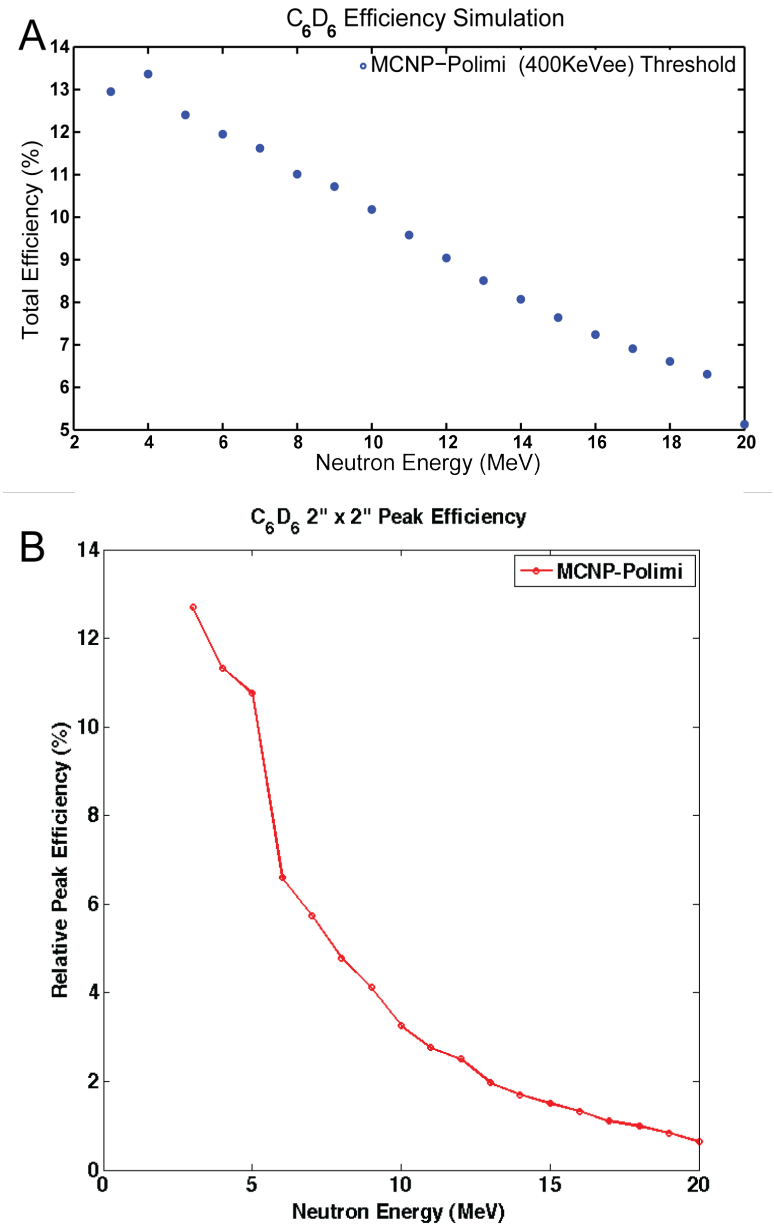

Figure 5.2: Simulated total neutron efficiency (A) and simulated neutron peak efficiency for C_6D_6 (B).

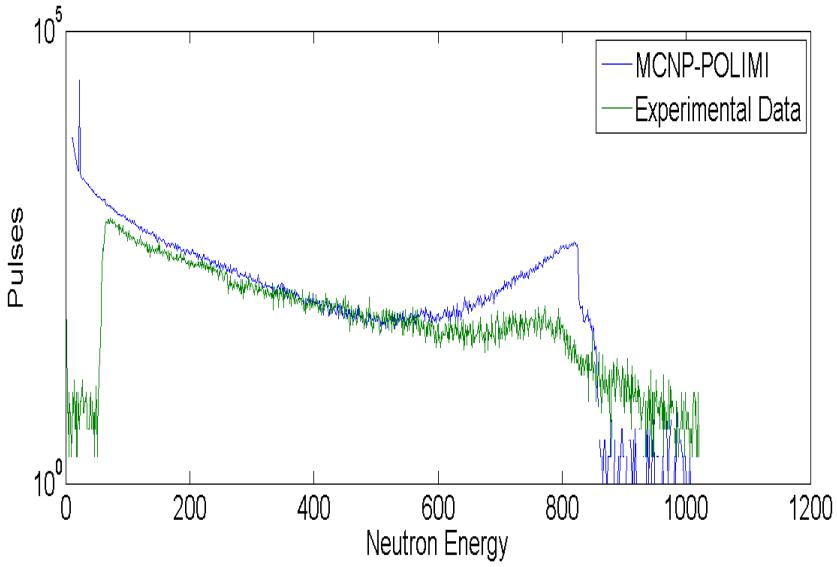

Figure 5.3: Measured and simulated (detector resolution and pulse pile up not included) 14.1 MeV neutrons on C_6D_6.

The input file written for MCNP-Polimi is given below:

```
Neutron Detection With Liquid Scintillators
c VOLUMETRIC GEOMETRY DEFINITION "CELL CARDS"
c CELL_NUM  MAT_NO  DENSITY(g/cc) SURFACE_CONSTRAINTS
1  1  -0.954   -1   imp:n=1   $ Detector
2 13  -2.7  1 -2   imp:n=1   $ Aluminum Shell
3 0  2 -999  imp:n=1   $ Vacuum
999  0  999    imp:n=0   $ The outside world
c SURFACE DEFINITIONS "SURFACE CARDS"
c define the surfaces that form volumes
c   ORIGIN    AXIS_VECTOR    RADIUS
1 RCC   0 0 0   5.08 0 0   2.54    $ Detector
2 RCC -0.05 0 0   5.13 0 0   2.59    $ Al. on det
c  xmin xmax  ymin ymax  zmin zmax
999 RPP -10   10   -10   10   -10   10
 $ Box over region of interest
c EVERYTHING ELSE "DATA CARDS"
c Define the source of neutrons
SDEF POS=-0.06 0 0 AXS 1 0 0 RAD=d1
PAR=1 ERG=15 VEC= 1 0 0 DIR=1
SI1 0 2.54
SP1 -21 1
c Define the problem type/mode
mode n
c The PHYS and CUT cards are essential for analog MC
PHYS:N J 20    $Mo
CUT:N 30  $mo
c Limit how long we run this problem
c ctme 0.1  $ Max run time in minutes  $MO
c Limit how many particles get created
NPS 1000  $ Create 1000000 particles
IDUM 0 1 2 1 J 1 1 1
RDUM 0.001 0.001
FILES 21 DUMN1
c TALLIES
F1:n 2.3
C1   0 1
PRINT 10 40 50 110 126 140
c from 0 to 14 MeV in 100 keV intervals
c Set the energy bin structure for this tally
c from 0 to 14 MeV in 100 keV intervals
E1 0 0.5 100I 14 15
c DEFINE MATERIALS
c  ZZAAA atom_fraction  ZZAAA atom_fraction
m1 6000   5.0069e-1  1002  4.9581e-1   1001  3.5048e-3
 $ Material 1:C6D6
m13  13027 1 $ Material 13 : Aluminum
c ptrac file=asc write=all max=-1e4 event=src
```

CHAPTER VI

Conclusions and Future Work

6.1 Conclusions

In this thesis we have demonstrated and conclude that C_6D_6 detectors can be used to study (d,n) analog reactions to (p, γ) radiative capture reactions and other reactions important in astrophysics. Experiments to explore experiments of this nature are planned at UND and new facilities at MSU.

The results presented in the previous chapters are extremely encouraging. There were a few doubts about the success of the planned experiments, primarily because, though the idea behind recoil deuteron liquid scintillator was not new, there is almost no data showing it is feasible as a practical detector for fast neutrons in accelerator experiments. However, the present data and simulations show that with further work most (d,n) reactions likely can be studied using C_6D_6 detectors.

These detectors are particularly a better choice for neutron measurements than C_6H_6 where ToF cannot be used because of the forward recoiling deuteron in the spectra. As noted, the d + d cross section was obtained using the neutron peak efficiency. It is important to note that the peak efficiency is not dependent on threshold setting or even gain shifts. This gives the C_6D_6 detectors a major advantage over the proton recoil detectors.

6.2 Future Work

The most meaningful next step will be to develop a better way to use this new detector to extract accurate (d,n) cross sections, further test and improve the accuracy of the simulations, and then use these detectors in RNB studies. This can extend existing (d,n) studies and obtain absolute spectroscopic factors for short-lived nuclei. Of particular interest are reactions such as ^{7}Be(d,n) (fig. 1.2)

Other applications would be to explore their uses in nuclear nonproliferation detection and analysis. (A grant proposal for this has been submitted). Another application would be to use a C_6D_6 detector in conjunction with Si detectors to identify ^{5}He reaction products, e.g. in (^{6}He,^{5}He) etc. (fig. 6.1).

6.3 Improvements for Future Measurements

To improve these detectors for use in future RNB experiments, several things should be done:

(1) Employ a better optical grease (such as St. Gobain BC-630) to enhance coupling.

(2) Add a stabilized LED pulser with fiber optical cable to the scintillator-PMT to monitor PMT gain.

(3) Purchase larger volume detectors to improve peak and total efficency for RNB work.

(4) Utilize faster and newer PMTs to further improve PSD.

(5) Employ remote controlled multi channel HV-power supply system to permit better PMT gain matching.

(6) Perform a more accurate efficiency measurement using a deuteron gas cell (to avoid carbon) with 3He recoil tagging for d+d events producing neutrons.

(7) Perform more (d,n) measurements at higher deuteron energy to test the MC simulations to higher energies.

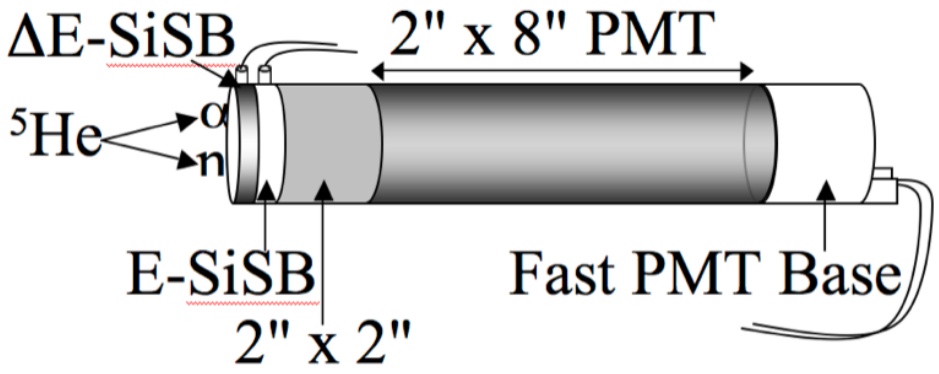

Figure 6.1: Proposed schematic for ^{5}He measurements using C_6D_6 detector

APPENDICES

APPENDIX A

Computer Codes

A.1 Elastic Scattering

For the deuterated scintillator, the most dominant reaction for the production of light is the elastic scattering reaction. The energy from elastic scattering is deduced as follows: Once the particle direction is sampled from the appropriate n + p or n + d angular distribution look up tables, the exiting nuclear recoil energy, E_{out}, is then dictated by two-body kinematics:

$$E_{out} = 1/2E_n[(1-\alpha)\mu_{cm} + 1 + \alpha] \tag{A.1}$$

$$= E_n[(1 + A^2 + 2A\mu_{cm})/(1 + A)^2] \tag{A.2}$$

where E_{in} = incident neutron energy, μ_{cm} = center-of-mass cosine of the angle between incident and exiting particle directions, and

$$\alpha = ((A-1)/(A+1))^2 \tag{A.3}$$

where A = mass of collision target nucleus in units of the mass of a neutron (atomic weight ratio).

A.1.1 Neutron on Deuteron Elastic Collision

In a two body collision process, a particle of mass M_b, at rest in the laboratory is hit by a particle of mass M_a, momentum p_1 and kinetic energy k_1. From conservation of energy and momentum we have

$$1/2M_aV_a^2 + 1/2M_bV_b^2 = 1/2M_aV_{af}^2 + 1/2M_bV_{bf}^2 \tag{A.4}$$

and

$$M_a\boldsymbol{V}_a + M_b\boldsymbol{V}_b = M_a\boldsymbol{V}_{af} + M_b\boldsymbol{V}_{bf} \tag{A.5}$$

Since both masses are known, one can solve both equations simultaneously to get the final velocities.

$$1/2M_aV_a^2 = 1/2M_aV_{af}^2 + 1/2M_bV_{bf}^2 \tag{A.6}$$

$$M_a\boldsymbol{V}_a + M_b\boldsymbol{V}_b = M_a\boldsymbol{V}_{af} + M_b\boldsymbol{V}_{bf} \tag{A.7}$$

Rearranging the above equations gives us

$$M_bV_b^2 = (M_aV^2 - V_a^2) = M_a(\boldsymbol{V} - \boldsymbol{V}_{af})(\boldsymbol{V} + \boldsymbol{V}_{af}) \tag{A.8}$$

$$M_b\boldsymbol{V}_b = M_a(\boldsymbol{V} - \boldsymbol{V}_a) \tag{A.9}$$

Now dividing and substituting gives

$$\boldsymbol{V}_{bf} = 2M_a/(M_a + M_b) * \boldsymbol{V}_a = 2/3 * \boldsymbol{V}_a \tag{A.10}$$

for the case of the deuteron this becomes

$$1/2(2)V_{bf}^2 = 1/2(4/9(2))V_a^2 \tag{A.11}$$

Thus,

$$E_d^{max} = 8/9 E_n \tag{A.12}$$

where $E^{max}{}_d$ is the energy (a maximum) of a forward recoiling deuteron and for a proton,

$$E_p^{max} = E_n \tag{A.13}$$

where $E^{max}{}_p$ is the energy (a maximum) of a recoiling proton (see figure 3.8).

A.2 Monte Carlo Simulation

To study the detector response to particles such as neutrons and gammas, a Monte Carlo simulation code segment was written in both MCNP and MCNP-Polimi [Briesmeister, 1988][Pozzi, 2003].

A.2.1 MCNP

MCNP is a general-purpose continuous-energy, generalized-geometry, time-dependent neutron, photon and electron Monte Carlo transport code [Briesmeister, 1988]. This code can be used in multiple transport modes: neutron only, photon only, electron only or multiple combinations such as photon/neutron transport, where the photons are produced by neutron interactions. MCNP can handle a wide range of energies for the various particles: neutron energy range from 10^{-11} MeV to 20 MeV for all stable nuclear target isotopes and up to 150 MeV for some isotopes depending on the cross sections needed. The photon energy range is from 1 keV to 100 GeV and the electron energy is from keV to 1GeV.

The code is structured in the following way: An input file is created that contains the geometric specification for the detector, a description of the materials, a selection

of cross-section evaluations, the location and characteristics of the neutrons and photon values for specified tallies desired, and a variance reduction technique that is used to improve efficiency.

It is important to note that MCNP uses continous-energy nuclear and atomic data libraries. The main sources of the nuclear data are those from the Evaluated Nuclear Data File (ENDF) [Chadwick, 2006] system, Advanced Computational Technology Initiative (ACTI), The Evaluated Nuclear Data Library (ENDL), Evaluated Photon Data Data Library (EPDL), and compilations from Livermore and evaluation from the Nuclear Physics (T-16) Group at Los Alamos. A modification of the MCNP code was written (for both C_6D_6 and C_6H_6) to simulate the detector response to the various particles and the output from the simulation is shown in its entirety in Appendix C.

A.2.2 MCNP Polimi

MCNP-Polimi is a further modification of the standard MCNP code described above. MCNP-Polimi introduced new features that pertains to the physics of particle transport. Even though the Polimi code preserves most parts of the standard MCNP, the code runs with analog particle tracking [Pozzi, 2002]. This simply means that every particle that is created or generated by the source is assigned a weight. This way, one can effectively count and collect all the particles. Essentially, the Polimi code allows one to track individual particle history in the simulation. This was not possible in the standard MCNP. Within the Polimi input file, one must include the following [IDUM 0 1 2 1 J 1 1 1], [RDUM 0.001 0.001], [FILES 21 DUMN1] in order to generate the Polimi data file that is processed by the post-processor.

Another important feature of the MCNP-Polimi code is the Polimi data file. This is an additional ascii file. The Polimi package comes with a MatLab post-processor

code. One has to modify the post-processor to suit the specific detector. This post processor allows the direct collection and accumulation of the light created by the scintillator. A detection happens in a scintillator when neutrons or photons deposit enough energy to overcome a given threshold. Photons (x-rays and γ-rays) will deposit their energy primarily by Compton scattering on electrons while neutrons in organic scintillator interact by elastic and inelastic scattering with hydrogen, deuterium and carbon nuclei. The light output of each interaction that occurs within the scintillator depends on the ionizing particle to which energy is transferred (electron, proton, deuteron, or carbon nucleus) [Chiang, Oberer, and Pozzi, 2000]. To obtain the light output by the collisions, each collision within the pulse generation time is taken into account.

The major advantage of the post-processing code is that it takes into account many of details of the physics of detection, such as neutron collisions with carbon as well as multiple scatterings. Also, the secondary photons generated by neutrons in inelastic scattering on carbon are taken into account. The code written for C_6D_6, together with the output file(s) are shown in Appendix C.

APPENDIX B

Neutron Generators

As part of the initial test of the liquid scintillators, two neutron generators, Thermo Scientific Mp300 DD and the Thermo Scientific-D711 DT generators, in the Neutron Science Laboratory in the Nuclear Engineering Department were used. The specifications of both detectors are given below. The DD generator produces approximately 2.5 MeV neutrons, nearly isotropic neutrons while the DT generator produces nearly 14.1 MeV neutrons. The KMAX setup shown in section 3.1 (figure 3.1) was used to collect data with the generators.

B.1 DD Generator

The DD neutron generator is a small compact and portable neutron source device compact linear accelerator. The machine works by accelerating deuterium beam into a metal hydride target which contains deuterium. This reaction (D+D) results in a ^{3}He ion, and a neutron with a kinetic energy of approximately 2.5 MeV. Pictures of the setup using the DD generator with the liquid scintillators is shown in figure B.1.

B.2 DT Neutron Generator

The Thermo-Scintific D 711 DT neutron generator is housed in the Neutron Science Laboratory in the UM Nuclear Engineering Department. The generator consists of four main parts: the accelerator head, a control chassis, cooling units, and the

D+D MP 320 Neutron Generator Specifications	
Max Neutron Yield	1.0 x 10^8 n/s
Neutron Energy	2.45 MeV
Typical Lifetime	1,200 hours at 1.0 x 10^8 n/s
Pulse Rate	250 Hz to 20 kHz, continuous
Duty Factor	5% to 100%
Minimum Pulse Width	5 μsec
Pulse Rise Time	Less than 1.5 μsec
Pulse Fall Time	Less than 1.5 μsec
Maximum Accelerator Voltage	95 kV
Max Beam Current	60 μamps
Power Supply	Integral
Neutron Module	12.07 cm x 57.15 cm (4.75 in x 22.5 in)
Control Module	Integral, digital
Safety Features	Keylock: on/off
	Emergency: on/off
	Normal-open and normal-closed interlocks
	Pressure switch

Table B.1: DD Neutron generator properties

D+T D711 Neutron Generator Specifications	
DT Neutron Yield	2.0 x 10^8 n/s
Neutron Energy	14 MeV
Max Neutron Flux	1 x 10^9 n/cm^2/sec at 2 x 10^{10} n/s output
Typical Tube Lifetime	1000 hours at 1.0 x 10^{10} n/s
Control Interfaces	RS-232, RS-422, or RS-485
Operation Mode	Continuous only
Maximum Accelerator Voltage	120 to 160 kV
Operating Beam Current	0.5 to 3.0 mA
Neutron Module	12.07 cm x 57.15 cm (4.75 in x 22.5 in)
Total System Weight	1000 kg
Safety Features	Keylock: on/off on console and remote EMO box
	SmartLamp
	Normal open and normal closed contacts
	Pressure safety switches on power supply
	Pressure safety switch on accelerator head
	Continuous real-time monitoring
	Simple GUI interface

Table B.2: DT Neutron generator properties

accelerating high voltage power supply. The sealed neutron tube is designed for a maximum yield of 2x10^{10} n/s. When running, care was taken to make sure the coolant units were operational as these cool both the target and the ion source. In general, when this machine is operated at lower yields, one can drastically extend the tube lifetime. Running at 5 x 10^9 n/s for example would increase the expected lifetime to 2,000 hours.

The neutron energy from the DT generator varies slightly with angle as can be seen in figure B.2.

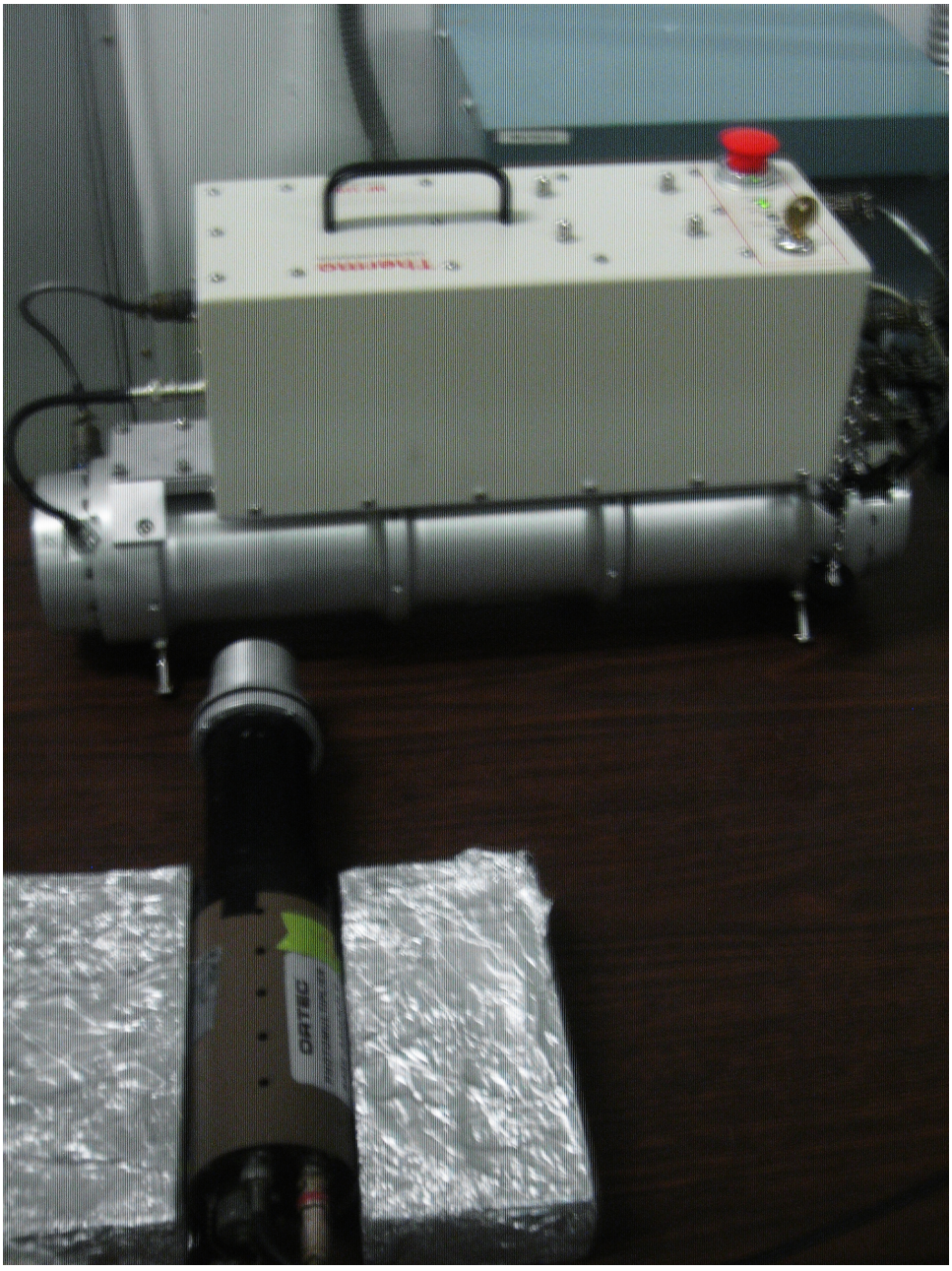

Figure B.1: D+D experimental setup.

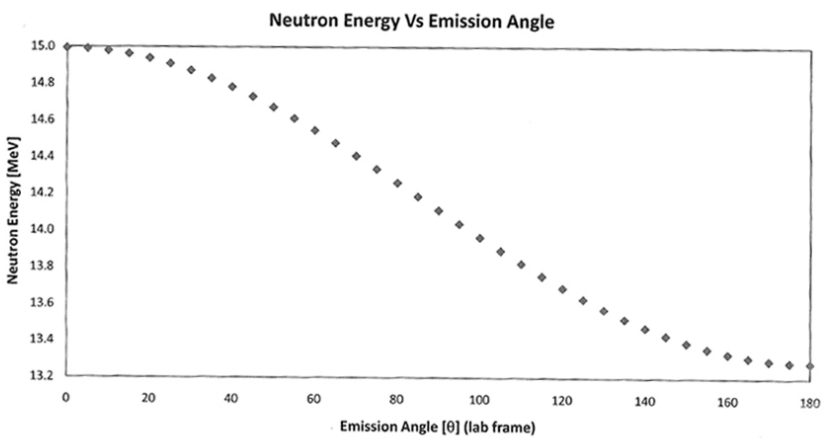

Figure B.2: DT generator neutron energy vs. emission angle.

Figure B.3: DT neutron generator.

Figure B.4: Scintillator in DT neutron generator cave.

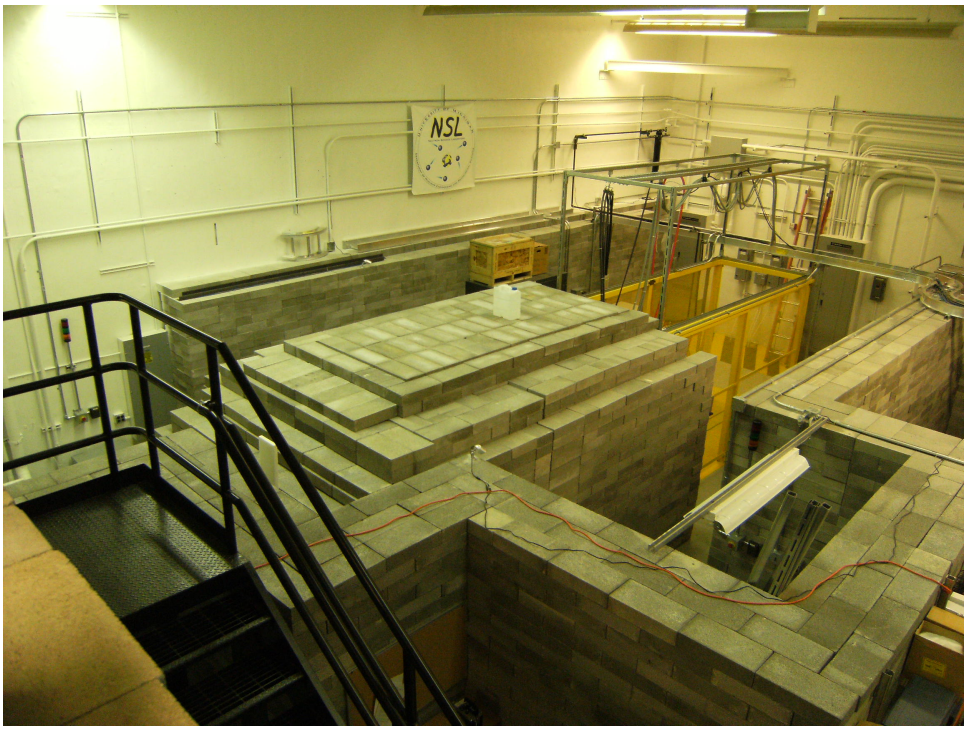

Figure B.5: DT neutron generator room layout.

APPENDIX C

Monte Carlo Simulation Code

The MCNP simulation code that was written as part of this thesis is shown below.

C.0.1 MCNP

```
The entire MCNP code and output files written as part
of this thesis are shown below.
\subsection{MCNP-Code and Output File}
\begin{verbatim}
Deuterated Liquid Scintillator Simulation Input File
c VOLUMETRIC GEOMETRY DEFINITION "CELL CARDS"
c
c CELL_NUM  MAT_NO  DENSITY(g/cc) SURFACE_CONSTRAINTS
1  1 -0.954  -1  imp:n=1   $ Detector
2 13  -2.7 1 -2   imp:n=1   $ Aluminum Shell
3  0  2 -999  imp:n=1   $ Vacuum
999 0   999 imp:n=0   $ The outside world
c
c SURFACE DEFINITIONS "SURFACE CARDS"
c define the surfaces that form volumes
c
c      ORIGIN    AXIS_VECTOR    RADIUS
1 RCC   0 0 0  5.08 0 0   2.54    $ Detector
2 RCC -0.05 0 0  5.13 0 0   2.59
$ Aluminum around detector
c    xmin xmax  ymin ymax  zmin zmax
999 RPP -10   10   -10   10   -10   10
 $ Box bounding our region of interest
c
c EVERYTHING ELSE "DATA CARDS"
c Define the source of neutrons
SDEF POS=0 0 0 AXS 0 0 1 RAD=d1
PAR=1  ERG=14.1 VEC= 0 0 1 DIR=1
SI1 0 2.54
c
c Define the problem type/mode
mode n
phys:n
c The PHYS and CUT cards are essential for analog MC
PHYS:N J 20    $Mo
CUT:N 30  $mo
c Limit how long we run this problem
c ctme 0.1  $ Max run time in minutes  $MO
c
c Limit how many particles get created
NPS 1E4  $ Create 10000 particles
c
```

```
c TALLIES
c
c Create a cell flux tally for cell 1
c NAME IT
c FC14  Volume averaged cell flux for detector
c DEFINE IT
c F8:p 1
F14:N  1
c F24:p  1
c Set the energy bin structure for this tally
c from 0 to 14 MeV in 100 keV intervals
c FC16  Cell averaged energy deposited
c DEFINE IT
c F16:N  1
c Set the energy bin structure for this tally
c from 0 to 14 MeV in 100 keV intervals
E14 0 0.5 100I 14 15
c E24 0 0.1 139I 14
c E8:p .001 98I 0.7
c
c DEFINE MATERIALS
c  ZZAAA atom_fraction  ZZAAA atom_fraction
m1 6000  141   1002  141    1001 1
    $ Material 1 : Liquid Scintillator
m13 13027 1     $ Material 13: Aluminum
```

The Sample Output File from the simulation

```
Thread Name & Version = MCNP5_RSICC, 1.40                                      -
 |   This program was prepared by the Regents
 of the University of  California at Los Alamos
 National Laboratory (the University) under |
 |  contract number W-7405-ENG-36 with
 the U.S. Department of Energy (DoE).
1mcnp     version 5     ld=11012005 12/30/08 12:21:04
 probid =  12/30/08 12:21:04
 i=14EN o=14.o
    1-  Neutron Detection With Liquid Scintillators
    2-    c
    3-   c VOLUMETRIC GEOMETRY DEFINITION "CELL CARDS"
    4-    c
    5-  c CELL_NUM  MAT_NO  DENSITY(g/cc) SURFACE_CONSTRAINTS
    6-  1   1 -0.954  -1   imp:n=1   $ Detector
    7-  2  13    -2.7  1 -2  imp:n=1   $ Aluminum Shell
    8- 3  0   2 -999  imp:n=1   $ Vacuum
    9-  999   0   999    imp:n=0   $ The outside wor
   10-
   11-       c
   12-       c SURFACE DEFINITIONS "SURFACE CARDS"
   13-       c define the surfaces that form volumes
   14-       c
   15-       c      ORIGIN    AXIS_VECTOR    RADIUS
   16-       1 RCC   0 0 0      5.08 0 0      2.54    $ Detector
   17-       2 RCC -0.05 0 0    5.13 0 0      2.59
    $ Aluminum around detector
   18-       c       xmin xmax  ymin ymax  zmin zmax
   19-       999 RPP -10   10   -10   10   -10   10
   $ Box bounding our region of interest
   23-       c EVERYTHING ELSE "DATA CARDS"
   24-       c
   25-       c
   26-       c Define the source of neutrons
   27-       SDEF POS=-0.06 0 0 AXS 1 0 0 RAD=d1
   PAR=1  ERG=14.1 VEC= 1 0 0 DIR=1
   28-       SI1 0 2.54
```

```
   29-       c
   30-       c Define the problem type/mode
   31-       mode n
   32-       phys:n
   33-The PHYS cards and CUT cards are essential for analog MC
   34-       c PHYS:N J 20    $Mo
   35-       c CUT:N 30  $mo
   36-       c
   37-       c Limit how long we run this problem
   38-       c ctme 0.1  $ Max run time in minutes  $MO
   39-       c
   40-       c Limit how many particles get created
   41-       NPS 1E4  $ Create 10000 particles
   42-       c
   43-       c TALLIES
   44-       c
   45-       c Create a cell flux tally for cell 1
   46-       c NAME IT
   47-       c FC14  Volume averaged cell flux for detector
   48-       c DEFINE IT
   49-       c F8:p 1
   50-       F14:N  1
   51-       c F24:p  1
   52-       c Set the energy bin structure for this tally
   53-       c from 0 to 14 MeV in 100 keV intervals
   54-       c FC16  Cell averaged energy deposited
   55-       c DEFINE IT
   56-       c F16:N  1
   57-       c Set the energy bin structure for this tally
   58-       c from 0 to 14 MeV in 100 keV intervals
   59-       E14 0 0.5 100I 14 15
   60-       c E24 0 0.1 139I 14
   61-       c E8:p .001 98I 0.7
   62-       c
   65-       c DEFINE MATERIALS
   66-       c  ZZAAA atom_fraction  ZZAAA atom_fraction
   67-   m1 6000  141   1002  141 1001 1
   68-       m13 13027 1
   69-       c ptrac file=asc write=all max=-1e4 event=src
************************************************
 * Random Number Generator  =                  1 *
 * Random Number Seed       =       19073486328125 *
 * Random Number Multiplier =       19073486328125 *
 * Random Number Adder      =                    0 *
 * Random Number Bits Used  =                   48 *
 * Random Number Stride     =               152917 *
*******************************
1problem summary
  run terminated when   10000  particle histories were done. +
  Neutron Detection With Liquid Scintillators
  probid =  12/30/08 12:21:04
 neutron creation    tracks      weight
 energy    neutron loss  tracks  weight   energy
 (per source particle)   (per source particle)
 source 10000    1.0000E+00    1.4100E+01
 escape    10337    1.0184E+00    1.2274E+01
 energy cutoff    0    0.            0.
 time cutoff   0  0.    0.
 weight window    0  0.  0.
 weight window    0    0.   0.
 cell importance 0    0. 0
   cell importance  0    0.  0.
 weight cutoff      0 0. 0
 weight cutoff  0  0.  0.
 upscattering  0    0. 0.
```

```
 downscattering  0 0  1.4112E+00
 photonuclear    0    0.   0.
neutron tracks per source particle     1.0674E+00
escape            3.1128E-01          tco   1.0000E+33
 neutron collisions per source particle 4.8650E-01
 capture           4.8686E-02           eco   0.0000E+00
   total neutron collisions     4865
   capture or escape 3.0744E-01  wc1  -5.0000E-01
   net multiplication   1.0335E+00 0.0017
   any termination   2.9778E-01           wc2  -2.5000E-01
 computer time so far in this run     0.02 minutes
 maximum number ever in bank          2
 computer time in mcrun    0.00 minutes
 bank overflows to backup file        0
 source particles per minute  6.0000E+05
 random numbers generated     86792
 most random numbers used was 118 in history   7036
 range of sampled source weights = 1.0000E+00 to 1.0000E+00
1neutron  activity in each cell   print table
  tracks     population   collisions   collisions
   number  flux  average      average
cell    entering     * weight
weighted     weighted   track weight   track mfp
(per history)    energy  energy  (relative)      (cm)
1  1    9999    10325          4767    4.7220E-01
1.1110E+01  1.3132E+01   9.9288E-01   1.1030E
 2     2  12448  10223    98    9.6551E-03   9.2149E+00
 1.2219E+01   9.8655E-01   9.0850E
 3     3   20337  10337  0    0.0000E+00   7.3981E+00
 1.1025E+01   9.8022E-01   0.0000E
total     42784  30885    4865    4.8186E-01
1tally  14  nps =   10000
 tally type 4    track length estimate of particle flux.
  units   1/cm**2    tally for  neutrons
volumes
cell:        1 1.02963E+02
 cell  1
      energy
    0.0000E+00   0.00000E+00 0.0000
    5.0000E-01   5.44467E-04 0.0892
    6.3366E-01   1.07222E-04 0.1594
    7.6733E-01   1.06336E-04 0.1554
    9.0099E-01   4.50873E-05 0.2144
    1.0347E+00   6.92578E-05 0.1807
    1.1683E+00   6.11504E-05 0.1961
    1.3020E+00   5.80448E-05 0.2110
    1.4356E+00   7.50532E-05 0.1911
    1.5693E+00   4.59654E-05 0.2072
    1.7030E+00   9.92956E-05 0.1652
    1.8366E+00   9.38362E-05 0.1674
    1.9703E+00   9.69052E-05 0.1635
    2.1040E+00   6.54184E-05 0.1965
    2.2376E+00   5.53367E-05 0.1936
    2.3713E+00   5.32417E-05 0.2205
    2.5050E+00   7.55759E-05 0.1900
    2.6386E+00   8.45825E-05 0.1767
    2.7723E+00   3.02965E-05 0.2443
    2.9059E+00   4.12324E-05 0.2273
    3.0396E+00   6.20163E-05 0.2000
    3.1733E+00   5.83754E-05 0.1905
    3.3069E+00   5.55591E-05 0.2224
    3.4406E+00   4.88731E-05 0.2178
    3.5743E+00   5.96638E-05 0.2184
    3.7079E+00   4.74122E-05 0.2176
    3.8416E+00   6.05196E-05 0.2053
    3.9752E+00   5.93578E-05 0.2059
    4.1089E+00   4.32689E-05 0.2124
    4.2426E+00   4.69093E-05 0.2691
    4.3762E+00   3.45217E-05 0.2559
```

```
    4.5099E+00   4.29242E-05 0.2464
    4.6436E+00   2.26585E-05 0.3058
    4.7772E+00   2.18502E-05 0.3481
    4.9109E+00   4.18026E-05 0.2531
    5.0446E+00   2.93720E-05 0.2836
    5.1782E+00   4.00053E-05 0.2527
    5.3119E+00   2.27307E-05 0.3294
    5.4455E+00   2.22064E-05 0.3325
    5.5792E+00   3.48015E-05 0.2625
    5.7129E+00   3.88179E-05 0.2794
    5.8465E+00   2.64593E-05 0.3123
    5.9802E+00   2.75901E-05 0.3209
    6.1139E+00   4.58648E-05 0.2568
    6.2475E+00   4.83157E-05 0.2378
    6.3812E+00   4.32750E-05 0.2475
    6.5149E+00   6.38867E-05 0.1990
    6.6485E+00   4.88831E-05 0.2203
    6.7822E+00   5.50969E-05 0.2214
    6.9158E+00   4.41799E-05 0.2467
    7.0495E+00   2.73596E-05 0.2921
    7.1832E+00   7.10902E-05 0.1924
    7.3168E+00   4.78561E-05 0.2170
    7.4505E+00   6.29069E-05 0.2129
    7.5842E+00   3.41173E-05 0.2589
    7.7178E+00   4.02333E-05 0.2283
    7.8515E+00   4.09826E-05 0.2598
    7.9851E+00   3.27885E-05 0.2673
    8.1188E+00   3.79415E-05 0.2709
    8.2525E+00   2.99707E-05 0.2885
    8.3861E+00   2.95639E-05 0.2822
    8.5198E+00   6.15295E-05 0.1947
    8.6535E+00   3.78435E-05 0.2370
    8.7871E+00   3.81998E-05 0.2653
    8.9208E+00   6.73557E-05 0.2158
    9.0545E+00   5.71951E-05 0.2163
    9.1881E+00   6.57973E-05 0.1991
    9.3218E+00   8.62817E-05 0.1804
    9.4554E+00   7.88072E-05 0.1854
    9.5891E+00   7.09576E-05 0.1948
    9.7228E+00   4.34871E-05 0.2554
    9.8564E+00   2.50831E-05 0.3061
    9.9901E+00   2.85738E-05 0.3180
    1.0124E+01   6.96173E-05 0.2028
    1.0257E+01   5.02929E-05 0.2053
    1.0391E+01   7.08211E-05 0.1912
    1.0525E+01   6.54290E-05 0.2208
    1.0658E+01   5.05779E-05 0.2303
    1.0792E+01   6.32653E-05 0.2081
    1.0926E+01   6.39479E-05 0.2234
    1.1059E+01   4.98965E-05 0.2443
    1.1193E+01   7.46310E-05 0.1876
    1.1327E+01   7.38675E-05 0.1900
    1.1460E+01   6.64237E-05 0.1872
    1.1594E+01   8.77049E-05 0.1825
    1.1728E+01   5.95069E-05 0.2046
    1.1861E+01   9.10140E-05 0.1811
    1.1995E+01   6.63305E-05 0.1967
    1.2129E+01   7.90550E-05 0.1888
    1.2262E+01   9.57977E-05 0.1689
    1.2396E+01   1.04306E-04 0.1611
    1.2530E+01   7.84404E-05 0.1785
    1.2663E+01   1.00474E-04 0.1724
    1.2797E+01   9.84904E-05 0.1757
    1.2931E+01   9.82125E-05 0.1665
    1.3064E+01   1.01063E-04 0.1678
    1.3198E+01   8.17142E-05 0.1947
    1.3332E+01   1.25671E-04 0.1529
    1.3465E+01   1.61983E-04 0.1298
    1.3599E+01   2.52917E-04 0.1065
    1.3733E+01   3.44722E-04 0.0927
    1.3866E+01   5.18576E-04 0.0728
    1.4000E+01   6.52313E-04 0.0652
    1.5000E+01   4.01861E-02 0.0038
      total      4.83046E-02 0.0024
=========================================
 this tally meets the statistical criteria used to form
 confidence intervals:
```

```
 check the tally fluctuation chart to verify.
 the results in other bins associated with
  this tally
      estimated quantities   value at nps value at nps+1
          value(nps+1)/value(nps)-1.
      mean                              4.83046E-02
      4.83192E-02                       0.000303
      relative error                    2.41670E-03
      2.43469E-03                       0.007442
      variance of the variance          1.48420E-03
      1.67592E-03                       0.129171
      shifted center                    4.83048E-02
       4.83048E-02                       0.000001
      figure of merit                   9.39263E+07
       9.25437E+07                      -0.014720
 the estimated slope of the 200 largest  tallies
 starting at  7.88092E+00 appears to be decreasing
  at least exponentially. the large score tail of the
  empirical history score probability
 density function appears to have
 no unsampled regions
 tally   result of statistical checks for the tfc bin
  (the first check not passed is listed) and error magnitude
  check for all bins
   14   passed the 10 statistical checks for the tally
   fluctuation chart bin result
  missed all bin error check:   105 tally bins had
   1 bins with zeros and    98 bins with relative
 errors exceeding 0.10
 the 10 statistical checks are only for the tally fluctuation
  chart bin and do not apply to other tally bins.
the tally bins with zeros may or may not be correct:
 compare the source, cutoffs, multipliers, et cetera
with the tally bins.
 warning.     1 of the   1 tallies had bins with relative errors
  greater than recommended.
1tally fluctuation charts
  tally   14
          nps      mean     error   vov  slope    fom
         1000   4.7387E-02 0.0078 0.0075 10.0 6.3E+07
         2000   4.8085E-02 0.0052 0.0072 10.0 7.0E+07
         3000   4.8007E-02 0.0042 0.0043 10.0 7.2E+07
         4000   4.8267E-02 0.0037 0.0033 10.0 7.1E+07
         5000   4.8311E-02 0.0034 0.0034 10.0 6.8E+07
         6000   4.8385E-02 0.0031 0.0029 10.0 7.9E+07
         7000   4.8356E-02 0.0029 0.0023 10.0 7.7E+07
         8000   4.8357E-02 0.0027 0.0020 10.0 8.8E+07
         9000   4.8325E-02 0.0025 0.0017 10.0 8.5E+07
        10000   4.8305E-02 0.0024 0.0015 10.0 9.4E+07
************************************************************
\linespread{0.1}
```

C.0.2 MCNP-POLIMI Code and Data file

The MCNP-Polimi code written as part of this thesis is below. The main difference between this code and the standard MCNP is that, this code contains the Polimi-Data input card which the standard MCNP does not have.

```
Neutron Detection With Liquid Scintillators
c
```

```
c VOLUMETRIC GEOMETRY DEFINITION "CELL CARDS"
c
c CELL_NUM  MAT_NO  DENSITY(g/cc) SURFACE_CONSTRAINTS
1   1  -0.954 -1   imp:n=1   $ Detector
2 13    -2.7  1 -2  imp:n=1   $ Aluminum Shell
3  0    2 -999     imp:n=1   $ Vacuum
999   0   999   imp:n=0
$ The outside world (Particle go here to die)
c SURFACE DEFINITIONS "SURFACE CARDS"
c define the surfaces that form volumes
c
c      ORIGIN    AXIS_VECTOR    RADIUS
1 RCC   0 0 0      5.08 0 0      2.54    $ Detector
2 RCC -0.05 0 0    5.13 0 0      2.59
$ Aluminum around detector
c       xmin xmax  ymin ymax  zmin zmax
999 RPP -10   10   -10   10   -10   10
$ Box bounding our region of interest
c EVERYTHING ELSE "DATA CARDS"
c
c
c Define the source of neutrons
SDEF POS=-0.06 0 0 AXS 1 0 0 RAD=d1
PAR=1  ERG=14.1 VEC= 1 0 0 DIR=1
SI1 0 2.54
c
c Define the problem type/mode
mode n
c The f PHYS and CUT cards  essential for analog MC
PHYS:N J 20    $Mo
CUT:N 30  $mo
c
c Limit how long we run this problem
c ctme 0.1  $ Max run time in minutes  $MO
c
c Limit how many particles get created
NPS 1E3  $ Create 10000 particles
IDUM 0 1 2 1 J 1 1 1
RDUM 0.001 0.001
FILES 21 DUMN1
c
c TALLIES
F1:n 2.3
PRINT 10 40 50 110 126 140
c
c from 0 to 14 MeV in 100 keV intervals
c Set the energy bin structure for this tally
c from 0 to 14 MeV in 100 keV intervals
E1 0 0.5 100I 14 15
c
c
c DEFINE MATERIALS
c  ZZAAA atom_fraction  ZZAAA atom_fraction
m1    6000   5.0069e-1    1002  4.9581e-1
1001  3.5048e-3  $ Material 1:C6D6
m13  13027    1        $ Material 13 : Aluminum
c ptrac file=asc write=all max=-1e4 event=src
POLIMI DATA FILE
```

APPENDIX D

KMAX Data Aquisition

D.1 KMAX

As part of the thesis, fellow graduate student Hao Jian and I wrote a new special acquisition program in JAVA for use in on-campus experiments and tests. The KMAX data acquisition system is a multi-parameter, list-mode data acquisition and process control environment [Sparrow Corp]. KMAX can be used to configure and operate data acquisition and process control systems which use modular instrumentation [CAMAC, VME etc]. KMAX provides high-level features for data display and analysis. This program is highly recommended because it is a complete data acquisition system using the common USB-2 computer input.

This acquisition system supports most standard modular instrumentation, including CAMAC, which was used to collect data for the experiment. In principle KMAX can work with any hardware for which native or JAVA drivers are available. KMAX was useful because of the flexibility available to work directly with the spectra. Also, the spectra data was easily transfered to a text file that could easily be incorporated with other data analyzing programs (i.e MATLAB). The KMAX code that was written as part of this thesis is shown in its entirety in Appendix C. Shown figure D.1 is a snap shot of the KMAX interface. Below is one of the KMAX code written as

part of this thesis:

```
-------------------------------------------------------
 Hawk_M4 Toolsheet Version 3.0
 Uses a single AD413 to do event-by-event data acquisition.
  Buffering should be added for highspeed requirements
Changing the LLD could be automated
-------------------------------------------------------
import kmax.ext.*;
import java.lang.*;
import java.math.*;
import java.io.*;
public class Runtime implements KmaxRuntime {
KmaxToolsheet tlsh; // Store a reference to the toolsheet
 environment
KmaxDevice dev;
KmaxWidget report;
KmaxWidget startStop;
KmaxWidget doSort;
KmaxWidget doSave;
KmaxHist dataHist;
KmaxHist dataHist2;
KmaxHist dataHist2D;
KmaxHist dataHist2D_1;
KmaxHist project1;
long startTime,stopTime;
//String fname = "log.txt";
//File logFile = new File(fname);
//BufferedWriter p = new BufferedWriter(logFile);
int count = 0;
int slotADC = 2; // The toolsheet has one CAMAC
 ADc 2249SG 114 in this slot
int slotADC2 = 3;
int numEvents = 0;
//Change these values to change the LLD in the
ADC, value[mVolts] = 2* LLDn
int LLD = 25;
int ULD = 255;
boolean isReady = false;
boolean isRunning = false;
/**
* The 'init' method is executed at compile time.
*/
public void init(KmaxToolsheet toolsheet) {
tlsh = toolsheet; // Save this reference for use in the toolsheet
dev = tlsh.getKmaxDevice("DEV1");
startStop = tlsh.getKmaxWidget("START_STOP");
report = tlsh.getKmaxWidget("REPORT");
dataHist = tlsh.getKmaxHist("DATA_HIST");
dataHist2 = tlsh.getKmaxHist("DATA_HIST2");
dataHist2D = tlsh.getKmaxHist("HIST2D");
dataHist2D_1 = tlsh.getKmaxHist("HIST2D_1");
doSort = tlsh.getKmaxWidget("DO_SORT");
doSave = tlsh.getKmaxWidget("DO_SAVE");
project1=tlsh.getKmaxHist("project1");
dataHist.setEventID(5);
dataHist2.setEventID(5);
} // init
/**
* The 'GO' method is executed when the GO button is clicked.
```

```
*/
public void GO(KmaxToolsheet toolsheet) {
startStop.setProperty("LABEL", "Start");
isReady = false;
isRunning = false;
tlsh.setProperty("STATUSSTR",
"SCM301_AD114.VERSION 1.0");
} // GO
/**
* The 'initDAQ' method is executed when the
initDAQ button is clicked.
*/
public void initDAQ(KmaxWidget widget) {
int[] datArray = new int[1];
int devErr = 0;
if (isRunning) {
tlsh.showWarning
("You must stop Aquisition before Re-initializing.");
return;
}
// Clear the REPORT text widget
report.setProperty("TEXT", "");
report.setProperty("INSERT", "Initializint the controller ....\n")
count = 0;
// Init the controller
devErr = dev.writeInt(28, 8, 26, null, 0, 0);
// SCM 301: CAMAC Initialize.
if (devErr != 0) {
report.setProperty("INSERT",
"device error = " + devErr + "\n");
return;
}
dev.writeInt(28, 9, 26, null, 0, 0); // SCM 301: CAMAC Clear.
dev.writeInt(30, 9, 26, null, 0, 0); // SCM 301: Set CAMAC Inhibit.
dev.writeInt(30, 10, 24, null, 0, 0); // SCM 301: Disable BD Output.
// Calculate and write the LAM mask
datArray[0] = 1 << (slotADC - 1);
dev.writeInt(30, 0, 16, datArray, 0, 1); // SCM 301: Load LAM Mask.
//datArray[0] = 1 << (slotADC2 - 1);
//dev.writeInt(30, 0, 16, datArray, 0, 1); // SCM 301: Load LAM Mask.
dev.writeInt(10, 0, 26,
report.setProperty("INSERT",
 "Initializint the ADC in slot " + slotADC + "....\n");
setMode(2);
// Initialize the ADC: Coincidence Mode; CAMAC
Random Access; disable Zero Suppression
// Disable Overflow suppression; Disable channel
gates; Enable Master Gate
// devErr = dev.writeInt(slotADC, 0, 9, null, 0, 0);
// AD 114 ADC: Clear module.
devErr = dev.writeInt(slotADC, 0, 9, null, 0, 0);
devErr = dev.writeInt(slotADC2, 0, 9, null, 0, 0);
if (devErr != 0) {
report.setProperty("INSERT", "device error = " + devErr + "\n");
return;
}
} // initDAQ
/**
```

```
* The 'SRQ' method is executed when a device requests service.
*/
int status;
int[] tempData = new int[3]; // a temp array for the reads.
int[] tempData2 = new int[1];
double PSD;
int result;
public void SRQ(KmaxDevice device) {
count++;
tlsh.setProperty("STATUSSTR", "SRQ event " + count);
// report.setProperty("INSERT","event="+count+"\n");
int[] statArray = new int[1];
setMode(2);
int error = dev.writeInt(30, 9, 26, null, 0, 0);
// SCM 301: Set CAMAC Inhibit.
numEvents ++;
// This is the actual readout
error = dev.readInt(slotADC, 11, 2, tempData, 0, 1);
// AD 114 ADC:READ DATA.
//error = dev.readInt(slotADC2, 11, 2, tempData2, 0, 1);
tempData2[0]=tempData[0]/4;
//report.setProperty("INSERT",tempData[0]+"\n");
error = dev.readInt(0, 0, 1, statArray, 0, 1); // get the status.
if (statArray[0] != 0 ) { // We had an IO error
tlsh.setProperty("STATUSSTR", "IO error while reading ADC
 in SRQ, restart required.");
return;
}
if (result == KmaxToolsheet.BUFFER_FULL) {
result = tlsh.clearEventBuffer(tlsh.PRIMARY_BUFFER);
tlsh.addEventRecord(tlsh.PRIMARY_BUFFER, 5, 3, tempData);
tlsh.setProperty("STATUSSTR", "numEvents = " + numEvents);
UPDATE_HIST(null);
report.setProperty("INSERT","Block read\n");
}
else if (result != 0 ) { // We had a buffer error
tlsh.setProperty("STATUSSTR", "Buffer error while adding
event record, restart required.");
return;
}
dev.writeInt(30, 9, 24, null, 0, 0); // SCM 301:
Remove CAMAC Inhibit
* The 'HALT' method is executed when the HALT button is clicked.
*/
public void HALT(KmaxToolsheet toolsheet) {
tlsh.setProperty("STATUSSTR", "HALT event!");
}// HALT
public void reStart() {
dev.writeInt (slotADC, 0, 26, null, 0, 0) ; //  AD 114 ADC:Enable ADC.:
dev.writeInt (slotADC2, 0, 26, null, 0, 0);
dev.writeInt(slotADC, 0, 9, null, 0, 0); // AD 114 ADC: Clear module.
dev.writeInt(slotADC2, 0, 9, null, 0, 0);
dev.writeInt(30, 9, 24, null, 0, 0)// SCM301: Remove CAMAC Inhibit.
} // reStart
* The 'START_STOP' method is executed when the START_STOP
 button is clicked.
*/
public void START_STOP(KmaxWidget widget) {
```

```
if (isRunning) {  // We need to stop the process
dev.writeInt(30, 9, 26, null, 0, 0) // SCM301: Set CAMAC Inhibit.
dev.writeInt(28, 9, 26, null, 0, 0); // SCM 301: CAMAC Clear.
//dev.writeInt(30, 10, 24, null, 0, 0); // SCM 301: Disable BD Output.
int result = 0;
if (doSave.getProperty("VALUE").equals("1"))
result = tlsh.saveEventBuffer(tlsh.PRIMARY_BUFFER);
//report.setProperty("INSERT", "saveEvents returned - " +
 result + "\n");
if (doSort.getProperty("VALUE").equals("1")) {
result = tlsh.sortEventBuffer(tlsh.PRIMARY_BUFFER);
report.setProperty("INSERT", "sortEvents returned - "
+ result + "\n");
}
result = tlsh.clearEventBuffer(tlsh.PRIMARY_BUFFER);
widget.setProperty("LABEL", "Start");
isRunning = false;
tlsh.setProperty("STATUSSTR", "The DAC is stopped.
count = " + count);
stopTime=System.currentTimeMillis();
long runtime=(stopTime-startTime)/1000;
report.setProperty("INSERT","Time = "+runtime+" s\n");
//p.newLine();
//p.write(runtime);
return;
} // The if isRunning scope
if (isReady) { // Then we can start the DAC
reStart();
widget.setProperty("LABEL", "Stop");
isRunning = true;
tlsh.setProperty("STATUSSTR", "The DAC is running.");
startTime=System.currentTimeMillis();
}
else {
tlsh.showWarning("The system is not initialized.  Initialize before
 starting.");
}
} // START_STOP
* The 'CLEAR_REPORT' method is executed when the CLEAR_REPORT
 button is clicked.
*/
public void CLEAR_REPORT(KmaxWidget widget) {
report.setProperty("TEXT", "");
} // CLEAR_REPORT
* The 'CLEAR_HISTS' method is executed when the CLEAR_HISTS button
 is clicked.
public void CLEAR_HIST(KmaxWidget widget) {
dataHist.clear();
dataHist2.clear();
dataHist2D.clear();
dataHist2D_1.clear();
UPDATE_HIST(null);
} // CLEAR_HIST
/**
* The 'UPDATE_HISTS' method is executed when the UPDATE_HISTS
button is clicked.
*/
public void UPDATE_HIST(KmaxWidget widget) {
```

```
dataHist.update();
dataHist2.update();
dataHist2D.update();
dataHist2D_1.update();
} // UPDATE_HISTS
/**
* The 'GET_PROPS ' method is executed when the GET_PROPS
button is clicked.
* It returns all the available properties of the CAMAC system
*/
public void GET_PROPS(KmaxWidget widget) {
int[] data = new int[1];
int error = 0;
setMode(2);
error = dev.readInt(slotADC, 0, 0, data, 0, 1); // AD 114 ADC:Read
 Control Register
if (error != 0) {
tlsh.setProperty("STATUSSTR", "In GET_PROPS:: readInt1, error :: "
+ dev.getErrorMessage(error));
return;
report.setProperty("INSERT", "Control Register = " + data[0] + "\n");
// Get the CAMAC Status
int status = getCAMACStatus();
report.setProperty("INSERT", "CAMAC Status = " + status + "\n");
// Now test the ADC LAM
error = dev.writeInt(slotADC, 0, 8, null, 0, 0)
// D 413 ADC: Test LAM.
if (error != 0) {
tlsh.setProperty("STATUSSTR", "In GET_PROPS:: readInt3, error :: "
+ dev.getErrorMessage(error));
return;
}
status = getCAMACStatus();
if (status == 0)
report.setProperty("INSERT", "ADC LAM = True\n");
else
report.setProperty("INSERT", "ADC LAM = False\n");
} // GET_PROPS
/**
* The getCAMACStatus method is used to get the last status returned.
* Status is implemented in the driver as a pseudo register
*/
public int getCAMACStatus() {
int[] status = new int[1];
int error = dev.readInt( 0, 0, 1, status, 0, 1);
if (error != 0) {
tlsh.setProperty("STATUSSTR", "In getCAMACStatus:: readInt,
error :: "
+ dev.getErrorMessage(error));
return -1;
}
return status[0];
}
/**
* The setMode method is used to set the transfer mode in the controller
* Mode is implemented in the driver as a pseudo register
*/
public void setMode( int mode) {
int[] modeArray = new int[1];
```

```
modeArray[0] = mode;
int error = dev.writeInt( 0, 0, 2, modeArray, 0, 1);
// read the status
 register
if (error != 0) {
tlsh.setProperty("STATUSSTR", "In setMode:: readInt, error :: "
+ dev.getErrorMessage(error));
}// setMode
public void trigger(KmaxWidget widget){
// int[] data1=new int[512];
// data1=dataHist.get1DData();
// for (int i=0;i<10;i++)
// report.setProperty("INSERT",data1[i]+"\n");
tlsh.saveEventBuffer(tlsh.PRIMARY_BUFFER);
tlsh.sortEventBuffer(tlsh.PRIMARY_BUFFER);
//dataHist.update();
//dataHist2.update();
UPDATE_HIST(null);
tlsh.clearEventBuffer(tlsh.PRIMARY_BUFFER);
report.setProperty("INSERT","Update OK\n");
}
public void resolution(KmaxWidget widget){
  double[] res=new double[1];
res=dataHist.getRegionFWHM("reg1");
report.setProperty("INSERT","FWHM of reg1="+res[0]+"\n");
}
public void fileread(KmaxWidget widget) {
int[] blkinfo = new int[3];
String lastName = "";
int totalEvents = 0;
int i;
int n=0;
//int[] rData=new int[262144];
//int[] fdata=new int[90000];
//tlsh.setProperty("BUFSIZE","270000");
while (true) {
n++;
String fileName = tlsh.getEventFile(tlsh.EV_READ_FILE).getName();
if ( !fileName.equals(lastName)) {
report.setProperty("INSERT", "-------------------- "
+ fileName + " --------------------" + "\n");
lastName = fileName;
}
tlsh.clearEventBuffer(tlsh.PRIMARY_BUFFER);
int result = tlsh.readNextBlockHeader(blkinfo);
if (result != tlsh.NO_ERROR) {
tlsh.setProperty("STATUSSTR", "End of file sequence.
result = " + result);
report.setProperty("INSERT", "This is the end of file!\n");
break;
}
report.setProperty("INSERT", "<< TYPE,  SIZE, COUNT >>= "
+ blkinfo[0] + ", " + blkinfo[1] + ", " + blkinfo[2] + "\n" );
totalEvents += blkinfo[2];
tlsh.loadEventBuffer(tlsh.PRIMARY_BUFFER);
tlsh.sortEventBuffer(tlsh.PRIMARY_BUFFER);
report.setProperty("INSERT", n + " blocks read \t");
```

```
}
report.setProperty("INSERT", "Total Events =
"  + totalEvents + "\n" );
report.setProperty("INSERT", "# of blocks =" + (n-1) + "\n");
UPDATE_HIST(null);
}
public void project(KmaxWidget widget){
project1.clear();
String selectedName = dataHist2D_1.getSelectedRegion();
if (selectedName == null)
tlsh.setProperty("STATUSSTR", "No region selected");
else
tlsh.setProperty("STATUSSTR", selectedName + " is selected");
//boolean projectToX = (toX.getProperty("VALUE").equals("1"));
//boolean projectToY = (toY.getProperty("VALUE").equals("1"));
//if (projectToX) {
int result =  dataHist2D_1.projectRegion(selectedName,
"project1", KmaxHist.ALONG_Y);
if (result != 0) { tlsh.setProperty("STATUSSTR", "error:" +
result); return;}
project1.update();
int totalnumber=project1.getTotal();
//tlsh.setProperty("STATUSSTR", "Total Number = "+totalnumber);
//}
/*else {
int result =  Hist2D.projectRegion(selectedName, "project1",
 KmaxHist.ALONG_X);
if (result != 0) { tlsh.setProperty("STATUSSTR", "error"); return;}
project1.update();
int totalnumber=project1.getTotal();
tlsh.setProperty("STATUSSTR", "Total Number = "+totalnumber);
} */
int total=dataHist2D_1.getRegionSum(selectedName);
report.setProperty("INSERT",total + "\n");
}
} // End of the runtime object
```

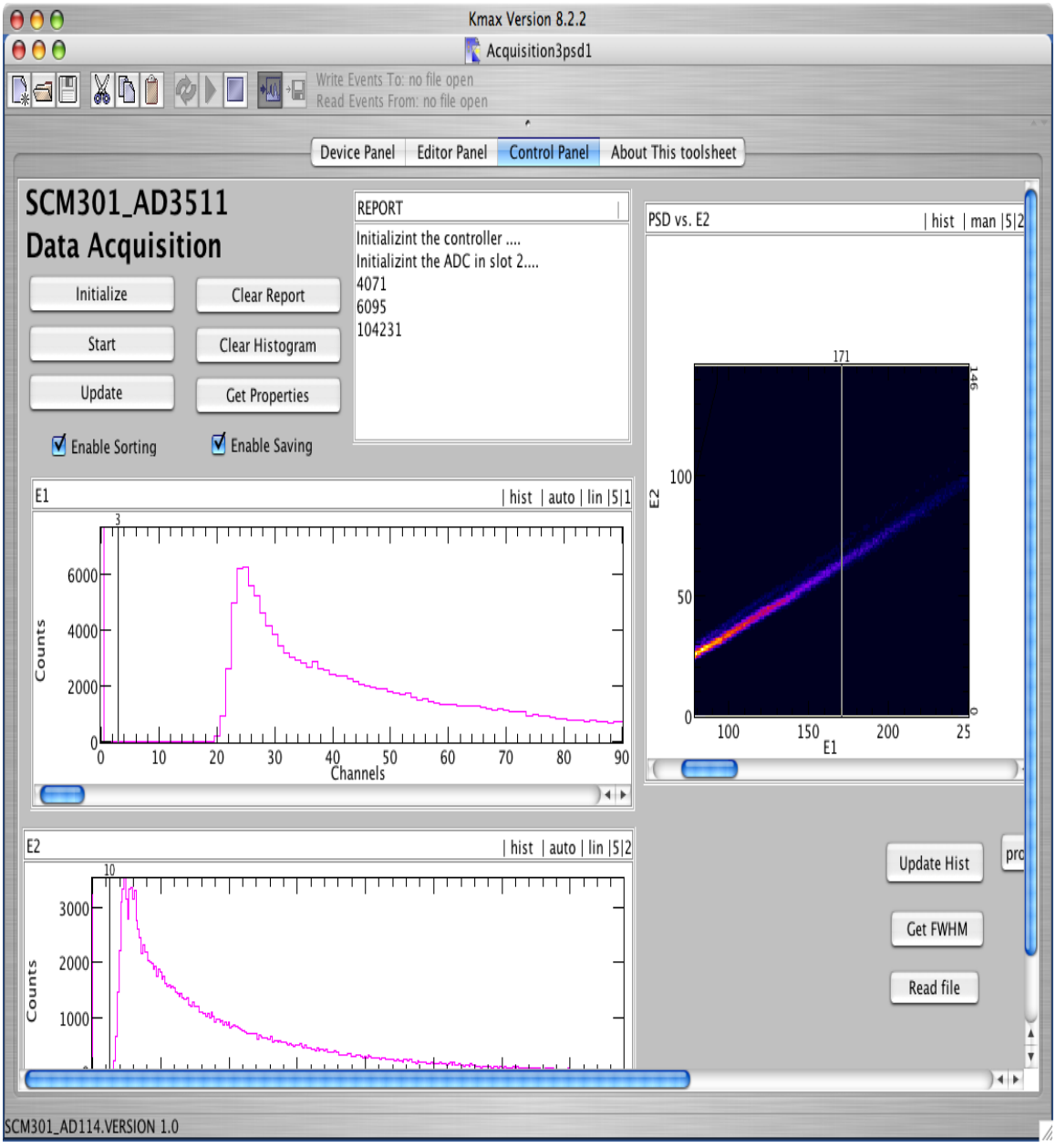

Figure D.1: A snapshot of the Kmax DAQ interface.

APPENDIX E

RCA8575 Photomultiplier and Base

For this thesis, the RCA 8575 PMT was used. This PMT is a 51mm diameter, 12-stage photomultiplier device with a bialkali photocathode (fig. E.1), a pyrex faceplate and an in-line electrostatically-focused copper-berryllium dynode structure. The PMT Anode rise time is 2.8 ns and can handle up to -3000 kV.

E.1 Ortec 265 Base

The ORTEC Model 265A Photomultiplier Base (fig. E.2) is a mechanical assembly with a resistive voltage divider network, with good decoupling, for operation of 12-stage PMTs. It is particularly useful for fast timing or single photon counting. The Model 265A was used with the RCA 8575 for the (d,n) measurements.

The Model 265A PMT Base structure compliments the tube characteristics of both timing and energy resolution by maintaining good pulse fidelity through a wide range of signal currents [Ortec Manual, 2007].

Negative high voltage is applied to the cathode, and the anode is operated essentially at ground potential. The anode output is dc-coupled, with the anode connected to ground through a 50-Ω load resistor. This helps to reduce the baseline shift caused by varying counting rates in ac-coupled systems. The base has two outputs. the negative anode signal that is optimized for timing application and the positive (dynode)

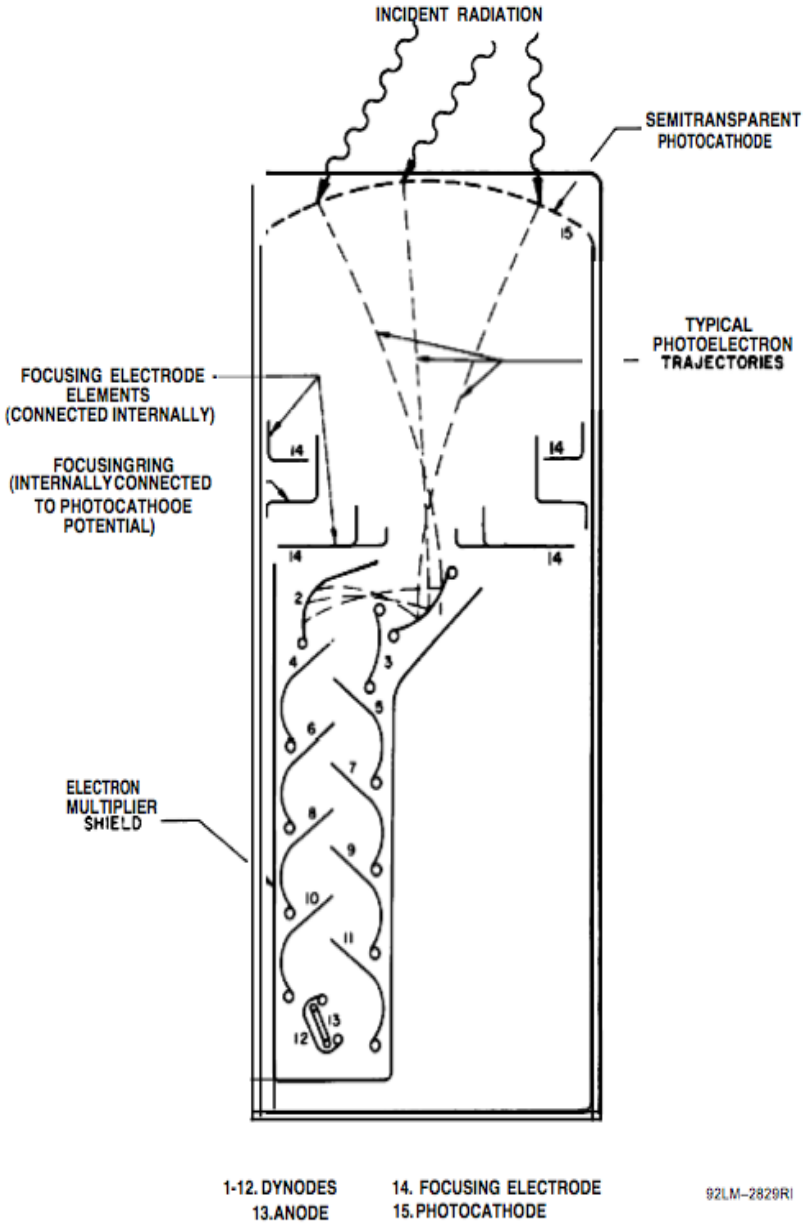

Figure E.1: Schematic arrangement of RCA8575 PMT structure with electron trajectories [Burle Handbook, 1980].

output usually used for energy measurements. For our applications, the anode signal was directly fanned out into the constant fraction discriminator to generator energy gates (fig. 3.5).

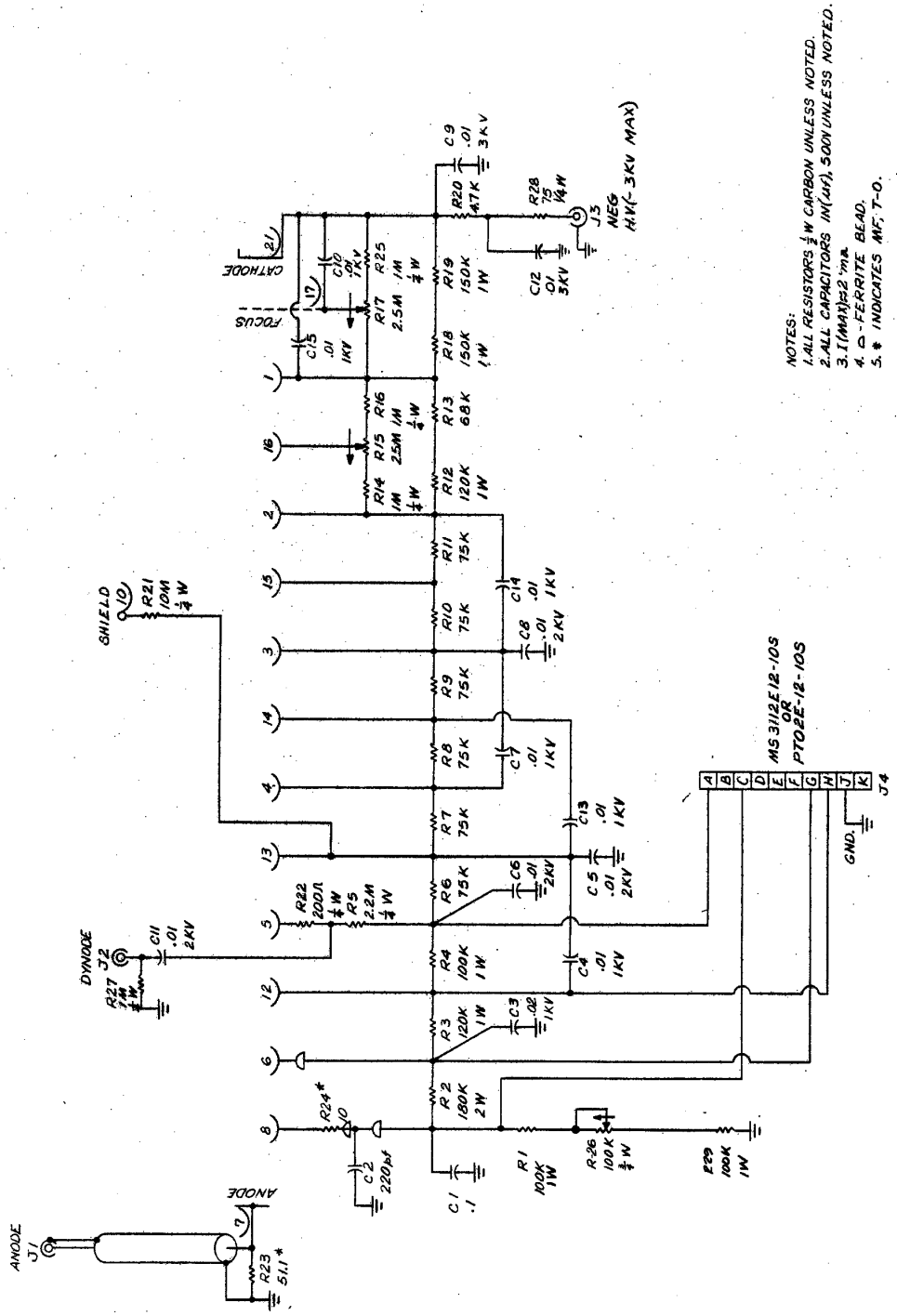

Figure E.2: Schematic of Ortec 265 PMT base.

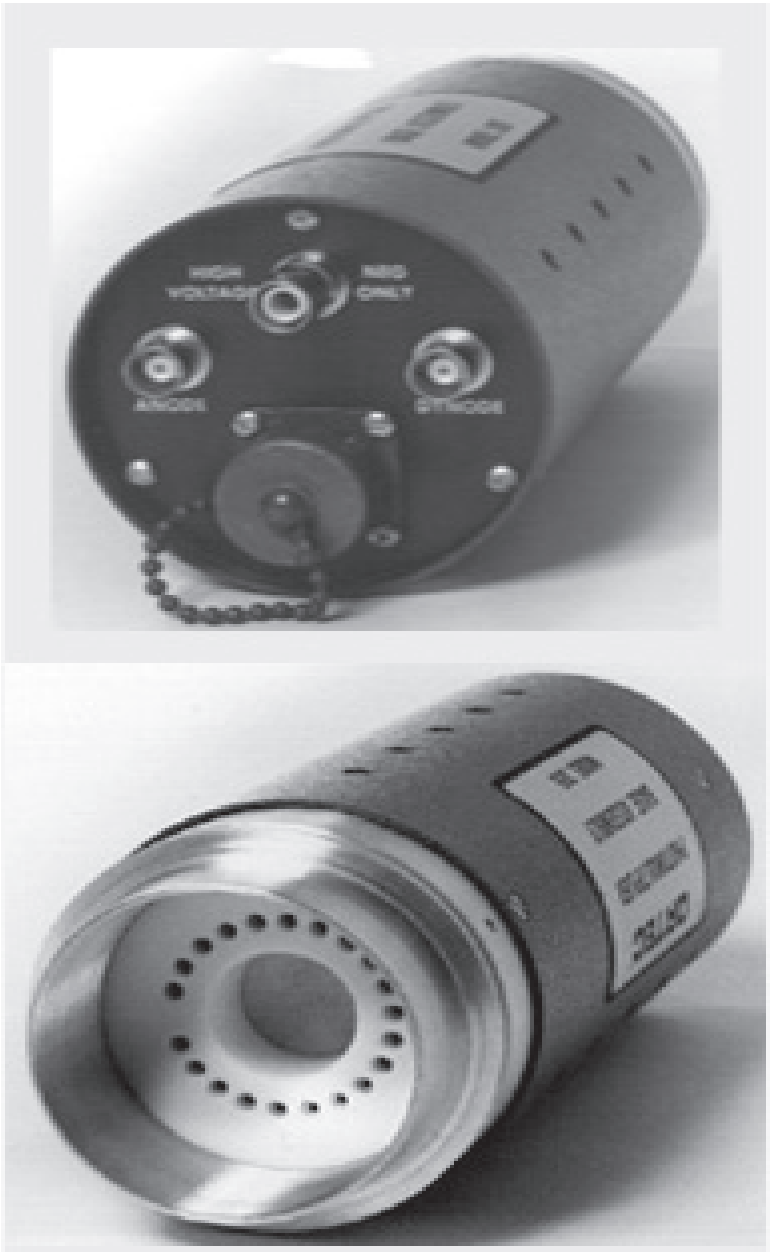

Figure E.3: Picture of Ortec 265 PMT base.

BIBLIOGRAPHY

BIBLIOGRAPHY

[Baur and Rebel, 1996] "Coulomb Breakup of Nuclei-Applications to Astrophysics," G. Baur and H. Rebel, Annu. Rev. Nucl. Part. Sci. 46 (1996) pp. 321-350.

[BBFH, 1957] "Synthesis of the Elements in Stars," Burbidge, E. M., Burbidge, G., Fowler, W. & Hoyle, F. Rev. Mod. Phys. 29 (1957) pp. 547-650.

[Becchetti, 2003] "The *TwinSol* Low-energy Radioactive Nuclear Beam Apparatus: Status and Recent Results" F. Becchetti, M. Lee, T. O'Donnell D. Roberts, J. Kolata. L. Lamm, G. Rogachev, V. Gimaraes, P. DeYoung and S. Vincent, Nucl. Instrum. Meth. A. (2003) pp. 377-380.

[Becchetti, 2001] "A Dual 6T Persistent-Mode SC Solenoid Ion-Optical System for Radioactive Nuclear Beam Research," F.D. Becchetti, M.-Y. Lee, D.A. Roberts, T.W. O'Donnell, J.A. Zimmerman, J.J. Kolata, D. Peterson, P. Santi, V. Guimarães, and L.O. Lamm, Proc. Conference on Applied Superconductivity, Virginia City, VA (September 2000); IEEE Transactions on Superconductivity 11 (1 Part 2), (March 2001) pp. 1601-1604.

[Becchetti, 1990] "Production and Use of Radioactive ^{7}Be Beams," F.D. Becchetti et al, Nucl. Instrum. Meth. A 294 (1990) pp. 26-30.

[Becchetti, 1989] "Measurements of Discrete Nuclear Reactions Induced by a Radioactive ^{8}Li Beam," F.D. Becchetti, W.Z. Liu, D.A. Roberts, J.W. Jänecke, J.J. Kolata, A. Morsad, X.J. Kong, and R.E. Warner, Phys. Rev. C 40, 3 (1989) pp. 1104-1107.

[Becchetti, 1976] "Response of Plastic Scintillator Detectors to Heavy Ions, $Z \leq 35$, $E \leq$ 170 MeV" F.D. Becchetti, C.E. Thorn, M.J. Levine, Nucl. Instrum. Meth. 138 (1976) pp. 93-104.

[Bell, Jr. and Haynes, 1957] *Liquid Scintillation Counting*, C. G. Bell, Jr. and F. N. Haynes, Pergamon Press, Oxford, UK., 1957.

[Birks, 1964] *The Theory and Practice of Scintillation Counting,* J. B. Birks Macmillan, New York, 1960.

[Bobbitt, 1973] "A study of 14N using the 13C(d,n)14N reaction," J.R. Bobbitt, M.P. Etten, G.H. Lenz, Nucl. Phys. A 203 (1973) pp. 353-368.

[Brenen and Olde, 1962] "The Response of Organic Scintillators to Electrons Deposited in Them," E. Brennen, E and G. Olde, G. Rad. Res. 16 (1962) pp. 1-6.

[Briesmeister, 1988] “MCNP-A General Monte Carlo Code N -Particle Transport Code” J.F. Briesmeister (Ed.), LA-12625-M, Los Alamos - Code N -Particle Transport Code, LA-12625-M, Los Alamos (unpublished).

[Brooks, 1979] “Development of Organic Scintillators,” F.D. Brooks, Nucl. Instrum. Meth.162 (1979) pp. 477-505.

[Brooks, 1980] “Proceedings of the International Conference on polarization phenomena in nuclear reactions, Santa Fe,” F. B. Brooks, P.M. Lister, J. M. Nelson, and K.S.Dhuga, 1980, unpublished.

[Burcham, 1963] *Nuclear Physics,* W. E. Burcham, McGraw-Hill Book Company, 1963.

[Burle Handbook, 1980] “Photomultiplier Handbook” Burle Industries, 1980.

[Caussyn, 1993] “Cross section for the primordial reaction ^{8}Li(p, n)^{8}Be(g.s) at E_{cm} = 1.5 MeV,” D. D. Caussyn, N. R. Fletcher, K. W. Kemper, E. E. Towers, J. J. Kolata, K. Lamkin, R. J. Smith, F. D. Becchetti, J.A. Brown, J. W. Janecke, D. A. Roberts, D. L. Gay, Phys. Rev. C. 47 (1993) pp. 387-391.

[Chadwick, 2006] "ENDF/B-VII.0: Next Generation Evaluated Nuclear Data Library for Nuclear Science and Technology,” M.B. Chadwick, P. Oblozinsky, M. Herman et. al. Nuclear Data Sheets, 107,(2006) pp. 2931-3060.

[Chadwick, 1932] “Possible Existence of a Neutron,” J. Chadwick, Nature 129 (1932) p. 312.

[Copi, Schramm, and Turner, 1995] “The Big-Bang Nucleosynthesis and the Baryon density in the Universe,” C. Copi, D. Schramm, M. Turner, Science (1995) pp. 1095-9203.

[Cookson, 1968] “The 13C(d,n)14N Reaction,” J. A. Cookson, Phys. Lett. 27 B, 10 (1968) pp. 619-621.

[Cranberg, 1956] “Neutrons from D – D Reactions” L. Cranberg, A. Armstrong, and R. Henkel, Phys. Rev. 104 (1956) pp. 1639 – 1642.

[Crookes, 1903] “Certain properties of the emanations of radium,” W. Crookes, Chem. News 87 (1903) p. 241.

[Eichholz and Poston, 1982] *Principles of Nuclear Radiation Detection*, G. Eichholz, and J. Poston, Ann Arbor Science Publishers, 1982.

[Eisberg and Resnick, 1985] *Quantum Physics,* R. Eisberg and R. Resnick, John Wiley and Sons, 1985.

[Eljen web page] Eljen Technologies: Website-www.eljentechnology.com

[Epstein, 1976] "The Origin of Deuterium," R. Epstein*, J. M. Lattimer, and D. N. Schramm. 263 Nature (1976) pp. 198 - 202

[Fuchs, 1966] "Shell Model Configurations of States in 14N Studied by the 13C(d,n)14N Reaction," H. Fuchs, K. Brabisch, P.Kraaz, and G. Roschert, Phys. Lett. 23 (1966) pp 363-366.

[Gilmore and Hemingway, 1995] *Practical Gamma-Ray Spectrometry*, G. Gilmore, J. Hemingway, John Wiley and Sons Ltd. 1995.

[Hansen and Johnson, 1987] "The neutron halo of extremely neutron-rich nuclei," P. G. Hansen and B. Johnson, Europhys. Lett. 4 (1987) pp. 409-414.

[Howard, 1974] "Differential cross section for np and nd elastic scattering near 130 MeV," J. Howard, J. A. Edgington and S. S. Das Gupta, Nucl. Phys. A 218 (1974) pp. 140-150.

[Klein and Brooks, 2006] "Scintillation detectors for fast neutrons," H. Klein, F. Brooks, Proceedings of Science, International Workshop on Fast Neutron Detectors, University of Cape Town, South Africa, 2006 (unpublished).

[Knoll, 2000] *Radiation Detection and Measurement*, G. Knoll, Wiley Publishers, 3rd Edition, 2000.

[Kobayashi, 1997] "Quasifree Nucleon-Knockout Reactions from Neutron-Rich Nuclei by a Proton Target: p(^{6}He, pn) ^{5}He, p(^{11}Li, pn) ^{10}Li, p(^{6}He, 2p) ^{5}H, and p(^{11}Li, 2p)^{10}He," T. Kobayashi, K. Yoshida, A. Ozawa, I. Tanihata, A. Korshenninnikov, E. Nikolski, T. Nakamura, Nucl. Phys. A. 616 (1997) pp. 223c-230c.

[Kolata, 2008] D+D cross section data and private communication. 2008.

[Kolata, 2006] "A Large Segmented Neutron Detector for Reaction Studies with Radioactive Beams near the Coulomb Barrier," J. J. Kolata, Hanan, Amro, M. Cloughesy, P. A. Deyoung, J. Rieth, J.P. Bychowski, G. Peaslee, Nucl. Instrum. Meth.A 557 (2006) pp. 594-598.

[Kolata, 1989] "A Radioactive Beam Facility using a Large Superconducting Solenoid," J.J. Kolata, F.D. Becchetti, W.Z. Liu, D.A. Roberts, and J.W. Jänecke, Nucl. Instrum. Meth. B40/41, (1989) pp. 503- 506.

[Krane, 1988] *Introductory Nuclear Physics,* K. Krane, John Wiley and Sons, 1988.

[Lee, 2002] "*Twinsol:* A Dual Superconducting Solenoid Ion-Optical System for the Production and Study of Low-Energy Radioactive Nuclear Beam Reactions," M.-Y. Lee Ph.D. Thesis, University of Michigan 2002 (unpublished).

[Lee, 1997] *" TwinSol*: A Dual Superconducting Solenoid System for Low-Energy Radioactive Nuclear Beam Research," M. Y. Lee, F. D. Becchetti, J. M. Holmes, T. W. O'Donnell, D. A. Roberts, J. A. Zimmerman, M. A. Rataczak, J. J. Kolata, L. O. Lamm, J. Von Schwarzenberg, M. Weischer, Proceedings of the 14th Int'l Conf. on the Applications of Accelerators in Research and Industry, Denton, Texas Nov. 1996, AIP Conf. Proc. 392, AIP Press, New York (1997) pp. 397-400.

[Lee, 1999] " Study of Nuclear Reactions with Intense, High-Purity, Low-energy Radioactive Ion Beams using a Versatile Multi-configuration Dual Superconducting-solenoid systems," M. Y. Lee, F. D. Becchetti, J. M. Holmes, T. W. O'Donnell, D. A. Roberts, J. A. Zimmerman, M. A. Rataczak, J. J. Kolata, D. Peterson, P. Santi, P.A. DeYoung, G. F. Peaslee, J.D. Hinnefeld, Nucl. Instrum. Meth. A 422 (1999) pp. 536-540.

[Leo, 1987] *Techniques for Nuclear and Particle Physics Experiments*, W.R. Leo, Springer, 2nd edition, 1987.

[Lister, 1981] "Experimental Reaction Studies with Polarised Ion Beams" P. Lister, Ph. D. Thesis 1981, University of Birmingham, U.K. (unpublished).

[Liu, 1990] "Production and Use of Radioactive Ion Beams for measurements of Nuclear Reactions" W. Liu, Ph.D Thesis, University of Michigan, 1990 (unpublished).

[Ludewigt, 2007] "High-yield D–T neutron generator," B.A. Ludewigt, R.P. Wells, J. Reijonen, Nucl. Instrum. Meth. B, 261 (2007) pp. 830-834.

[Marion and Fowler, 1960] *Fast Neutron Physics; Part 1: Techniques; Part 2: Experiments and Theory*, J.B. Marion, J.L. Fowler Eds., Interscience, New York, 1960

[Marone, 2002] "Pulse Shape Analysis of Liquid Scintillators for Neutron Studies", S. Marrone et al. Nucl Instrum. Meth. A 490 (2002) pp. 299-307.

[McBeth, 1971] "Pulse Shape Discrimination in Inorganic and Organic Scintillators" G. W. McBeth, R. A. Winyard and J.E. Lutkin. Nucl Instrum. Meth. 95 (1971) pp. 141-153.

[Milner, 1980] "Upak documentation," W.T. Milner, Oak Ridge National Laboratory (unpublished).

[Nucl. Structure Lab Webpage, 2009] http://isnap.nd.edu/

[Olive, 2000] " Primordial Nucleosynthesis: Theory and Observations," S. G. Ryan, T. C. Beers, K. A. Olive, J. E. Norris, and B. D. Fields, Ap. J. Lett. 530: L, (2000) pp. 57-60.

[Pozzi, 2004] "Analysis of Neutron and Photon Detection Position for the Calibration of Plastic (BC420) and Liquid (BC-501) Scintillators," S. A. Pozzi, J. A. Mullens, and J. T. Mihalczo, Nucl. Instrum. Meth. A, 524/1–3 (2004) pp. 92–101.

[Pozzi, 2003] "MCNP-PoliMi: A Monte Carlo Code for Correlation Measurements," S. A. Pozzi, E. Padovani, and M. Marseguerra, Nucl. Instrum. Meth. A, 513/3 (2003) pp. 550–558.

[Pozzi and Padovani, 2002] MCNP-PoliMi ver.1.0 user's manual, E. Padovani, S.A. Pozzi, CESNEF-021125, Library of Nuclear Engineering Department, Politecnico di Milano, November 2002 (unpublished).

[Pozzi, Chiang, and Oberer, 2000] "Method to Correlate CFD Discriminator Level and Energy Deposition by Neutrons and Photons in a Fast Plastic Scintillating Detector" L.G. Chiang, R.B. Oberer, and S.A. Pozzi, ORNL/TM-2000/193, Oak Ridge National Laboratory (2000) (unpublished).

[Roberts, 1992] "Deuterated Liquid Scintillator (NE230) as a Fast Neutron Detector for Cold-Fusion and other Research," D. A Roberts, F.D. Becchetti, K. Ashktorab, D. Steward, J. Janecke, H. R. Gustafson, M. J. Dueweke, IEEE Trans. Nucl. Sci. 39/4 (1992) pp. 532-535.

[Roberts, 1995] "Neutron decay from the isobaric analog state in Sb populated in ^{120}Sn(^{3}He, t) ^{120}Sb at E(^{3}He) = 200 MeV, $\theta = 0°$," D. A Roberts, F.D. Becchetti, K. Ashktorab, D. Steward, J. Janecke, M. N. Harakeh, S. Y. Van der, C. C. Foster, J. E. Lisantti, T. Rinckel, E. J. Stephenson, S. P. Wells, A. Nadasen, Phys. Rev. C 52 (1995) pp. 1361-1367.

[Rolfs and Rodney, 1988] *Cauldrons in the Cosmos,* C. Rolfs and W. Rodney, University of Chicago Press, 1988.

[Rolfs and Barnes, 1990] "Radiative Capture Reactions in Nuclear Astrophysics," C. Rolfs and C. Barnes, Annu. Rev. Nucl. Part. Sci. 40 (1990) pp. 45-77.

[Schram, 1963] *Organic Scintillation Detectors,* E. Schram, and R. Lombaert, Elsevier Pub. Company, Amsterdam, 1963.

[Schramm, 1996] *The Big Bang and Other Explosions in Nuclear and Particle Astrophysics,* D. Schramm, World Scientific Publishing, London, 1996.

[Smith, 1968] "Measurement of the Response of Several Organic Scintillators to Electrons, Protons, and Deuterons," D. L. Smith, R. G. Polk, and T. G. Miller, Nucl. Instrum. Meth. 64 (1968) pp. 157-166.

[Smith and Craun, 1970] "Analysis of Response Data for Several Organic Scintillators" Smith, D, Craun, R, Nucl. Instrum. Meth. 80 (1970) pp. 239-244.

[Sparrow Corp, 2006] “KMAX Users Manual,” Sparrow Corporation, 2006 www.sparrowcorp.com

[Spite, 1982] “Abundance of lithium in unevolved halo stars and old disk stars: interpretation and consequences,” F. Spite and M. Spite. Astron. Astrophys. 115 (1982) pp. 357-366.

[Swank, 1954] “Characteristics of Scintillators” R. K. Swank, Ann. Rev. Nucl. Sci. 4 (1954) pp. 111-140.

[Thornton, 1969] “The D(d,n)3He Reaction From Ed = 5 to 10 MeV” S. Thornton, Nucl Physics A 136 (1969) pp. 25-34.

[Tornow, 1985] “Measurement of the Response of the Deuterated Scintillators NE230 and NE232 to Protons and Neutrons,” W. Tornow, W. Arnold, J. Herdtweck, and G, mertens, Nucl. Instrum. Meth. A. 244 (1986) pp. 477-482.

[Turner, 2000] “The Dark Side of the Universe: from Zwicky to accelerated expansion,” M. S. Turner, Physics Report, 333-334 (2000) pp. 619 – 635.

[Zwicky, 1937] “On the Masses of Nebulae and of Clusters of Nebulae”F. Zwicky, ApJ, 86 (1937) pp. 217 – 246.